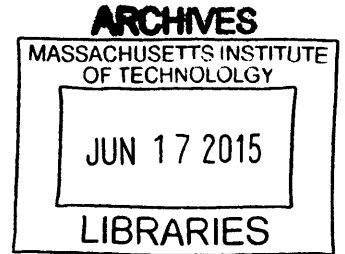


Understanding and Designing Carbon-based Thermoelectric Materials with Atomic-Scale Simulations

by
Jeong Yun Kim



B.S. Materials Science and Engineering, Seoul National University, Korea, 2009

Submitted to the Department of Materials Science and Engineering
in partial fulfillment of the requirements for the degree of

**DOCTOR OF PHILOSOPHY IN MATERIALS SCIENCE AND ENGINEERING
AT THE
MASSACHUSETTS INSTITUTE OF TECHNOLOGY**

June 2015

©2015 Massachusetts Institute of Technology. All rights reserved.

Signature redacted

Signature of Author: _____

Department of Materials Science and Engineering
May 8th, 2015

Signature redacted

Certified by: _____

y w /
Jeffrey C. Grossman
Professor of Materials Science and Engineering
Thesis Supervisor

Signature redacted

Accepted by: _____

[Handwritten signature]
Donald R. Sadoway
John F. Elliott Professor of Materials Science and Engineering
Chair, Departmental Committee on Graduate Students

Understanding and Designing Carbon-based Thermoelectric Materials with Atomic-Scale Simulations

by

Jeong Yun Kim

Submitted to the Department of Materials Science and Engineering
on May 8th, 2015 in partial fulfillment of the requirements for the degree of
Doctor of Philosophy in Materials Science and Engineering

Abstract

Thermoelectric (TE) materials, which can convert unused waste heat into useful electricity or *vice versa*, could play an important role in solving the current global energy challenge of providing sustainable and clean energy. Nevertheless, thermoelectrics have long been too inefficient to be utilized due to the relatively low energy conversion efficiency of present thermoelectrics. One way to obtain improved efficiency is to optimize the so-called TE figure of merit, $ZT = S^2\sigma/\kappa$, which is determined by the transport properties of the active layer material. To this end, higher-efficiency thermoelectrics will be enabled by a deep understanding of the key TE properties, such as thermal and charge transport and the impact of structural and chemical changes on these properties, in turn providing new design strategies for improved performance.

To discover new classes of thermoelectric materials, computational materials design is applied to the field of thermoelectrics. This thesis presents a theoretical investigation of the influence of chemical modifications on thermal and charge transport in carbon-based materials (*e.g.*, graphene and crystalline C₆₀), with the goal of providing insight into design rules for efficient carbon-based thermoelectric materials. We carried out a detailed atomistic study of thermal and charge transport in carbon-based materials using several theoretical and computational approaches – equilibrium molecular dynamics (EMD), lattice dynamics (LD), density functional theory (DFT), and the semi-classical Boltzmann theory.

We first investigated thermal transport in graphene with atomic-scale classical simulations, which has been shown that the use of two-dimensional (2D) periodic patterns on graphene substantially reduces the room-temperature thermal conductivity compared to that of the pristine monolayer. This reduction is shown to be due to a combination of boundary effects induced from the sharp interface between sp² and sp³ carbon as well as clamping effects induced from the

additional mass and steric packing of the functional groups. Using lattice dynamics calculations, we elucidate the correlation between this large reduction in thermal conductivity and the dynamical properties of the main heat carrying phonon modes.

We have also explored an understanding of the impact of chemical functionalization on charge transport in graphene. Using quantum mechanical calculations, we predict that suitable chemical functionalization of graphene can enhance the room-temperature power factor of a factor of two compared to pristine graphene. Based on the understanding on both transport studies we have gained here, we propose the possibility of highly efficient graphene-based thermoelectric materials, reaching a maximum $ZT \sim 3$ at room temperature. We showed here that it is possible to independently control charge transport and thermal transport of graphene, achieving reduced thermal conductivity and enhanced power factor *simultaneously*. In addition, we discuss here the broader potential and understanding of the key thermoelectric properties in 2D materials, which could provide new design strategies for high efficient TE materials.

Transport properties of crystalline C_{60} are investigated, and the results demonstrate that these properties can be broadly modified with metal atom intercalation in crystalline C_{60} . In contrast to the case of graphene, where chemical modifications induce structural changes in graphene lattice (from sp^2 C to sp^3 C), intercalating metal atoms only modify van der Waals interactions between C_{60} molecules, but still having a huge impact on both thermal and charge transport. Taken both transport studies together, we suggest that the metal atom intercalation in crystalline C_{60} could be a highly appealing approach to improve both transports in solid C_{60} , and with appropriate optimization of TE figure of merit, ZT value as large as 1 at room-temperature can be achieved.

This dissertation consists of five chapters. Chapter 1 contains a brief review of thermoelectric materials. Chapter 2 introduces the theoretical approaches for computing both thermal (with molecular dynamics and lattice dynamics) and charge transport (with density functional theory and semi-classical Boltzmann approach) in materials. In Chapter 3, our study of thermal transport in functionalized graphene is presented. Chapter 4 describes our results on charge carrier transport in functionalized graphene. Combining these two works, we predict the full ZT values of functionalized graphene. Chapter 5 describes how to optimize ZT value in metal atom intercalated crystalline C_{60} .

Thesis Supervisor: Jeffrey C. Grossman

Title: Professor of Materials Science and Engineering

Acknowledgment

I would hereby like to appreciate my mentors, colleagues, friends, and family over the course of my studies. This doctoral thesis is and will be a milestone in my life that would not have been completed without their support.

First of all, I would like to express my appreciation to my thesis advisor, Professor Jeffrey C. Grossman, who led me into this interesting research area of computational material design. Since I joined his group in 2009, I have learned a lot from him. In the respect of research, I learned the details of simulation methods, how to apply theoretical approaches to material design, and how to think creatively. In addition, for outside of research, I learned the ways to interact with others, how to become an independent researcher and a good leader, and attitude toward science and research. He always encouraged me to try new ideas, and helped me with his insightful thoughts. Also, he helped me to overcome difficulties in doing research and course work by encouraging me with thoughtful and kind words, trusting me and waiting me. It is the biggest luck of my life to meet Jeff as my advisor. Without his guidance and support over the past academic years, I could not have completed this thesis.

I am also grateful to my thesis committee members, Professor Harry Tuller and Professor Gang Chen, for sharing their invaluable time and knowledge. Their constructive inputs and ideas improve my research and thesis. I also appreciate Professor Joo-Hyoung Lee in GIST (Gwangju Institute of Science and Technology) in Korea, my research mentor in early academic years, for sharing his experiences and knowledge of computations in thermoelectric field.

Next, I am indebted to current and past Grossman group members for their friendship and helpful discussions. I specially thank my 13-4069 officemates; Donghun Kim, Jongwon Choi, Michelle Tomasik, Sophia Sklan, Dr. David Zhitomirsky, Sangjin Lee, Priyank Kumar, Dr. Can Ataca, Kayahan Saritas and Tiziana Musso. I have enjoyed our conversations and discussions. I would also like to thank Dr. Huashan Li, Dr. Li-Chiang Lin, Dr. Yun Liu, Dr. Francesca Fisplendi, Dr. David Strubbe, Dr. David Cohen-Tanugi, Dr. Rajamani Raghunathan, Dr. Giuseppe Romano, and Dr. Marco Bernardi, Prof. Alexie Kolpak, Prof. Alex Greaney and Prof.

Engin Durgun for their helpful discussions. Also, I thank Eugene Cho and Jee Soo Yoo and Brenden Smith for their support.

I must express my gratitude to all the members in KGMSE and KGSA at MIT, who enrich my life at MIT, especially for Dr. Shinyoung Kang, Dr. Eunseon Cho, Jiyoun Chang, Dr. Dahyun Oh and Dr. Jaechul Kim. I also thank my friend Hyerim Hwang from Harvard. I truly appreciate their warm hearts and supports.

Lastly, I owe my large debt of gratitude to my family members: my father, Youngbyoung Kim, my mother, Meejung Kim, my sister, Jeongin Kim, my two younger brothers, Hyunjae Kim and Seongdong Kim. I deeply appreciate that their endless and unconditional love and unlimited support. Without their encouragement, this work would never be accomplished. I also thank parents-in-law for their bottomless support and care. Most of all, I give my sincerest thanks to my husband, Rhokyun Kwak. He always loved me and raised me up when I was down, and also gives me lots of helpful advices and guidance as a research and life mentor. I would like to dedicate this thesis to my parents and husband, who have devoted themselves to me.

Table of contents

1.Introduction	12
1.1. Review of Thermoelectrics.....	12
1.2. Principles of Operation.....	14
1.2.1. Thermoelectric Power Generation.....	14
1.2.2. Thermoelectric Cooling.....	16
1.3 Materials Requirements	16
1.3.1. Efficient Thermoelectric Materials.....	16
1.3.2. Strategies for Improving Efficiency.....	18
1.4. Current Thermoelectric Material.....	21
1.5. Carbon-based Materials as a Promising Thermoelectric Material.....	21
1.6. Thesis Objectives.....	23
References.....	24
2. Theoretical Approaches	26
2.1. Introduction.....	26
2.2. Thermal Transport.....	26
2.2.1. Molecular Dynamics Simulations.....	27
2.2.2. Lattice Dynamics Simulations.....	28
2.3. Charge Carrier Transport.....	31
2.3.1. Density Functional Theory.....	31
2.3.2. Boltzmann Transport Theory.....	33
2.3.3. Semi-classical Theory – Transport Coefficients.....	34
2.3.4. Relaxation time.....	36
References.....	38
3. Thermal Transport in Functionalized Graphene	40
3.1. Introduction to Thermal Transport in Functionalized Graphene.....	40
3.2. Thermal Conductivity of Chemically Functionalized Graphene.....	42
3.2.1. Pristine Graphene.....	43
3.2.2. Chemically Functionalized Graphene.....	44

3.2.2.1. H-Functionalized Graphene.....	45
3.2.2.2. C5-Functionalized Graphene.....	47
3.2.2.3. (C5+H)-Functionalized Graphene.....	52
3.3. Understanding Reduction Mechanisms in Functionalized Graphene.....	53
3.2.1. Pristine Graphene.....	53
3.2.2. H-Functionalized Graphene.....	53
3.2.3. C5-Functionalized Graphene.....	55
3.4. Outlook and Future Work.....	56
References.....	57
4. High-Efficiency Thermoelectrics with Functionalized Graphene	59
4.1. Introduction to High-Efficiency Thermoelectrics with Functionalized Graphene.....	59
4.2. Atomic Structure of Chemically Functionalized Graphene.....	60
4.3. Charge Carrier Transport in H-Functionalized Graphene.....	61
4.3.1. Electronic Structure.....	61
4.3.2. Relaxation Time.....	64
4.3.3. Transport Coefficients	65
4.4. Charge Carrier Transport in C5-Functionalized Graphene.....	68
4.4.1. Electronic Structure.....	68
4.4.2. Relaxation Time.....	69
4.4.3. Transport Coefficients	70
4.5. Charge Carrier Transport in (C5+H)-Functionalized Graphene.....	71
4.6. Charge Carrier Transport in Pristine Graphene	72
4.7. Prediction of overall ZT values.....	73
4.7.1. Klemens Model.....	74
4.7.2. ZT values in Functionalized Graphene.....	75
4.8. Outlook and Future Work.....	78
References.....	79
5. Optimization of the Thermoelectric Figure of Merit in Crystalline C₆₀ with Intercalation Chemistry	81

5.1. Introduction to Crystalline C_{60}	81
5.2. Effect of Doping Composition on Thermoelectric Properties in A_xC_{60}	82
5.2.1. Crystal Structure and Electronic Structure in A_xC_{60}	82
5.2.2. Thermal Transport in A_xC_{60}	84
5.2.3. Charge Transport in A_xC_{60}	86
5.2.4. Prediction of Figure of Merit ZT in A_xC_{60}	89
5.3. Effects of Dopants on Thermoelectric Properties in A_xC_{60}	90
5.3.1. Face-centered Cubic (fcc) A_3C_{60}	90
5.3.2. Base-centered Cubic (bcc) A_6C_{60}	93
5.4. Outlook and Future Work.....	98
References.....	98
6. Conclusion.....	100

List of Figures

Figure 1.1: Thermoelectric device efficiency

Figure 1.2: Thermoelectric device

Figure 1.3: Normalized thermoelectric properties and ZT versus doping concentration at 300 K for n-type $\text{Si}_{80}\text{Ge}_{20}$

Figure 1.4: Crystal structure of CoSb_3 , which contains large void spaces shown in blue

Figure 1.5: Electronic density of states for a bulk 3D crystalline semiconductor, a 2D quantum well, a 1D nanowire or nanotube, and a 0D quantum dot

Figure 1.6: Figure of merit of current state of the art thermoelectric materials *versus* temperature

Figure 1.7: Diverse structures in carbon-based materials

Figure 3.1: Thermal conductivities of square graphene sheets as a function of graphene sheet size

Figure 3.2: Chemically functionalized graphene with H atoms and hydrocarbon chains

Figure 3.3: Thermal conductivities of HG samples both perpendicular (red) and parallel (blue) to the pattern as a function of H pattern coverage

Figure 3.4: Thermal conductivities of C5G samples as a function of C5 pattern coverage

Figure 3.5: Thermal conductivities of fully functionalized graphene as a function of functional groups (hydrogen atom, “fake” hydrogen atom and C5 chains)

Figure 3.6: Schematic of phonon confinement effects in graphene with the two different functionalizations considered in this work: hydrogen (upper) and C5 chain (lower)

Figure 3.7: Thermal conductivities of patterned graphene as a function of functional groups are shown for (a) 0.5 and (b) 0.75 pattern coverage

Figure 3.8: Main heat carrying phonon modes, whose κ contribution is larger than 4% of total κ , for pristine graphene and HG and C5G samples with 50% coverage

Figure 4.1: 2D thermoelectric based on patterned graphene nano-roads with two different chemical functionalizations

Figure 4.2: Thermoelectric properties of H-functionalized patterned graphene nano-roads

Figure 4.3: Calculated relaxation time of three different HG samples at n_{peak} and as a function of N_C for $N_C = 3p+2$ (pink), $N_C = 3p$ (green) and $N_C = 3p+1$ (blue), respectively

Figure 4.4: Thermoelectric properties of H-functionalized Graphene in 3p family

Figure 4.5: Thermoelectric properties of C5-functionalized graphene

Figure 4.6: Calculated Seebeck coefficients (a) and electrical conductivities (b) of fully functionalized C5G as a function of carrier concentration

Figure 4.7: Thermoelectric properties of pristine graphene as a function of carrier concentration (n_i). (a) Seebeck coefficient. (b) electrical conductivity, and (c) power factor

Figure 4.8: Thermal conductivities of functionalized graphene with H pattern (solid line), C5 pattern (dashed line) and C5+H pattern (dotted line) parallel to the pattern as a function of pattern width

Figure 4.9: Calculated thermal conductivities of patterned graphene as a function of functional groups are shown for $N_C = 8$ pattern width at 300 K, where $\kappa_{Total} = \kappa_{MD} + \kappa_{Correct}$.

Figure 4.10: Thermoelectric properties of patterned graphene nano-roads with different functional groups

Figure 5.1: Hückel energy levels of C_{60} molecule, band structure of crystalline fcc C_{60} , and resistivity of K_3C_{60} as a function of temperature, exhibiting superconducting behavior upon the introduction of K atom

Figure 5.2: Unit cells and corresponding band structures of K_3C_{60} in the fcc lattice and K_6C_{60} in the bcc lattice

Figure 5.3: Calculated electronic (green), lattice (sky-blue) and total (dark-blue) thermal conductivities of K_xC_{60} samples as a function of doping composition

Figure 5.4: Calculated power factors of pristine fcc C_{60} , K_3C_{60} in fcc lattice and K_6C_{60} in bcc lattice

Figure 5.5: Calculated figure of merit ZT values of pristine fcc C_{60} , K_3C_{60} in the fcc lattice and K_6C_{60} in the bcc lattice

Figure 5.6: Computed density of states of A_3C_{60} ($A = Na, K, Rb$ and Cs) fullerenes

Figure 5.7: Electronic thermal conductivity (green), power factor (purple) and ZT (orange) values of A_3C_{60} ($A = Na, K, Rb$ and Cs) fullerenes in fcc lattice

Figure 5.8: The effect of the metal atom intercalation on bandwidth

Figure 5.9: Thermoelectric properties of $A_xAE_{6-x}C_{60}$ ($x = 0, 3$ and 6) fullerenes

Chapter 1

Introduction

1.1. Review of Thermoelectrics

Thermoelectric (TE) materials, which can convert waste heat into useful electricity or vice versa, could play an important role in solving the current global energy challenge to develop alternative energy technologies that reduce our dependence on fossil fuels and to provide sustainable and clean energy. They are appealing for current energy conversion devices such as air conditioners, refrigerators, heat pumps, heat exchangers, and turbine engines. This is due to the fact that the TE power generator and Peltier cooler have no moving parts, making them simpler and cleaner, whereas conventional devices employ a working fluid such as the steam in heat engines or chlorofluorocarbons (Freon). Owing to that, they are silent, scalable and reliable, making them applicable for small size devices such as power generators in satellites and spaceships or car seat cooler/heaters.

Although thermoelectric devices are becoming more prominent with the effort to utilize waste heat recovery techniques, solid-state thermoelectric power generation is not widely utilized owing to its relatively low energy conversion efficiency compared to conventional devices. The efficiency of TE materials in power generation is characterized as

$$\varepsilon = \frac{T_H - T_C}{T_H} \frac{\sqrt{1 + ZT} - 1}{\sqrt{1 + ZT} + T_C/T_H} \quad (1.1)$$

where T_H is the temperature of the hot side and T_C is the temperature of the cold side. ZT is the materials' dimensionless figure of merit: $ZT = S^2\sigma T/\kappa$, where S is the Seebeck coefficient, σ the electrical conductivity, κ the thermal conductivity, and T the temperature, respectively. Consequently, a significant ΔT and high ZT value are required to generate sufficient electrical energy. Current thermoelectric research has concentrated on the optimization of three conflicting transport coefficient (S , σ and κ). In order to maximize the ZT value of a material, a high S , high σ , and low κ are required. The difficulty in optimizing three interdependent transport properties has limited the room temperature ZT of bulk materials, such as Bi_2Te_3 , PbTe , and SiGe alloy, to a value of around 1 for the past five decades.

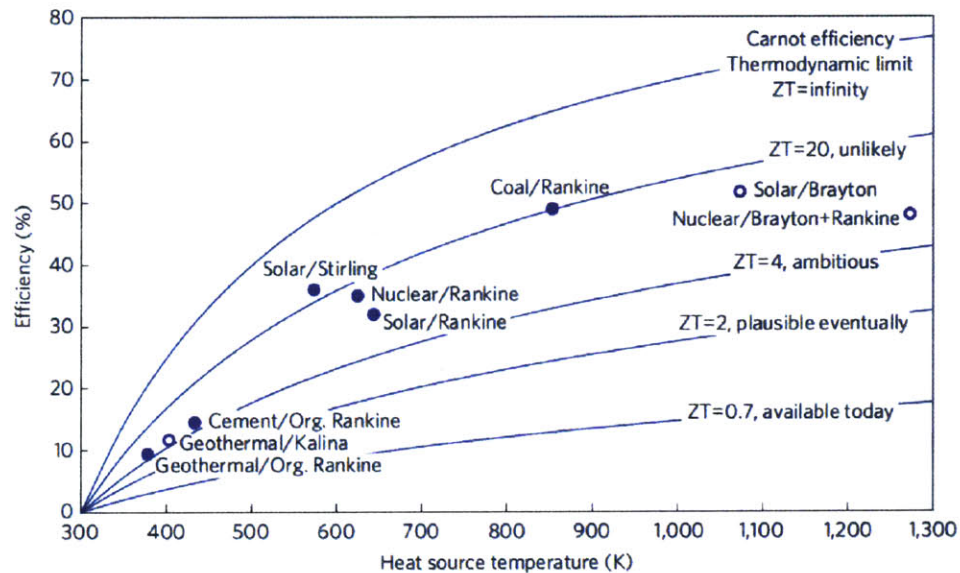


Figure 1.1 | Thermoelectric device efficiency. Efficiency of ‘best practice’ mechanical heat engines and thermoelectric energy conversion efficiency as a function of ZT at the setting of $T_C = 300\text{K}$. Figure taken from Vining C. B. *et al.*, *Nat. Mater.* **8**, 83-85 (2009).¹

Figure 1.1 shows the estimated thermoelectric device efficiency as a function of temperature of heat source and ZT value. Using materials with a ZT of 1, the efficiency of TE generator is limited to around 1/6 of the maximum possible Carnot efficiency. To compete with traditional mechanical energy conversion system, an efficiency of around 20-30% is needed, requiring ZT values of 2-3. For example, a TE device with $ZT = 3$ operating between 303 and 773 K yields approximately 50% of the Carnot efficiency.² In order to realize the potential economic and environmental benefits of thermoelectrics, the development of new high-efficiency TE materials is needed.

There have been many efforts to enhance ZT , for example by introducing impurity states in bulk materials,^{3,4} reducing the dimensionality,⁵⁻⁸ or using complex bulk materials.⁹⁻¹¹ Among the various routes to improve upon current TE efficiencies, the more recent use of nano-structured materials, such as superlattices, quantum wires and quantum dots,^{6,12-14} offers a new strategy to improve thermoelectric performance by allowing for independent control over the manipulation of electronic and thermal transport. Here, we focus on nano-structured TE materials, understanding the enhanced TE properties of nanostructured materials and showing their current limitations. Finally, based on this understanding, we propose a new direction to design nanostructured TE materials with high ZT values.

1.2. Principles of Operation

1.2.1. Thermoelectric Power Generation

Thermoelectric power generation devices are based on the Seebeck effect, which is the conversion of temperature differences to electric voltage. When a temperature gradient is applied across a TE material, mobile charge carriers (electrons or holes) diffuse from the hot

side of material to the cold side because charge carriers at the hot side have more thermal energy than carriers at the cold side. The building up of charge carriers at the cold side produces an electric field, which in turn opposes the diffusion. Equilibrium is reached when the material is in an open circuit, and the result is that an electrochemical potential is generated in response to the temperature gradient. This potential is known as the Seebeck voltage, and the amount of voltage generated per unit temperature gradient is called the Seebeck coefficient. This basic principle of TE power generation is shown in Figure 1.2b.

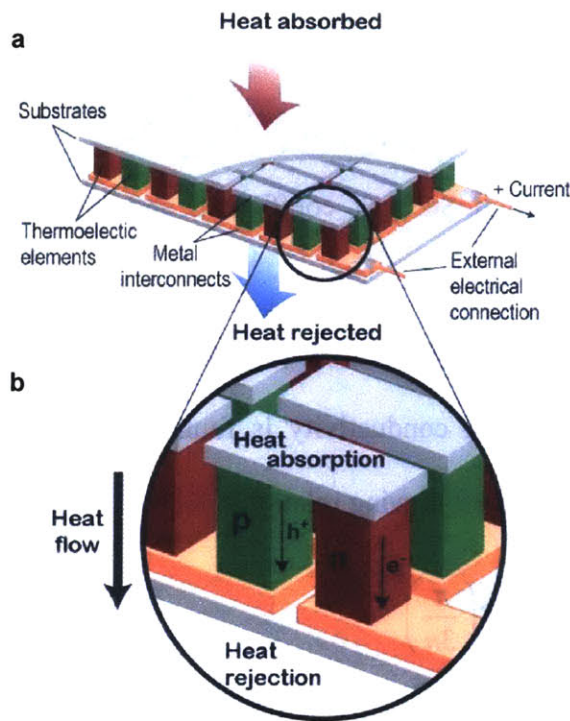


Figure 1.2 | Thermoelectric device. (a) TE module (b) shows the direction of charge flow. Figure taken from Snyder G. J. *et al.*, *Nat. Mater.* 105-114 (2008).⁹

Figure 1.2a shows a typical thermoelectric device, which contains many thermoelectric modules (shown in Figure 1.2b), consisting of n-type and p-type thermoelectric materials. These two elements are wired electrically in series and thermally in parallel. For power generation applications, a temperature gradient is applied across the length of the modules, and

modules are connected to a circuit.

1.2.2. Thermoelectric Cooling

Thermoelectric materials can also be used as solid-state refrigerators by taking advantage of the Peltier effect, which creates a heat flux between two dissimilar materials by driving a current in a circuit. When current is applied through the device, heat flows from one side to the other, cooling the one side, while heating the other side.

1.3. Materials Requirements

1.3.1. Efficient Thermoelectric Materials

Materials with high electrical conductivity, high Seebeck coefficient, and low thermal conductivity are required for high efficiency TE devices.

Power Factor ($S^2\sigma$): A large Seebeck coefficient is obtained in low carrier concentration semiconductors or insulators, while a high electrical conductivity is found in high carrier concentration metals, as can be seen by examining the following relations:

$$S = \frac{8\pi^2 k_B^2}{3eh^2} m^* T \left(\frac{\pi}{3n} \right)^{2/3} \quad (1.2)$$

$$\sigma = ne\mu \quad (1.3)$$

where k_B is the Boltzmann constant, e is the carrier charge, h is Plank's constant, m^* is the effective mass of the charge carrier, n is the carrier concentration, and μ is the carrier mobility. By combining these two expressions, one finds that the power factor value can have a maximum typically somewhere between the carrier concentrations of semiconductors and those of metals. Typically, heavily doped semiconductors with carrier concentrations of 10^{19} -

$10^{21} /\text{cm}^3$ are considered to be good candidate TE materials. For the Seebeck coefficient, a single type of charge carrier is required because mixed carrier types (n-type/p-type) would provide the opposite Seebeck effect, leading to a low overall Seebeck coefficient. As such, appropriate doping and band gaps that separate n-type and p-type are important, and high power factor TE materials are often heavily doped semiconductors with energy gaps less than around 1eV.

Thermal Conductivity (κ): For high ZT values, a low thermal conductivity is needed. The thermal conductivity of a material consists of two contributions: κ_l and κ_e , resulting from phonons and heat carrying charge carriers, respectively. According to Wiedemann-Franz law ($\kappa_e = L\sigma T$, where L is the Lorenz number), κ_e is proportional to σ , and thus reducing the electronic thermal conductivity would also reduce the electrical conductivity and is not a good way to enhance ZT. In contrast, the lattice thermal conductivity is not influenced (directly) by the electronic structure, so that reducing κ_l is an appealing route to achieve high improvements in ZT.

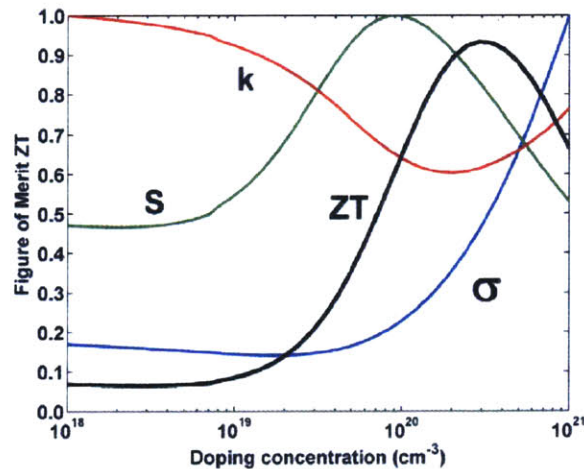


Figure 1.3 | Normalized thermoelectric properties and ZT versus doping concentration at 300 K for n-type Si₈₀Ge₂₀. Curves are calculated from a numerical model. In the figure, κ refers to thermal conductivity, S refers to the Seebeck coefficient, and σ refers to the electrical conductivity. Figure taken from Minnich, A. J. *et al.*, *Energy & Environmental Science* **2**, 466-479 (2009).¹⁵

Examples of good thermoelectric materials are Bi_2Te_3 , PbTe , and SiGe alloys at room, moderate, and high temperatures, respectively. However, further improvements are challenging because optimizing all thermoelectric parameters (S , σ , and κ) together is difficult because these transport properties are interdependent (see Figure 1.3 for the case of SiGe). For example, in order to obtain high electrical conductivity, we would like to increase the carrier concentration; however this in turn would decrease Seebeck coefficient as well as increase the electronic thermal conductivity. As a consequence, increasing carrier concentration does not lead to a net enhancement in ZT . These conflicting trends are the reason why the maximum in ZT for bulk thermoelectric materials has remained for the past five decades – until very recently – around 1.

1.3.2. Strategies for Improving Efficiency

There have been many efforts to enhance the TE efficiency. Here, we introduce two main strategies that exhibit tremendous advances in current thermoelectric materials.

Phonon Glass Electron Crystal (PGEC) Approach: In 1994, G.A. Slack proposed a “phonon glass electron crystal” approach,¹⁶ which suggests that an ideal thermoelectric material should be the combination of glass-like low thermal conductivity and crystal-like electronic transport. This approach leads to the idea of complex bulk thermoelectric materials such as skutterudites¹⁷ and clathrates.¹¹ Generally, these materials have a large amount of voids (vacancies) filled with heavy element atoms (often referred to as “rattler” atoms). The rattler atoms vibrate at low frequencies and act as effective phonon scattering centers, leading to a significant reduction in thermal conductivity. These PGEC materials maintain their crystalline properties for the electrons, resulting in high electrical conductivities. Figure 1.4 shows an

example of a skutterudite compound, CoSb_3 . Through this approach, $ZT > 1$ is obtained with filled skutterudites. For example, $\text{Ba}_{0.08}\text{La}_{0.05}\text{Yb}_{0.04}\text{Co}_4\text{Sb}_{12}$ has achieved a ZT of 1.7 at 850K.¹⁸

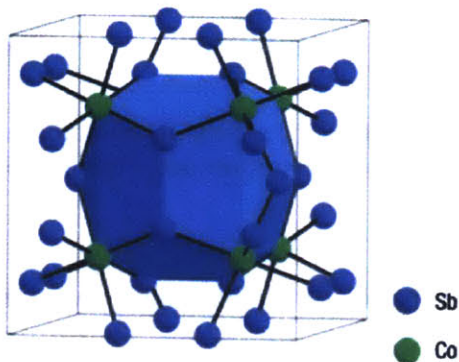


Figure 1.4 | Crystal structure of CoSb_3 , which contains large void spaces shown in blue. Figure taken from Snyder G. J. *et al.*, *Nat. Mater.* 7, 105-114 (2008).

Nanostructuring of Thermoelectric Materials: The idea of taking advantage of nanostructuring to enhance ZT was first introduced by Hicks and Dresselhaus in 1993.¹⁹ The introduction of nanostructures in TE materials, such as superlattices, quantum wires and quantum dots,^{6,20,21} can improve thermoelectric performance by manipulating the electronic and thermal transport separately. The thermal conductivity can be significantly reduced through nanostructuring of materials, which increases phonon scattering, without degrading the electron transport. Because the electron mean free path (MFP) is much shorter than that of phonons in typical semiconductors, in nanostructured materials the phonons with large MFP can be effectively scattered by a high density of interfaces, while preserving carrier mobility and electronic conduction.

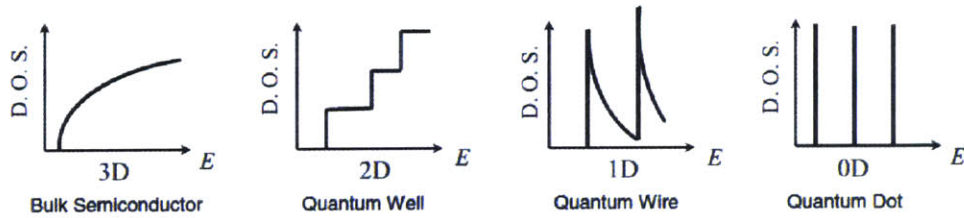


Figure 1.5 | Electronic density of states for a bulk 3D crystalline semiconductor, a 2D quantum well, a 1D nanowire or nanotube, and a 0D quantum dot. Figure taken from Dresselhaus, M. S. *et al.*, *Adv. Mater.* **19**, 1043-1053 (2007).⁷

In addition, reducing a material's dimensionality can introduce a sharp peak in the density of states (DOS) near the Fermi level due to quantum confinement (Figure 1.5), which may improve the thermoelectric efficiency by enhancing the Seebeck coefficient according to theoretical considerations by Mahan and Sofo,²² who predicted that a sharp increase in the DOS would improve Seebeck coefficient. In nanostructured materials, the Seebeck coefficient and electrical conductivity can be decoupled and tuned independently. Thus, high ZT values (around 2) have been reported in nanostructured TE materials (Figure 1.6).

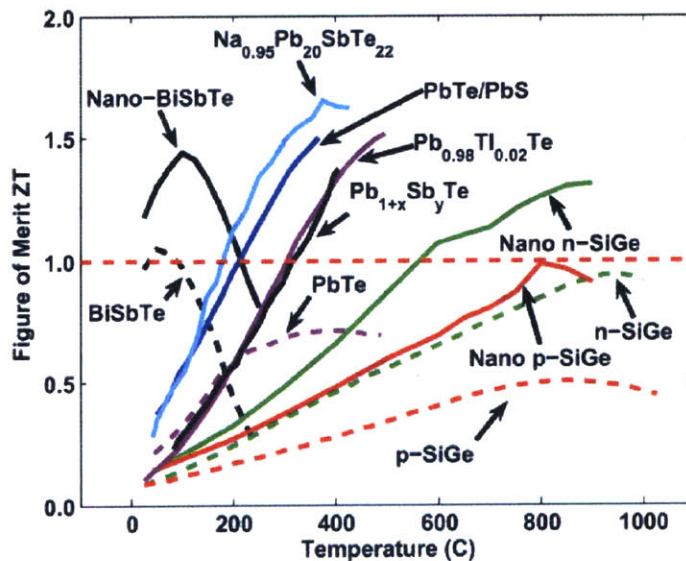


Figure 1.6 | Figure of merit of current state of the art thermoelectric materials versus temperature. The dashed lines show the maximum ZT values for bulk state of the art materials, and solid lines show recently reported ZT values of bulk nanostructured materials. Figure taken from Minnich, A. J. *et al.*, *Energy & Environmental Science* **2**, 466-479 (2009)¹⁵

1.4. Current Thermoelectric Materials

Many different ZT enhancing strategies have shown the improvements in thermoelectric fields for the last 20 years. Most of current state-of-the-art TE materials are achieved through nanostructuring, and the highest ZT value yet reported is around 2 at 915 K with hierarchical PbTe.²³ These TE materials are composed of heavy elements such as Pb, Bi, Te, Ge, Co, and Sb. Although TE materials with these elements exhibit high ZT values, these elements are expensive, scarce, and toxic. To satisfy industrial requirements, large-scale low cost, environmentally benign, non-toxic, and earth-abundant high performance TE materials are needed. Thus, we need to develop and discover new classes of TE materials with non-toxic, and earth-abundant elements such as C and Si. However, the ZT values of materials with these elements are so far less than other state-of-art TE materials. We can apply the same ZT enhancing strategies to these earth abundant materials to obtain high ZT values.

1.5. Carbon-based Materials as a Promising Thermoelectric Material

The need for new high-efficiency thermoelectrics has motivated researchers to discover and develop a range of new classes of thermoelectric materials. As we mentioned above, materials that are non-toxic, earth abundant, and exhibiting broad tunability of transport properties, are needed to exhibit improvements in the thermoelectric field.

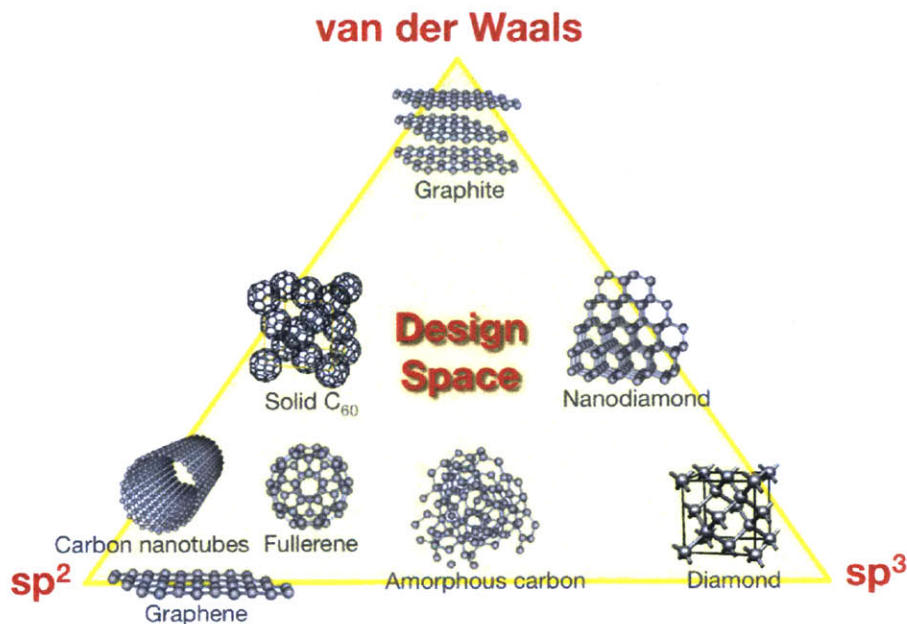


Figure 1.7 | Diverse structures in carbon-based materials. Three vertices of a triangle represent three possible bonding between C atoms in carbon-based materials.

In this respect, we suggest the potential of carbon-based nano-materials as a candidate for thermoelectric applications due to the wide range of possible bonding between C atoms in carbon-based materials (*e.g.*, sp^2 hybridization, sp^3 hybridization, and van der Waals interactions), which could provide diverse structures ranging from sp^3 -hybridized diamond to sp^2 -hybridized graphene. This diversity in structures generates a wide range of properties, particularly in transport. Among carbon-based materials, graphene, composed entirely of sp^2 -bonded C, exhibits superior thermal and charge transport, whereas crystalline C₆₀, where both sp^2 hybridization and van der Waals interactions coexist, generates extremely low thermal and charge transport. Furthermore, given that C-C interactions determine transport in these materials, any chemical modifications to the C-C bonds will be expected to have a large impact on the resulting transport properties. For example, the highly delocalized electronic structure of sp^2 -hybridized graphene can be widely modified with chemical functionalization,^{24,25} introducing sp^3 -C within graphene lattice, and accordingly leading to large modifications of charge carriers

and phonon modes. In addition, van der Waals interactions play an important role in determining transport in carbon-based materials. In crystalline C_{60} , the modified van der Waals interactions give rise to a change in electronic structure, resulting in tunable charge transport.^{26,27} Here, van der Waals interactions are modified by intercalating metal atoms into crystalline C_{60} . Thus, further broadened transport properties are possible in carbon-based materials with chemical modifications, an appealing attribute when faced with such constrained optimization problems as in the case of thermoelectrics. In addition to these aspects of nanostructured carbon as a basis for thermoelectric materials, carbon-based materials offer a range of advantages including earth abundance, low cost, high thermal-stability, solution processability, potential for flexible substrates, and chemical tunability. To this end, carbon-based materials are excellent candidates for thermoelectric materials.

1.6. Thesis Objectives

In this dissertation, we consider the prospect of carbon-based nano-materials as efficient thermoelectrics. Among possible carbon-based materials, we investigated the transport properties in both graphene (Chapter 3 and 4) and crystalline C_{60} (Chapter 5). These two carbon-based materials lie at the two extremes of the transport spectrum in carbon-based materials, where graphene exhibits superior transport in both fields, while crystalline C_{60} shows poor thermal and charge transport. Indeed, both of these materials are not good thermoelectric materials by themselves (without any modifications). However, as has been shown possible for other materials such as silicon,^{8,21} we believe it is possible to tailor these two extremes of carbon-based materials such that they exhibit a high thermoelectric figure of merit.

The first goal of this thesis is to understand thermal and charge transport in these carbon-

based nano-materials, and to investigate the influence of chemical modifications (*i.e.*, chemical functionalization for graphene, and intercalation of metal atoms for crystalline C₆₀) on the transport properties. This understanding is gained via both classical and quantum mechanical calculations, where the former is employed to calculate thermal transport properties, and the latter is employed for charge carrier transport studies. Combining both thermal and charge transport studies, we are able to predict ZT values for carbon-based materials. Next, based on these results, we optimize the thermoelectric figure of merit, identifying appropriate chemical functionalization and doping for graphene and crystalline C₆₀, respectively.

References

1. Vining, C. B. An inconvenient truth about thermoelectrics. *Nat Mater* **8**, 83-85 (2009).
2. Tritt, T. M., Boettner, H., Chen, L. Thermoelectrics: Direct solar thermal energy conversion. *Mrs Bulletin* **33**, 366-368 (2008).
3. Lee, J. H., Wu, J. Q., Grossman, J. C. Enhancing the Thermoelectric Power Factor with Highly Mismatched Isoelectronic Doping. *Phys Rev Lett* **104**, 016602 (2010).
4. Heremans, J. P., Jovovic, V., Toberer, E. S., Saramat, A., Kurosaki, K., Charoenphakdee, A., *et al.* Enhancement of thermoelectric efficiency in PbTe by distortion of the electronic density of states. *Science* **321**, 554-557 (2008).
5. Venkatasubramanian, R., Siivola, E., Colpitts, T., O'Quinn, B. Thin-film thermoelectric devices with high room-temperature figures of merit. *Nature* **413**, 597-602 (2001).
6. Harman, T. C., Taylor, P. J., Walsh, M. P., LaForge, B. E. Quantum dot superlattice thermoelectric materials and devices. *Science* **297**, 2229-2232 (2002).
7. Dresselhaus, M. S., Chen, G., Tang, M. Y., Yang, R. G., Lee, H., Wang, D. Z., *et al.* New directions for low-dimensional thermoelectric materials. *Adv Mater* **19**, 1043-1053 (2007).
8. Lee, J. H., Galli, G. A., Grossman, J. C. Nanoporous Si as an Efficient Thermoelectric Material. *Nano Lett* **8**, 3750-3754 (2008).
9. Snyder, G. J., Toberer, E. S. Complex thermoelectric materials. *Nat Mater* **7**, 105-114 (2008).
10. Uher, C. *Skutterudites: Prospective novel thermoelectrics*, Academic Press edn, vol. 69. Semiconductors and Semimetals: San Diego, 2001.
11. Nolas, G. S., Poon, J., Kanatzidis, M. Recent developments in bulk thermoelectric materials. *Mrs Bulletin* **31**, 199-205 (2006).
12. Li, D. Y., Wu, Y. Y., Kim, P., Shi, L., Yang, P. D., Majumdar, A. Thermal conductivity of individual silicon nanowires. *Appl Phys Lett* **83**, 2934-2936 (2003).
13. Donadio, D., Galli, G. Atomistic Simulations of Heat Transport in Silicon Nanowires. *Phys Rev Lett* **102**, (2009).
14. Lee, S. M., Cahill, D. G., Venkatasubramanian, R. Thermal conductivity of Si-Ge superlattices. *Appl Phys Lett* **70**, 2957-2959 (1997).
15. Minnich, A. J., Dresselhaus, M. S., Ren, Z. F., Chen, G. Bulk nanostructured thermoelectric materials: current research and future prospects. *Energy & Environmental Science* **2**, 466-479 (2009).
16. Slack GA., CRC Handbook of Thermoelectrics, ed. DM Rowe, Boca Raton, FL: CRC Press (1995)
17. Uher, C. Skutterudites: Prospective novel thermoelectrics. *Semicond Semimetals* **69**, 139-253 (2001).
18. Shi, X., Yang, J., Salvador, J. R., Chi, M. F., Cho, J. Y., Wang, H., *et al.* Multiple-Filled Skutterudites: High

- Thermoelectric Figure of Merit through Separately Optimizing Electrical and Thermal Transports. *J Am Chem Soc* **133**, 7837-7846 (2011).
19. Hicks, L. D., Dresselhaus, M. S. Thermoelectric Figure of Merit of a One-Dimensional Conductor. *Phys Rev B* **47**, 16631-16634 (1993).
 20. Hochbaum, A. I., Chen, R. K., Delgado, R. D., Liang, W. J., Garnett, E. C., Najarian, M., *et al.* Enhanced thermoelectric performance of rough silicon nanowires. *Nature* **451**, 163-U165 (2008).
 21. Boukai, A. I., Bunimovich, Y., Tahir-Kheli, J., Yu, J. K., Goddard, W. A., Heath, J. R. Silicon nanowires as efficient thermoelectric materials. *Nature* **451**, 168-171 (2008).
 22. Mahan, G. D., Sofo, J. O. The best thermoelectric. *Proc Natl Acad Sci USA* **93**, 7436-7439 (1996).
 23. Biswas, K., He, J. Q., Blum, I. D., Chun-Iwu, Hogan, T. P., Seidman, D. N., *et al.* High-performance bulk thermoelectrics with all-scale hierarchical architectures (vol 489, pg 414, 2012). *Nature* **490**, (2012).
 24. Elias, D. C., Nair, R. R., Mohiuddin, T. M. G., Morozov, S. V., Blake, P., Halsall, M. P., *et al.* Control of Graphene's Properties by Reversible Hydrogenation: Evidence for Graphane. *Science* **323**, 610-613 (2009).
 25. Balog, R., Jorgensen, B., Nilsson, L., Andersen, M., Rienks, E., Bianchi, M., *et al.* Bandgap opening in graphene induced by patterned hydrogen adsorption. *Nat Mater* **9**, 315-319 (2010).
 26. Forro, L., Mihaly, L. Electronic properties of doped fullerenes. *Reports on Progress in Physics* **64**, 649-699 (2001).
 27. Varma, C. M., Zaanen, J., Raghavachari, K. Superconductivity in the Fullerenes. *Science* **254**, 989-992 (1991).

Chapter 2

Theoretical Approaches

2.1. Introduction

The goal of this chapter is to review all computational methods that we used to understand thermal and charge carrier transport in the material. Recall that the thermoelectric figure of merit $ZT = \frac{S^2\sigma}{\kappa}T$ can be predicted with the three transport coefficients (σ , S and κ), and we demonstrated how these three properties are calculated with atomic-scale computer simulations.

2.2. Thermal Transport

In general, there are two computational approaches to compute the thermal transport of materials. One is based on the Boltzmann transport equation (BTE), which requires parameters obtained from measurements. The other is based on the fluctuation-dissipation relation from linear response theory.¹ For novel materials, measured parameters are not available, and accordingly the BTE cannot be used to compute thermal transport properties. In contrast, for molecular dynamics (MD) simulations, the only pre-required information to compute thermal transport coefficients is the interatomic interactions (force fields) for the system. It is not difficult to obtain high-quality force fields, which can be obtained from *ab initio* calculations and related to the experimental measurements.

In this thesis, we used equilibrium molecular dynamics (EMD) simulations to predict the

thermal transport properties of novel carbon-based materials, allowing us to understand the effects of various modifications on thermal transport in these materials. In order to analyze the properties of the main heat carriers in materials and understand how they depend on structural or chemical modifications (*e.g.*, chemical functionalization, introduction of defects and intercalation of metal atoms), we carried out a series of lattice dynamics calculations. We compute the group velocities and lifetimes of each phonon mode in order to quantify their contributions to the thermal conductivity.

2.2.1. Molecular Dynamics Simulations

The microscopic thermal conductivity (κ) of the material is defined from Fourier's law of heat flow under non-uniform temperature. κ is defined as the ratio of the heat current (\vec{J}_q) in the direction of heat flow and the local temperature gradient (∇T) along that direction:

$$\vec{J}_q = -\kappa \nabla T \quad (2.1)$$

In MD simulations, a system at equilibrium within the microcanonical ensemble (constant atom number, volume, and energy, or NVE) induces zero average heat flux. The lattice thermal conductivity can be obtained from the fluctuations of the heat current, using the Einstein relation,^{2,3} based on the fluctuation-dissipation theorem from linear response theory:¹

$$\kappa_\alpha = \frac{1}{k_B V T^2} \lim_{t \rightarrow \infty} \frac{1}{2t} \langle [R_\alpha(t) - R_\alpha(0)]^2 \rangle \quad (2.2)$$

where k_B is the Boltzmann constant, V the system volume and T the temperature, respectively.

$\langle [R_\alpha(t) - R_\alpha(0)]^2 \rangle$ is the mean square displacement of the integrated microscopic heat flux along the α direction, and the microscopic heat flux can be written as:

$$J_\alpha(r,t) = \frac{1}{V} \frac{dR_\alpha}{dt} = \frac{1}{V} \frac{d}{dt} \sum_i r_{i\alpha} \varepsilon_{i\alpha} \quad (2.3)$$

where r_i is the position of atom i , and the energy $\varepsilon_{i\alpha}$ can be expressed as:

$$\varepsilon_{i\alpha} = \frac{1}{2} m_i v_{i\alpha}^2 + W_{i\alpha} \quad (2.4)$$

where $v_{i\alpha}$ and $W_{i\alpha}$ are the velocity and the local potential energy assigned to atom i , respectively. For a many body interaction potential, such as the Tersoff potential⁴ and REBO potential,⁵ the heat current can then be expressed as follows:⁶

$$J = \frac{1}{V} \left[\sum_i^N \varepsilon_i v_i + \frac{1}{2} \sum_{i,j;i \neq j}^N (F_{ij} \cdot v_i) r_{ij} + \frac{1}{6} \sum_{i,j,k;i \neq j \neq k}^N (F_{ijk} \cdot v_i) (r_{ij} + r_{ik}) \right] \quad (2.5)$$

where F_{ij} and F_{ijk} are the two- and three-body forces. In this work, molecular dynamics was used to obtain the coordinates, velocities, and forces to compute the heat flux, employed within the LAMMPS package.⁷

Note that the thermal conductivity calculated here does not include the electronic contribution. The contribution to the thermal conduction in the above formulation only comes from the atomic vibrations, and is referred to as the lattice thermal conductivity (κ_l). The electronic thermal conductivity is computed separately, as explained in section 2.3.2.

2.2.2. Lattice Dynamics Simulations

In a crystal, the potential energy for the ions using the harmonic approximation, which neglects all powers of displacements larger than or equal to 3, can be written as:⁸

$$\phi(r_1, \dots, r_N) = \phi_0 + \sum_{ii'} \sum_{ll'} \sum_{\alpha\beta} u_\alpha(ii) \Phi_{\alpha\beta} u_\beta(i'l') \quad (2.6)$$

where $i(i')$, $l(l')$ and $\alpha(\beta)$ refer to the index of atom, unit cell and the cartesian component of its

displacement, respectively. The $u(il)$ is the displacement vector from the equilibrium position, and the Φ is the second derivative of the potential energy at the equilibrium position, called the force constant matrix:

$$\Phi_{\alpha\beta} \begin{pmatrix} ii' \\ ll' \end{pmatrix} = \frac{\partial^2 \phi}{\partial u_\alpha(il) \partial u_\beta(i'l')} \quad (2.7)$$

From the derivation of the potential, we can compute the force on each site with $F = -\frac{\partial \phi}{\partial u}$. The equation of motion for the i th atom in the l th unit cell is:

$$-\sum_{i'l'} \Phi_{\alpha\beta} \begin{pmatrix} ii' \\ ll' \end{pmatrix} u(i'l', t) = M_i \ddot{u}(il, t) \quad (2.8)$$

where M_i is the mass of the i th atom. The solution for $u(il, t)$ is a linear superposition of traveling harmonic waves with different wave vector \mathbf{q} and mode label ν :

$$u(il, t) = \sum_{\mathbf{q}, \nu} U(i, \mathbf{q}, \nu) \exp(i[\mathbf{q} \cdot r(il) - \omega(\mathbf{q}, \nu)t]) \quad (2.9)$$

where $r(il)$ is the position of the atom, and U is the displacement vector of the atom i in the reciprocal space. By substituting the Eq. 2.9 into the Eq. 2.8,

$$M_i \omega^2 U(i, \mathbf{q}, \nu) = \sum_{i'l'} \Phi_{\alpha\beta} \begin{pmatrix} ii' \\ 0l' \end{pmatrix} U(i', \mathbf{q}, \nu) \exp(i\mathbf{q} \cdot [r(i'l') - r(i0)]) \quad (2.10)$$

The equation of motion for a single solution can be expressed:

$$\omega^2(\mathbf{q}, \nu) e(\mathbf{q}, \nu) = D(\mathbf{q}) \cdot e(\mathbf{q}, \nu) \quad (2.11)$$

where D is the dynamical matrix as the $3n \times 3n$ matrix given by:

$$D_{\alpha\beta}(ii', \mathbf{q}) = \frac{1}{\sqrt{M_i M_{i'}}} \sum_{l'} \Phi_{\alpha\beta} \begin{pmatrix} ii' \\ 0l' \end{pmatrix} \exp(i\mathbf{q} \cdot [r(i'l') - r(i0)]) \quad (2.12)$$

The only nontrivial solutions are obtained with $\det(D(\mathbf{q}) - \omega^2 I) = 0$. For each \mathbf{q} , there are $3n$

(n is the number of atoms in the unit cell) different solutions (branches) with eigenvalues $\omega(\mathbf{q}, \nu)$. The dependence of these eigenvalues on \mathbf{q} is known as the dispersion relation. We compute and diagonalize the dynamical matrix (D) to obtain eigenvalues (phonon mode frequencies) and eigenvectors (phonon mode shape).

In our work, we have used lattice dynamics calculations to obtain the group velocities. The group velocities can be determined from the phonon dispersion around the Γ point of the Brillouin zone in a large supercell. We consider $0 \leq |\vec{q}| \leq 0.002 \text{ \AA}^{-1}$, where \vec{q} is a phonon wave vector and is spaced by 0.0001 \AA^{-1} . Approximating the dispersion curves by a quadratic function, the group velocity is obtained from the slope at $\vec{q} = 0.002 \text{ \AA}^{-1}$.

The phonon lifetime (τ_i) is computed from the integral of the normalized autocorrelation function of the kinetic energy fluctuation of the eigenmodes⁹

$$\tau_i = \int_0^\infty \frac{\langle \delta E_{i,k}(\vec{q}, t) \delta E_{i,k}(\vec{q}, 0) \rangle}{\langle \delta E_{i,k}(\vec{q}, 0) \delta E_{i,k}(\vec{q}, 0) \rangle} dt \quad (2.13)$$

where

$$E_{i,k}(\vec{q}, t) = \frac{A_i'^* A_i'}{2} \quad (2.14)$$

$$A_i(\vec{q}, t) = \sum_j \sqrt{M_j} e^{(-\vec{q} \cdot \vec{r}_{j,0})} \boldsymbol{\varepsilon}_i^*(\vec{q}) \cdot \mathbf{u}_j(t) \quad (2.15)$$

By projecting the atomic trajectories generated by MD simulations on the normal mode coordinates, we obtain a time history of the normal mode amplitudes $A_i(\vec{q}, t)$, which gives the mode kinetic energy, $E_{i,k}$. Here, M_j is the mass of the j -th atom, $r_{j,0}$ the equilibrium position, and u_j the relative displacement from its equilibrium position in our MD trajectories, respectively. $\boldsymbol{\varepsilon}_i$ is an eigenvector obtained from lattice dynamics calculation.

The contribution to κ from the i -th phonon mode (κ_i) is expressed in terms of group velocities

v_i and lifetimes τ_i , using the single mode relaxation time approximation of the Boltzmann transport equation¹⁰

$$\kappa_i(\vec{q}) = C_i(\vec{q})v_i^2(\vec{q})\tau_i(\vec{q}) \quad (2.16)$$

Here C_i is the specific heat per unit volume of the i -th phonon mode from the Bose-Einstein statistics,

$$C_i(\vec{q}) = \frac{1}{V}k_b x^2 \frac{e^x}{(e^x - 1)^2} \quad (2.17)$$

where $x = \hbar\omega_i(\vec{q})/k_bT$, and $\omega_i(\vec{q})$ is the phonon frequency.

2.3. Charge Carrier Transport

Electronic structure plays an important role in understanding properties of materials, in particular, their charge carrier transport properties. In this thesis, we employ first-principles atomistic calculations, within the framework of density functional theory (DFT), to obtain the electronic structure of the various materials considered. In addition, by employing semi-classical Boltzmann transport theory, we calculated the transport coefficients (σ , S and κ_e), which are needed to predict the full thermoelectric figure of merit ZT .

2.3.1. Density Functional Theory

Density functional theory is based on universal quantum mechanical principles, and broadly speaking is an approach to reduce the intractable Schrödinger equation, governing 10^{23} electrons, to a single-particle effective theory. DFT enables the accurate prediction of a wide range of materials properties (*e.g.*, electronic, structural, mechanical, spectroscopic and magnetic) in many-body systems. DFT is founded on the Hohenberg-Kohn theorem.¹¹ This

theorem states that many-body interactions can be described by a unique ground state electron density, $n(\mathbf{r})$, of a system, which in turn can determine all quantities of interest in the ground state, including the total energy. Accordingly, the kinetic and Coulomb energies of a system are functionals, *i.e.*, functions of another function, $E[n(\mathbf{r})]$ of the charge density $n(\mathbf{r})$. On this basis, the ground-state energy for the electronic system can be derived by minimizing the energy functional $E[n(\mathbf{r})]$. However, the functional is unknown, and approximate forms need to be employed in DFT. Kohn and Sham (KS)¹² introduced the Schrödinger equation of a fictitious non-interacting system of N electrons that generate the same ground-state density as the system of interacting N electrons, and this KS equation is:

$$\left(-\frac{\hbar^2}{2m}\nabla^2 + v_{ext}(\mathbf{r}) + v_H[n(\mathbf{r})] + v_{xc}[n(\mathbf{r})] \right) \phi_{nk} = \varepsilon_{nk} \phi_{nk} \quad (2.18)$$

This KS Hamiltonian is given by the sum of the kinetic energy $-\frac{\hbar^2}{2m}\nabla^2$, the external potential v_{ext} from the nuclei, the Hartree potential v_H for the repulsive interaction of the electron, and the exchange correlation potential v_{xc} including all electron-electron interaction beyond the Hartree term. The ϕ_{nk} are KS orbitals, the ε_{nk} are KS eigenvalues, the n and k are a band index and a vector in the Brillouin zone in the case of using a plane wave basis set. Since the exchange correlation potential is also unknown, a large number of possible approximations are developed for E_{xc} . Two most common local forms of v_{xc} are the Local Density Approximation (LDA) and Generalized Gradient Approximation (GGA). These approximations can produce highly accurate ground state energies and related properties in materials. In this thesis, DFT is performed using the plane-wave basis VASP code.¹³

2.3.2. Boltzmann Transport Theory

For general particle transport in semiconductors, the appropriate formalism to use is the Boltzmann transport equation (BTE). Applying this equation, transport properties, particularly thermoelectric properties, are calculated from the electronic structure calculated from DFT.

The Boltzmann transport equation (BTE) describes the statistical behavior of a system, which is not in thermodynamic equilibrium, by following the time evolution of the electron distribution function $f_i(\vec{r}, \vec{k}, t)$. The $f_i(\vec{r}, \vec{k}, t)$ is the probability of having an electron at position \vec{r} at a given time t with wave vector \vec{k} , and we would obtain the total number of electrons by integrating this distribution function. Once $f_i(\vec{r}, \vec{k}, t)$ is determined, all other properties of the system can be computed, which is why BTE is considered a fundamental description of a physical system. The time variation of this distribution is due to three effects: diffusion, drift and scattering. Diffusion is caused by any gradient in the electron concentration, and drift is caused by an external field. The time evolution of the distribution function is given by the Boltzmann transport equation:

$$\begin{aligned} \frac{\partial f_i(\vec{k})}{\partial t} &= \left(\frac{\partial f_i(\vec{k})}{\partial t} \right)_{diffusion} + \left(\frac{\partial f_i(\vec{k})}{\partial t} \right)_{drift} + \left(\frac{\partial f_i(\vec{k})}{\partial t} \right)_{scattering} \\ &= -v(\vec{k}) \cdot \frac{\partial f_i(\vec{k})}{\partial \mathbf{r}} - \dot{\vec{k}} \cdot \frac{\partial f_i(\vec{k})}{\partial \vec{k}} + \left(\frac{\partial f_i(\vec{k})}{\partial t} \right)_{scattering} \end{aligned} \quad (2.19)$$

where i is the band index, and \vec{r} is omitted for simplicity. It is difficult to solve Eq. 2.19 since it is an integro-differential equation. Within the scope of this thesis, we applied the relaxation-time approximation (RTA),¹⁴ assuming the scattering term as:

$$\left(\frac{\partial f_i(\vec{k})}{\partial t} \right)_{scattering} = -\frac{f_i(\vec{k}) - f_i^0(\vec{k})}{\tau_i(\vec{k})} \quad (2.20)$$

where $f_i(\vec{k})$ is the local concentration of electrons in the state (i, \vec{k}) , which is assumed to deviate not far from the equilibrium distribution, and $f_i^0(\vec{k})$ is the equilibrium distribution given by the Fermi-Dirac function. $\tau_i(\vec{k})$ is the carrier's relaxation-time from $f_i(\vec{k})$ to $f_i^0(\vec{k})$ when the external field is removed.

Under the steady state condition, the right side of Boltzmann's transport equation becomes zero. When considering only a weak external DC electric field, the diffusion term can be neglected, and the drift term becomes

$$\left(\frac{\partial f_i(\vec{k})}{\partial t} \right)_{drift} = -\dot{\vec{k}} \frac{\partial f_i(\vec{k})}{\partial \vec{k}} = \frac{e}{\hbar} \vec{E} \cdot \nabla_{\vec{k}} f_i(\vec{r}, \vec{k}, t) \quad (2.21)$$

Then Eq. 2.19 becomes

$$-\frac{e}{\hbar} \vec{E} \cdot \nabla_{\vec{k}} f_i(\vec{k}) = \left[\frac{\partial f_i(\vec{k})}{\partial t} \right]_{scatt} \quad (2.22)$$

where \vec{E} is the external electric field. Substituting Eq. 2.20 into Eq.2.21, and neglecting the second-order term, the electron distribution is given as:

$$f_i(\vec{k}) \approx f_i^0(\vec{k}) - e\tau_i(\vec{k}) \left(-\frac{\partial f_i^0(\vec{k})}{\partial \epsilon_i(\vec{k})} \right) \vec{E} \cdot \vec{v}_{ik} \quad (2.23)$$

2.3.3. Semi-classical Theory – Transport Coefficients

The goal of our work is to calculate macroscopic quantities, such as electrical and thermal conductivity, and we need to determine how to relate $f_i(\vec{r}, \vec{k}, t)$ to these quantities. Here, we can apply the microscopic and macroscopic Ohm's law, which relate the current density to the applied electric field and temperature gradient. The number of electrons per unit volume in the

volume element $d\vec{k}$ is $f_i(\vec{k})d\vec{k}/4\pi^3$, and according to the microscopic Ohm's law the current density (\mathbf{j}) in a band i is given as:

$$\mathbf{j} = -e \sum_i \int \frac{d\vec{k}}{4\pi^3} v(\vec{k}) f_i(\vec{k}) \quad (2.24)$$

In addition, the thermal current density \mathbf{j}^q is given as:¹⁵

$$\mathbf{j}^q = \sum_i \int \frac{d\vec{k}}{4\pi^3} [\varepsilon_i(\vec{k}) - \mu] v_i(\vec{k}) f_i(\vec{k}) \quad (2.25)$$

The distribution function $f_i(\vec{k})$ in the presence of a uniform static electric field and temperature gradient can be written as:

$$f(\vec{k}) \approx f^0(\vec{k}) + \tau(\varepsilon(\vec{k})) \left(-\frac{\partial f^0}{\partial \varepsilon} \right) v(\vec{k}) \cdot \left[-e\vec{E} + \frac{\varepsilon(\vec{k}) - \mu}{T} (-\nabla T) \right] \quad (2.26)$$

According to the macroscopic version of Ohm's law, the current density \mathbf{j} and thermal current density \mathbf{j}^q are given as:

$$\begin{aligned} \mathbf{j} &= L^{11} \vec{E} + L^{12} (-\nabla T) \\ \mathbf{j}^q &= L^{21} \vec{E} + L^{22} (-\nabla T) \end{aligned} \quad (2.27)$$

With the above distribution function (Eq.2.26), the matrices L^{ij} are defined in terms of the transport coefficient function $L^{(\alpha)}$:

$$L^{(\alpha)} = e^2 \int \frac{d\vec{k}}{4\pi^3} \left(-\frac{\partial f^0}{\partial \varepsilon} \right) \tau(\varepsilon(\vec{k})) v(\vec{k}) v(\vec{k}) |\varepsilon(\vec{k}) - \mu|^\alpha \quad (2.28)$$

$$L^{11} = L^{(0)}$$

$$L^{21} = TL^{12} = -\frac{1}{e} L^{(1)}$$

$$L^{22} = \frac{1}{e^2 T} L^{(2)}$$

where e is the electronic charge, $\tau(\varepsilon(\vec{k}))$ the energy-dependent relaxation time, $v(\vec{k}) = (1/\hbar)\nabla_{\vec{k}}\varepsilon(\vec{k})$ the group velocity in the n th band at \vec{k} , $\varepsilon(\vec{k})$ the energy eigenvalues obtained from DFT, μ the chemical potential, and f^0 the Fermi-Dirac function at a given temperature T .

We can identify the electrical conductivity (σ), the Seebeck coefficient (S), and the electronic thermal conductivity (κ_e) as:

$$\begin{aligned}\sigma &= L^{11} = L^{(0)} \\ S &= -\frac{d\bar{E}}{dT} = -\frac{d\bar{E}/dx}{dT/dx} = \frac{L^{12}}{L^{11}} = -\frac{1}{eT}(L^{(0)})^{-1}L^{(1)} \\ \kappa_e &= L^{22} - \frac{L^{21}L^{12}}{L^{11}} = \frac{1}{e^2T}(L^{(2)} - L^{(1)}(L^{(0)})^{-1}L^{(1)})\end{aligned}\quad (2.29)$$

In this thesis, we employed a rigid band model, which assumes that electronic band structure is not affected by doping, and the above transport coefficients are calculated using the BoltzTrap package of Madsen and Singh.¹⁶

2.3.4. Relaxation Time

In general, the relaxation time (τ) is taken to be energy-independent, and obtained by fitting experimental values for pristine bulk materials even in the cases with structural and chemical modifications. However, in principle τ is a complex function of the electron energy, temperature, and atomic structure. Since the goal of our work is to determine the quantitative effects of various modifications of materials, we do not make the assumption of using a bulk τ for the nanostructured materials; rather, we calculated explicitly the relaxation time within Boltzmann transport theory in order to accurately predict thermoelectric properties.

The most important sources of scattering in typical semiconductor are the electron-phonon collisions and perturbing fields from ionized impurities. To obtain the scattering rates, the perturbing potential needs to be identified. Once the potential is known, the scattering rate $S(\mathbf{k}, \mathbf{k}')$ can be determined using Fermi's Golden Rule:

$$S(\mathbf{k}, \mathbf{k}') = \frac{2\pi}{\hbar} |H(\mathbf{k}, \mathbf{k}')|^2 \delta(E(\mathbf{k}') - E(\mathbf{k})) \quad (2.30)$$

$$H(\mathbf{k}, \mathbf{k}') = \langle \varphi_{n\mathbf{k}'} | U(\mathbf{r}) | \varphi_{n\mathbf{k}} \rangle$$

where $\varphi_{n\mathbf{k}}$ and $\varphi_{n\mathbf{k}'}$ are the wave functions before and after encountering the potential $U(\mathbf{r})$, respectively. $H(\mathbf{k}, \mathbf{k}')$ is the matrix element which couples those wave functions together.

When the scattering rate is known, the relaxation time can be computed from:

$$\frac{1}{\tau} = \sum_{\mathbf{k}'} S(\mathbf{k}, \mathbf{k}') |1 - \cos \theta_{\mathbf{k}\mathbf{k}'}| \quad (2.31)$$

where $\theta_{\mathbf{k}\mathbf{k}'}$ is the scattering angle between \mathbf{k} and \mathbf{k}' .

In this thesis, we model the intrinsic transport properties of carbon-based materials, and will only incorporate acoustic phonon scattering. Acoustic phonons change the local lattice constant, and this deviation from periodicity of the lattice can scatter electrons. Here, only longitudinal phonons can scatter electrons since only these modes can create volume changes in the lattice. The perturbing potential has a linear dependence on the relative volume change:

$$U_{ac} = D_{ac} \nabla \cdot \mathbf{u} \quad (2.32)$$

where D_{ac} is defined as the deformation-potential coupling constant, and \mathbf{u} is the displacement of the phonon. The scattering rate for quasielastic scattering on acoustic phonons :

$$S(\mathbf{k}, \mathbf{k}') = \frac{2\pi}{\hbar} \sum_{\mathbf{q}} |H(\mathbf{k}, \mathbf{k}')|^2 [N_{\mathbf{q}} \delta(E(\mathbf{k}') - E(\mathbf{k}) + \omega_{\mathbf{q}}) + (N_{\mathbf{q}} + 1) \delta(E(\mathbf{k}') - E(\mathbf{k}) - \omega_{\mathbf{q}})] \quad (2.33)$$

where $H(\mathbf{k}, \mathbf{k}')$ is the matrix element for scattering by acoustic phonons, $\omega_{\mathbf{q}}$ is the acoustic phonon frequency expressed in terms of the sound velocity v_{ph} ($\omega_{\mathbf{q}} = v_{ph} \mathbf{q}$), and $N_{\mathbf{q}}$ is the equilibrium distribution of phonons given by the Bose-Einstein distribution function $N_{\mathbf{q}} = 1/[\exp(\hbar\omega_{\mathbf{q}}/k_B T) - 1]$. For isotropic scattering, the square of the electron-phonon coupling $|H(\mathbf{k}, \mathbf{k}')|^2$ can be expressed as $|H(\mathbf{k}, \mathbf{k}')|^2 = \frac{\hbar \mathbf{q}}{2V \rho_m v_{ph}} D_{ac}^2 N_{\mathbf{q}}$, where ρ_m is the mass density, and V is the volume of the sample. For the temperature range we are interested in ($\hbar\omega_{\mathbf{q}} \ll k_B T$), $N_{\mathbf{q}} \sim k_B T / \hbar\omega_{\mathbf{q}} \gg 1$. The resulting relaxation time for acoustic phonons is given as:

$$\frac{1}{\tau} = \frac{\pi D_{ac}^2 k_B T}{\hbar \rho_m v_{ph}^2} D(E) \quad (2.34)$$

This form highlights the proportionality of the scattering rate to the density of states $D(E)$.

References

1. Kubo, R., Toda, M., Hashitsume, N. Statistical Physics II Nonequilibrium Statistical Mechanics. *Springer Series in Solid-State Sciences*, Berlin, Heidelberg: Springer Berlin Heidelberg,; 1985. p. 1 online resource.
2. Weitz, D. A., Pine, D. J., Pusey, P. N., Tough, R. J. A. Nondiffusive brownian-motion studied by diffusing-wave spectroscopy. *Phys Rev Lett* **63**, 1747-1750 (1989).
3. Viscardy, S., Servantie, J., Gaspard, P. Transport and helfand moments in the lennard-jones fluid. II. Thermal conductivity. *J Chem Phys* **126**, 184513 (2007).
4. Tersoff, J. New Empirical-Approach for the Structure and Energy of Covalent Systems. *Phys Rev B* **37**, 6991-7000 (1988).
5. Brenner, D. W., Shenderova, O. A., Harrison, J. A., Stuart, S. J., Ni, B., Sinnott, S. B. A second-generation reactive empirical bond order (REBO) potential energy expression for hydrocarbons. *Journal of Physics-Condensed Matter* **14**, 783-802 (2002).
6. Volz, S. G., Chen, G. Molecular-dynamics simulation of thermal conductivity of silicon crystals. *Phys Rev B* **61**, 2651-2656 (2000).
7. Plimpton, S. Fast Parallel Algorithms for Short-Range Molecular-Dynamics. *J Comput Phys* **117**, 1-19 (1995).
8. Dove, V. T. Introduction to the theory of lattice dynamics. *Microscopic Properties and Processes in Minerals* **543**, 281-297 (1999).
9. Ladd, A. J. C., Moran, B., Hoover, W. G. Lattice Thermal-Conductivity - a Comparison of Molecular-Dynamics and Anharmonic Lattice-Dynamics. *Phys Rev B* **34**, 5058-5064 (1986).
10. McGaughey, A. J. H., Kaviani, M. Quantitative validation of the Boltzmann transport equation phonon thermal conductivity model under the single-mode relaxation time approximation. *Phys Rev B* **69**, 094303

- (2004).
11. Hohenberg, P., Kohn, W. Inhomogeneous Electron Gas. *Phys Rev B* **136**, B864-+ (1964).
 12. Kohn, W., Sham, L. J. Self-Consistent Equations Including Exchange and Correlation Effects. *Physical Review* **140**, 1133-& (1965).
 13. Kresse, G., Furthmuller, J. Efficient iterative schemes for ab initio total-energy calculations using a plane-wave basis set. *Phys Rev B* **54**, 11169-11186 (1996).
 14. Ziman, J. M. *Principles of the theory of solids*, 2d edn. University Press: Cambridge Eng., 1972.
 15. Ashcroft, N. W., Mermin, N. D. *Solid state physics*. Holt: New York., 1976.
 16. Madsen, G. K. H., Singh, D. J. BoltzTraP. A code for calculating band-structure dependent quantities. *Comput Phys Commun* **175**, 67-71 (2006).

Chapter 3

Thermal Transport in Functionalized Graphene

3.1. Introduction to Thermal Transport in Functionalized Graphene

Graphene has attracted intense attention for both its superior carrier mobility at room temperature and unique zero-gap band structure, which leads to massless charge carriers.^{1,2} In addition to these remarkable electronic properties, there have been recent attempts to use graphene for thermoelectric (TE) applications^{3,4} due to its low dimensional structure and ambipolar nature, controlling the sign of the Seebeck coefficient (S) by changing the gate bias instead of doping. The efficiency of a TE material is determined by its figure of merit, $ZT = S^2\sigma T/\kappa$, where S is the Seebeck coefficient, σ the electrical conductivity, κ the thermal conductivity, and T the temperature, respectively. For a pristine graphene monolayer the TE properties have been studied both theoretically⁵⁻⁷ and experimentally,⁸⁻¹⁰ with reported values for S as high as 100 $\mu\text{V/K}$, suggesting the potential of graphene as a candidate material for TE applications. However, because of its extremely high κ ,¹¹⁻¹³ bare graphene is overall a highly inefficient TE material.⁸ Thus, in order to create an efficient ZT material based on graphene, a significant reduction in the thermal conductivity is required.

One way to suppress the thermal conductivity of graphene, or nearly any material, would be to introduce point defects such as interstitials, vacancies or by alloying. However, if the goal is to

explore thermoelectric applications, one must balance reduced thermal conductivity against the need for a large power factor ($S^2\sigma$). Unlike a range of other promising classes of thermoelectric materials that utilize controlled defects (phonon-glass) as phonon scattering sites by taking advantage of inherent “electron-crystal” properties in the materials, including skutterudites¹⁴ and clathrates,¹⁵ the introduction of *controlled* “rattling structures” into a graphene sheet would be pose an enormous synthesis challenge. The use of less controlled defects such as vacancies¹⁶ or substitutional impurities¹⁷ would of course lower the thermal conductivity but they would also lower the power factor by so much that such an approach is unlikely to be relevant to the case of graphene-based thermoelectrics. Introduction of isotope disorder and isotope patterns would be a method of reducing thermal conductivity of graphene without degrading electron transport; however, because of the relatively marginal thermal conductivity reduction, by only a factor of two,¹⁸ such approaches also have not led to significant increases in ZT.

Another way to suppress the thermal conductivity of a material is to reduce its dimensionality, *e.g.*, by using quantum wires or superlattices.¹⁹⁻²¹ Recent theoretical studies have shown that the thermal conductivity of a graphene nanoribbon (GNR) can be suppressed by several orders of magnitude compared to graphene due to its edge disorder,^{4,22-24} which is introduced during fabrication. However, owing to several obstacles to producing GNR-based devices, including the challenge of reliable production of GNRs with controlled width distributions and the manipulation required for assembling as-produced GNRs into devices,²⁵ it would be advantageous to develop approaches to reducing the thermal conductivity of graphene that do not rely on physical cutting or etching. Towards this end, graphene superlattices made with chemical functionalization are of great interest, and have been explored recently due to the possibility to nanostructure graphene into complex patterns.²⁵⁻²⁹ Functionalization also leads to tunable

electronic properties by opening the energy gap of graphene, originating from the induced changes in the hybridization of carbon atoms from sp^2 to sp^3 .^{25,27-29} It is therefore of great interest to further explore the potential of graphene superlattices made with chemical functionalization for TE applications, in particular the role of such functionalization on thermal transport properties.

Among various kinds of pattern shapes, we focus in this work on 2D periodic line patterns to produce graphene “nano-roads”,²⁵ which are in a sense a mixture of pristine GNRs and GNRs with full functionalization within the same sheet. Such partial functionalization generates patterned sp^3 hybridized carbon regions with well-defined boundaries between the sp^2 (pristine GNR) and sp^3 (functionalized GNR) domains. The key question for such materials regarding TE applications is whether their thermal conductivity can be efficiently suppressed due to the phonon scattering at these boundaries without severely degrading the electronic properties of the pristine monolayer.

3.2. Thermal Conductivity of Chemically Functionalized Graphene

Molecular dynamics (MD) simulations are employed within the LAMMPS package³⁰ to compute thermal conductivities for all of the systems considered in this work. The thermal conductivity is computed as a function of a range of pattern widths and functional groups (H and hydrocarbon chains). The volume is calculated as the product of the unit cell planar area times the interplanar distance (3.35 Å). To describe the covalent bonding interactions in the carbon and hydrocarbon systems, we used the second-generation reactive empirical bond order (REBO)³¹ potential, which has been successfully used in many carbon-based systems, such as carbon nanotubes and graphene, for thermal transport studies.³²⁻³⁴ All simulations are carried out at 300

K with a time step of 0.2 fs. To obtain converged results, 10 separate simulations are averaged for each system, each with different initial conditions. In each run, after a 100 ps equilibration period, the microscopic heat flux in the directions perpendicular and parallel to the functionalization pattern are recorded for 10^7 MD steps (2 ns) in order to obtain a converged thermal conductivity value.

3.2.1. Pristine Graphene

In order to investigate the convergence properties of thermal conductivity (κ) as a function of graphene sheet size, we compute κ values of approximately square graphene sheets ranging in size from 20 to 500 Å (corresponding to 200 - 92000 atoms in the simulation cell) with two different potentials; optimized Tersoff³⁵ and REBO³¹ potential. We find that for sizes larger than 5 nm, our MD results are relatively independent and converge to the values of 1000 W/mK and 350 W/mK with optimized Tersoff and REBO potential, respectively. These results are in good agreement with previous simulation results using the optimized Tersoff and REBO potential.³²⁻³⁴ These values are smaller than measured κ values for suspended graphene monolayer (3000~5000 W/mK)^{11,12} due to the small simulation cell size compared with the micrometer-size graphene monolayer. However, this size difference is not important for our current study because it does not change the influence of the functionalization on the graphene thermal transport. Our main goal in this part of the thesis is not to calculate the exact κ value of graphene but rather to obtain relative changes to κ values caused by different chemical functionalizations. Thus, we choose relatively small simulation cells (5 nm) for all subsequent simulations to study the effects of chemical functionalization on thermal transport in graphene. Although the optimized Tersoff potential exhibits closer κ values to the previous measurements,

we choose the REBO potential in order to describe better the covalent bonding interactions in the carbon and hydrocarbon systems. In a subsequent section, when our aim is to predict quantitatively the full ZT in functionalized graphene, we will employ corrections to the thermal conductivities computed here.

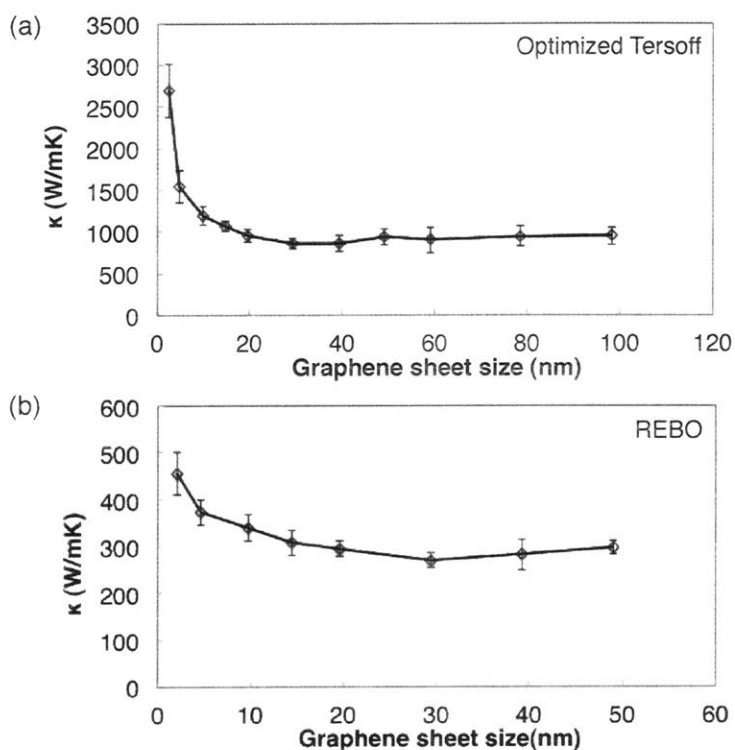


Figure 3.1 | Thermal conductivities of square graphene sheets as a function of graphene sheet size, with (a) optimized Tersoff potential and (b) REBO potential.

3.2.2. Chemically Functionalized Graphene

In our simulations, patterned graphene nano-roads are formed *via* partial functionalization of graphene sheets with the armchair-type of interface, which has a geometry that remains completely flat upon structural relaxation (see Figure 3.2a).²⁵ Graphene is functionalized with H atoms and hydrocarbon chains (pentane C_5H_{12} , referred to as C5) on both sides of the sheet in an alternating manner.³⁶ While H atoms can be attached to each C site of graphene to make

graphene (see Figure 3.2b),²⁹ it is not possible to functionalize graphene with C5 chains in the same fashion as for H atoms due to the steric repulsion between the chains (see Figure 3.2c).³⁷ Thus, we model the densest packing of C5 chains on graphene possible, given the possible bonding configurations available in the graphene lattice, namely a close-packed array of C5 chains separated by 4.2 Å as shown in Figure 3.2c. In the functionalized graphene, we define the pattern coverage as W_p / W_g , where W_p and W_g are the functionalized and total graphene widths in the unit cell, respectively.

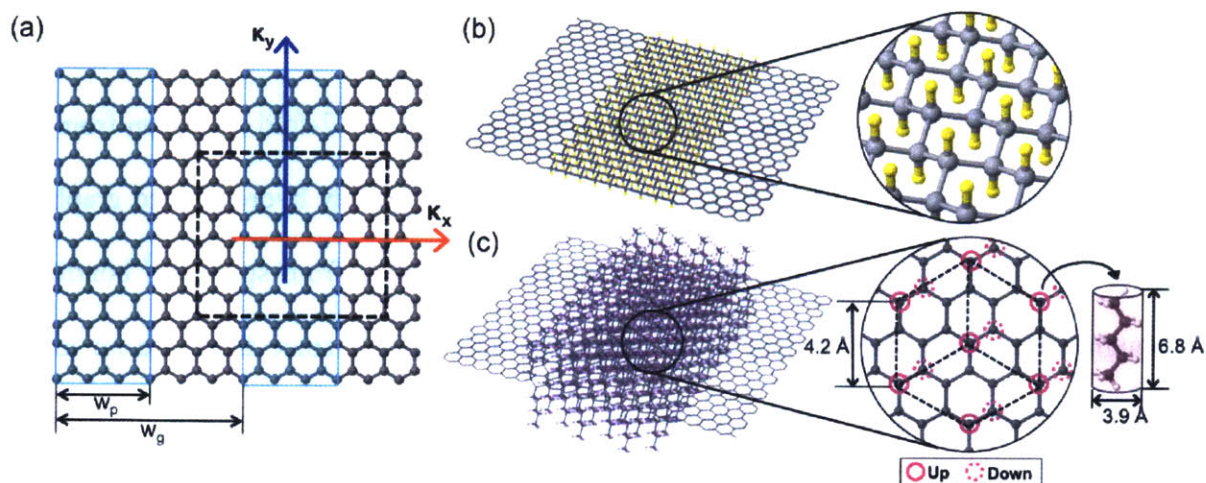


Figure 3.2 | Chemically functionalized graphene with H atoms and hydrocarbon chains. (a) Schematic representation of a patterned graphene sample with an armchair-type boundary along with structural variables used in the calculations. Blue shaded area indicates the patterned region, and the black dotted square represents the MD simulation unit cell. (b) The unit cell of H-functionalized graphene with graphene structure (inset). (c) C5-functionalized graphene. The inset shows the C sites of graphene where C5 chains are attached, arranged in a two-dimensional hexagonal close-packed lattice, as well as the structure of C5 (Pentane: C_5H_{12})

3.2.2.1. H-Functionalized Graphene

Figure 3.3 shows our computed values of κ_x and κ_y (perpendicular and parallel to the pattern boundary, respectively) for hydrogen-functionalized graphene as a function of pattern coverage.

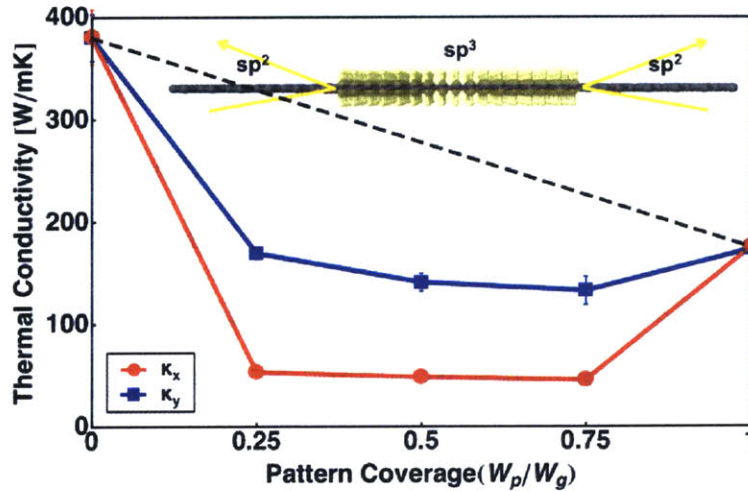


Figure 3.3 | Thermal conductivities of HG samples both perpendicular (red) and parallel (blue) to the pattern as a function of H pattern coverage. Black dotted line corresponds to the predicted κ_y from the rule of mixtures.

In the case of H-functionalization (HG), κ_x shows a more than 7-fold reduction from that of bare graphene over a wide range of coverage except for the fully hydrogenated graphene, which is lower than that of graphene due to the full conversion from sp^2 to sp^3 bonding,³⁸ although substantially higher than intermediate coverage values since there are no longer boundary scattering effects. For thermal transport parallel to the boundary one might expect a simple rule of mixtures to apply, although our computed values for κ_y are 2X lower than what would be expected and even lower than κ of graphane, slightly decreasing with the pattern coverage. This reduction is due to the presence of a well-defined boundary between pristine graphene (sp^2) and graphane (sp^3), where the acoustic mismatch at the interface gives rise to incoherent scattering, particularly for high frequency modes,³⁹ and scattered phonons reduce κ_y below the predictions from the rule of mixtures.

However, for partial coverage values, κ_x is essentially constant and substantially further reduced compared to κ_y . In addition to the effects of boundary scattering, the acoustic mismatch between pristine graphene and graphane also gives rise to a phonon confinement

effect, which partially localizes low frequency phonon modes³⁹ within the graphene or graphane domains, further reducing the thermal conductivity in the perpendicular direction by a factor of 3 compared to the parallel direction. This phenomenon has been observed in previous studies of in-plane thermal transport in superlattices, where it has been shown that phonon confinement arises from the acoustic mismatch at the boundary resulting in a modified dispersion with lower group velocity.^{40,41} Interestingly, in contrast to these other materials systems, in the case of hydrogenated graphene it is the structural difference (*i.e.*, sp^2 vs. sp^3) that causes the acoustic mismatch, not a large mass difference between the two domains. Note that for partial coverage values, κ_x is nearly independent of the pattern coverage due to the fact that the boundary region per unit area is a constant (0.4 /nm), which leads to near-constant boundary scattering and phonon confinement effects. Therefore, in HG cases, the large κ reduction in both directions mainly arises from the presence of the sharp boundary between graphene and graphane domains.

3.2.2.2. C5-Functionalized Graphene

When graphene is functionalized with patterns of C5 chains (C5G), both κ_x and κ_y are further reduced from those of HG (see Figure 3.4a), with the lowest κ value predicted to be 22 times smaller than that of pristine graphene at full coverage. It is interesting to note that the behavior of κ with pattern coverage for the C5G case is considerably different compared to the HG case. This can be explained from the different type of functionalization that results in un-functionalized carbon atoms in the patterned region around the C5 chains due to the steric repulsion between chains (see Figure 3.2c). This functionalization can generate two thermal conductivity reduction mechanisms, each of which can lead to a strong decrease: a clamping effect and scattering between sp^2 and sp^3 carbon in the patterned region. The C5

chains give rise to cuboid-shaped regions on both sides of graphene, which effectively clamp the graphene sheet from both sides due to a combination of the heavy mass (71 times larger than H) and large steric volume of the C5 chains.

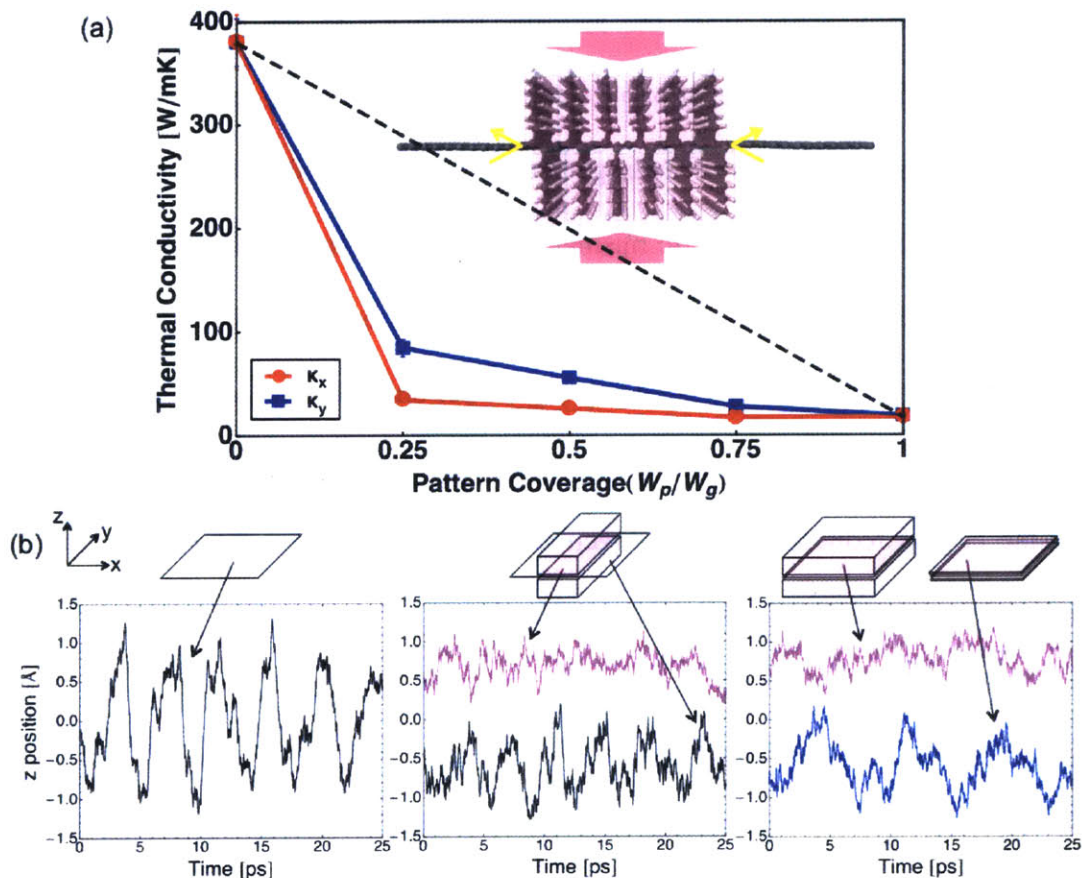


Figure 3.4 | Thermal conductivities of C5G samples as a function of C5 pattern coverage. (a) Black dotted line is for the predicted κ_y from the rule of mixtures. (b) z position vs. time of carbon atoms in pristine graphene (left), partially functionalized C5G (middle), and fully functionalized C5G (right) with schematic figures of our graphene samples (black arrows). The black (pink) solid lines indicate the fluctuation of un-patterned (patterned) regions. The blue line in the plot on the right is for the graphene functionalized with “fake” (heavy) hydrogen atoms.

In order to investigate this clamping effect, we calculate the atomic fluctuation of carbon atoms along the z direction in each system. As shown in Figure 3.4b, the fluctuation in the fully functionalized C5G system shows damped behavior compared to the bare graphene

system, and this damped phonon wave indicates considerably suppressed out-of-plane (ZA) phonon modes in graphene; it has been shown theoretically that as much as 77% of the total thermal conductivity in graphene at room temperature is due to the ZA modes.^{8,42}

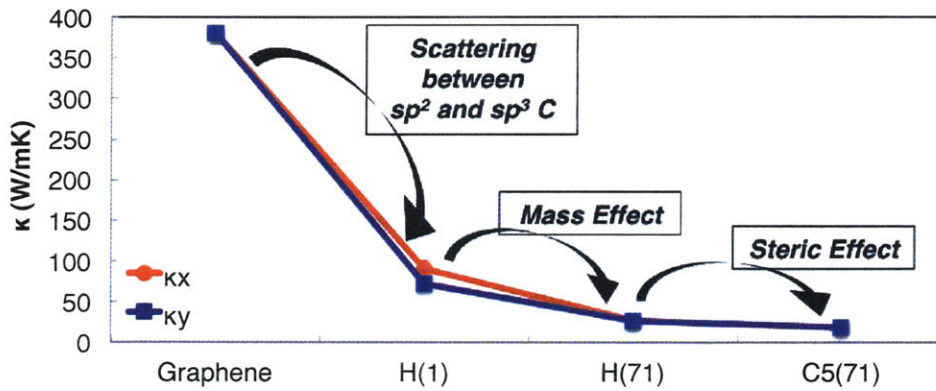


Figure 3.5 | Thermal conductivities of fully functionalized graphene as a function of functional groups (hydrogen atom, “fake” hydrogen atom and C5 chains). Relative changes of each sample are related to the each κ reduction effects in fully functionalized C5G system as indicated.

The clamping effect consists of two contributions: steric and mass effects. In order to separate all three of the thermal conductivity reduction effects (scattering between sp^2 and sp^3 C, mass and steric) in the fully functionalized C5G system, we carried out simulations with hydrogen atoms, “fake” hydrogen atoms that have the same mass as a C5 chain but do not have any steric effects and C5 chains as can be seen in Figure 3.5. From these results, we calculate the contribution of each effect using this relation.

$$\begin{array}{l}
\kappa_{\text{graphene}} \\
\kappa_{\text{H1}} \\
\kappa_{\text{H71}} \\
\kappa_{\text{C5}}
\end{array}
\begin{array}{l}
\curvearrowright \\
\curvearrowright \\
\curvearrowright \\
\curvearrowright
\end{array}
\begin{array}{l}
\times 1/r_{\text{scatter}} \\
\times 1/r_{\text{mass}} \\
\times 1/r_{\text{steric}}
\end{array}
\begin{array}{l}
\rightarrow -\log r_{\text{scatter}} \\
\rightarrow -\log r_{\text{mass}} \\
\rightarrow -\log r_{\text{steric}}
\end{array}$$

$$c_i = \frac{\log r_i}{(\log r_{\text{scatter}} + \log r_{\text{mass}} + \log r_{\text{steric}})}$$

where i = scatter, mass or steric effect. We find that 50 % of the reduction in thermal conductivity for the case of C5-functionalized graphene arises from the scattering between sp^2 and sp^3 C, and the other 50 % reduction, defined here as a “clamping” effect, arises from a combination of the mass (35 %) and steric (15 %) effects. This result shows that roughly 70 % of the clamping effect arises from the heavier mass of the C5 chains, and 30 % arises from the steric volume of the C5 chains. We note that out-of-plane fluctuations in graphene with “fake” hydrogen atoms (mass effect) are larger than those in the C5G system (which contains both mass + steric effects), although smaller than the fluctuations in bare graphene, as expected given our results for κ . In addition to the clamping effect, the other 50 % reduction in thermal conductivity arises from the scattering between sp^2 and sp^3 carbon. Note that there is no sharp boundary between these regions in the C5G case, although unlike in the HG case, the scattering between sp^2 and sp^3 carbon occurs both between the patterned and un-patterned regions as well as within the patterned region itself.

For partially functionalized C5G samples, κ_y is approximately 3.5 times lower than what would be expected from a simple rule of mixtures, due to spatial confinement of the phonons in the un-patterned region (see Figure 3.6), which arises from the clamped boundary between the patterned and un-patterned regions. This can be explained by the damped fluctuation in un-patterned regions compared to that in the pristine graphene sample (see Figure 3.4b).

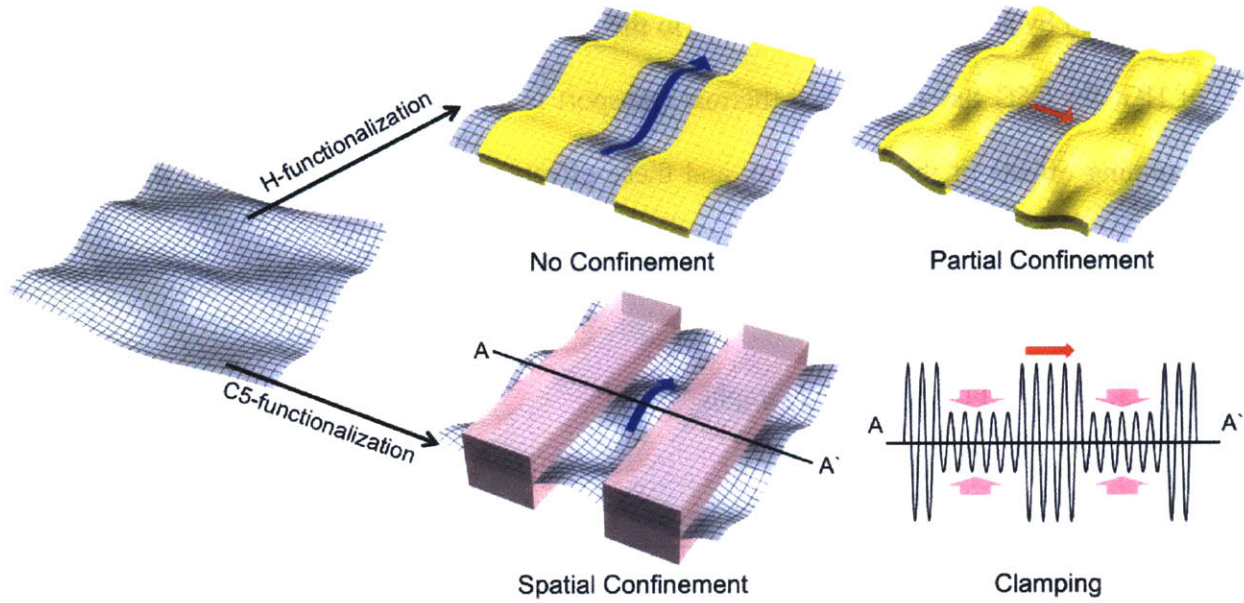


Figure 3.6 | Schematic of phonon confinement effects in graphene with the two different functionalizations considered in this work: hydrogen (upper) and C5 chain (lower). H-functionalization induces partial confinement of phonon modes in both the graphene and graphane domains, and suppresses thermal transport perpendicular to the boundary in HG samples. Modes with no confinement can propagate in all domains, and have no effect on thermal transport. C5-functionalization induces spatial confinement due to a clamping effect in the functionalized domain, which suppresses thermal transport parallel to the pattern. The lower right image indicates phonon waves along the AA' line in the C5G sample; waves in the patterned region (pink arrows) are damped due to the clamping effect, and this partially damped wave suppresses thermal transport in the perpendicular direction. Blue (red) arrows indicate heat transport along parallel (perpendicular) direction to the pattern boundary.

With increasing C5 pattern coverage, κ_y reduces further due to the increased spatial confinement with decreased un-patterned region width, and this behavior is in good agreement with previous work on the effects of quantum wells, where thermal conductivities significantly decrease with well width due to spatial confinement of acoustic phonons.⁴³ In the C5G system, the anisotropy of thermal conductivity is still present ($\kappa_x / \kappa_y \sim 1/2$), although substantially weaker than HG cases. Damped atomic fluctuations in the clamped region produce a partially damped wave as shown schematically in Figure 3.6 (lower right) along the perpendicular direction to the pattern in partially functionalized C5G samples. Due to this damped wave propagation, thermal transport along the perpendicular direction is

suppressed by a factor of two compared to the parallel direction. Thus, in contrast to the case of HG, for C5G the suppressed thermal transport is due to a combination of scattering and clamping effects of the C5 pattern, and these effects can further suppress not only thermal conductivity perpendicular to the boundary, but parallel as well.

3.2.2.3. (C5+H)-Functionalized Graphene

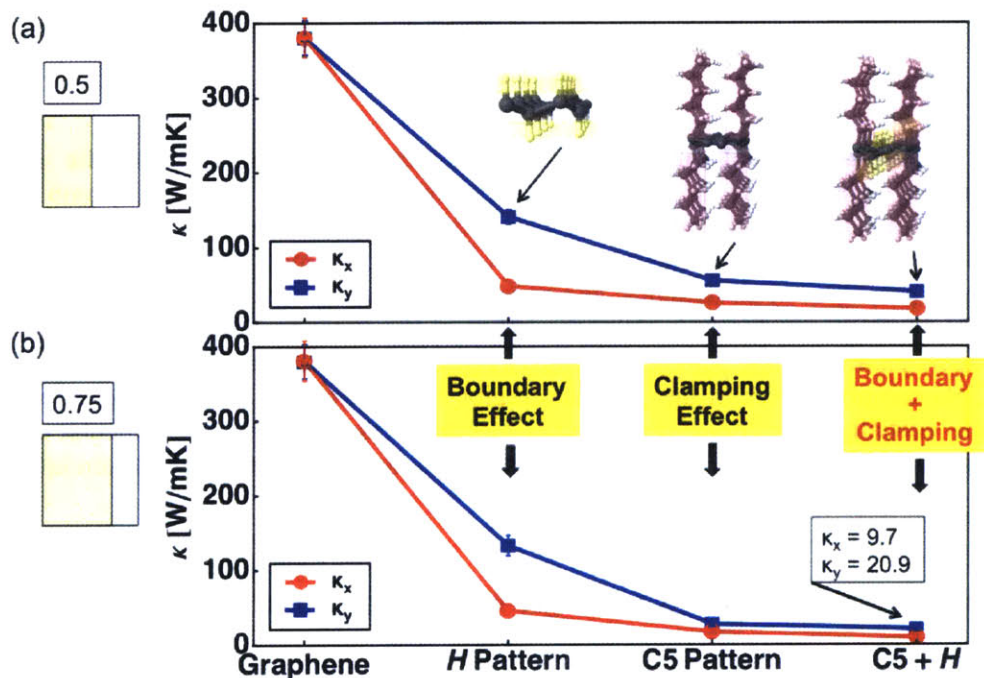


Figure 3.7 | Thermal conductivities of patterned graphene as a function of functional groups are shown for (a) 0.5 and (b) 0.75 pattern coverage. Each functional group introduces different thermal conductivity reduction effects as indicated.

By combining HG and C5G functionalization into the same sample, a further reduction in thermal conductivity can be achieved. In this case, all carbon atoms in the patterned region of graphene can have sp^3 bonding, and a well-defined boundary between graphene (sp^2) and graphane (sp^3) is formed. Combining both boundary and clamping effects in this manner is

found to reduce κ to 9.7 W/mK, which is 40 times smaller than that of pristine graphene within our calculations (see Figure 3.7).

3.3. Understanding Reduction Mechanisms in Functionalized Graphene

In order to analyze the properties of the main heat carriers in functionalized graphene and understand how they differ from those of pristine graphene, we carried out a series of lattice dynamics calculations. We compute the group velocities and lifetimes of each phonon mode in order to quantify their contributions to the thermal conductivity.

3.3.1. Pristine Graphene

In pristine graphene, our calculations show that there are five main heat carrying phonon modes (see Figure 3.8), each of whose contribution to κ is larger than 4% of the total thermal conductivity. As expected, the low-frequency phonon modes account for most of the thermal conductivity.

3.3.2. H-Functionalized Graphene

For the case of hydrogen functionalization, we examine a system with 50% pattern coverage. Our calculations show that due to the presence of a well-defined boundary, the lifetimes of phonon modes below 20 THz are greatly decreased with respect to those in pristine graphene, which makes a large contribution to the decrease of thermal conductivity in the direction both perpendicular and parallel to the pattern, as found in our MD simulations.

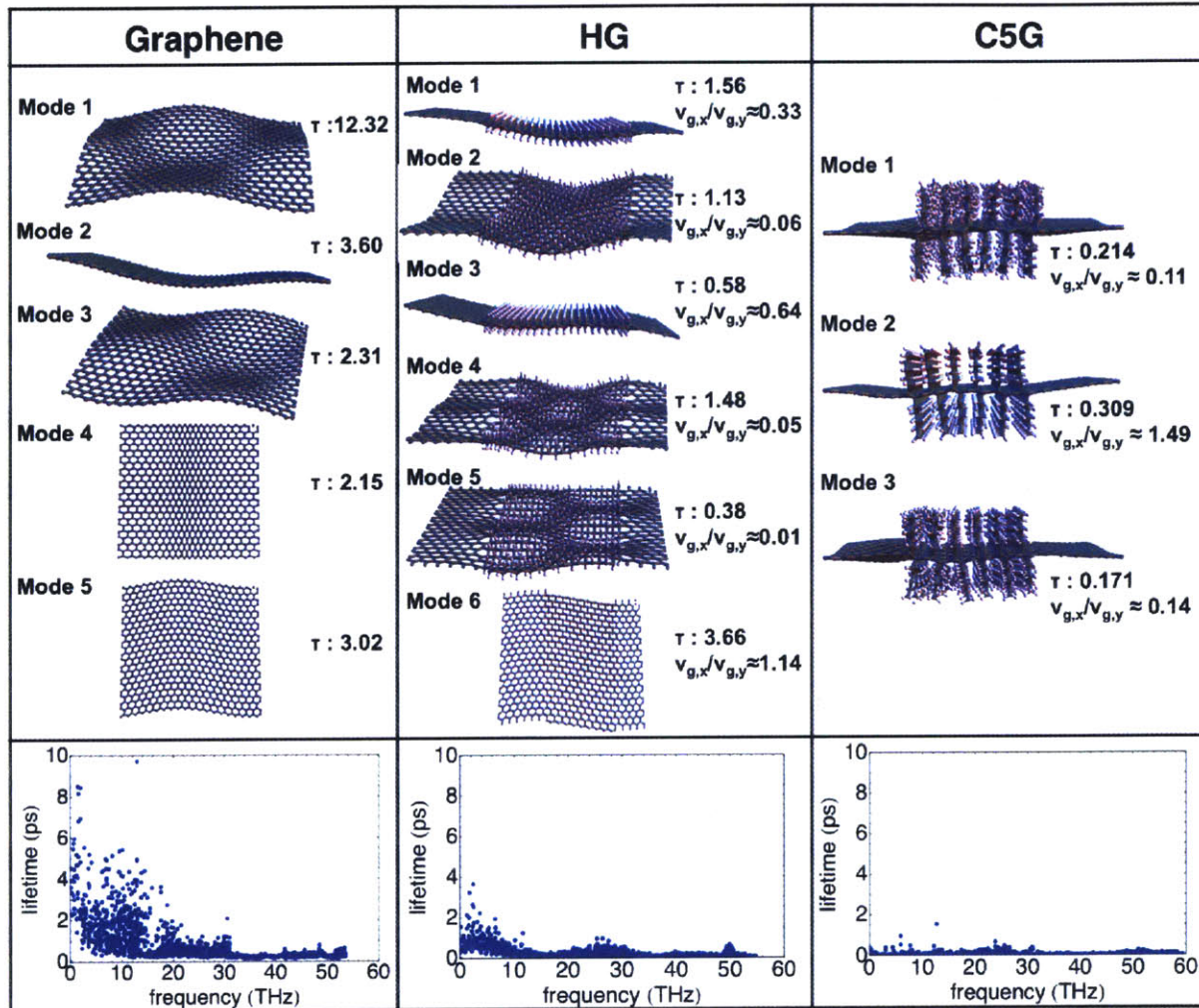


Figure 3.8 | Main heat carrying phonon modes, whose κ contribution is larger than 4% of total κ , for pristine graphene and HG and C5G samples with 50% coverage. Corresponding lifetimes and group velocity ratios for these particular modes are listed, and lifetimes for all frequencies in each sample are also shown (bottom graphs).

It is also observed that the group velocities (v_g) of the main heat carrying modes in HG samples are different in the two directions: v_g in the direction perpendicular to the pattern ($v_{g,x}$) is much lower than in the parallel direction ($v_{g,y}$). As mentioned, this is because of an acoustic mismatch at boundary, which leads to a modification of the phonon dispersion and group velocities. For instance, in phonon modes 2, 4 and 5, whose total contributions to κ_y are roughly 20 %, we find that $v_{g,x}$ is more than 20X smaller than $v_{g,y}$ resulting in a 400X smaller

κ_x than κ_y . The fact that these phonon modes cannot carry heat in the direction perpendicular to the pattern while carrying heat in the parallel direction is due to partial confinement in either domain. Note that the shape of these modes (see Figure 3.8) is nearly consistent with the previous expectation for partial confinement in HG samples (see Figure 3.6), where phonon modes in either domain exist separately. However, phonon modes 1, 3 and 6, which are consistent with waves with no confinement, contribute to heat conduction in both directions. From these lattice dynamics calculations, we find that about 20 % of phonon modes in κ_y in our HG sample are frozen out in the perpendicular direction due to partial phonon confinement, and the other 80 % contribute to perpendicular thermal transport in HG samples with reduced group velocities. This thermal transport phenomenon leads to the thermal conductivity difference in directions, consistent with the fact that κ_x/κ_y is roughly 1/3 in this HG sample.

3.3.3. C5-Functionalized Graphene

For the C5G case, our calculations show a further reduction of the phonon lifetimes, especially for the low frequency modes, which is consistent with the large decrease of both κ_x and κ_y . As discussed above, the large reduction in lifetime can be understood by scattering between sp^2 and sp^3 carbon induced from the particular kind of functionalization pattern of C5 chains on graphene.

In C5G samples, $v_{g,x}/v_{g,y}$ values can be larger than 1 (*e.g.*, mode 2) due to the spatial phonon confinement in un-patterned graphene regions, resulting in a strong modification of the phonon dispersion and reduction of group velocities in the parallel direction to the pattern.⁴³ Moreover, partially damped waves in C5G samples further reduce group velocities in the perpendicular direction, as can be seen from modes 1 and 3. Although all of the main heat

carrying phonon modes of the C5G sample contribute to heat conduction in both directions with different contributions, thermal conduction in the perpendicular direction is roughly 2X lower than in the parallel direction, consistent with the larger value of κ_x / κ_y , 0.469, than that of HG samples.

3.4. Outlook and Future Work

Chemical functionalization plays a significant role in the thermal transport of 2D materials since all atoms in the system can be functionalized, and phonon modes can be widely modified suggesting many possibilities for tuning thermal transport, in contrast to the case of 3D where only surface atoms can be functionalized leading to a minor influence on thermal transport. In this work, we performed molecular and lattice dynamics calculations to study the effect of chemical functionalization on thermal transport of graphene monolayers. Our simulations demonstrate that the presence of 2D periodic patterns on a graphene sheet suppresses thermal conductivity due to two main effects: 1) boundary effects induced from the sharp interface between sp^2 and sp^3 carbon domains and 2) clamping effects induced from both the additional mass as well as steric packing of hydrocarbon chains. Introducing boundaries in materials by nanostructuring has been widely used to reduce thermal conductivity.¹⁹⁻²¹ In the present work, we propose an approach for reducing the thermal conductivity in graphene based on steric hindrance, which could be applied to other materials, such as 1D carbon nanotubes and 2D boron nitride sheets. By combining steric hindrance with boundary scattering, we predict a reduction of the thermal conductivity by as much as a factor of 40 compared to pristine graphene. Our results suggest that chemical functionalization could broadly tailor thermal transport in low-dimensional system with different chemistries that change mass, charge and shape of functional groups, as

well as functionalized configuration. For example, using planar molecules such as benzene or azobenzene, which would induce more closely packed functionalization providing a stronger clamping effect, the thermal conductivity reduction could be even further enhanced. Further, the presence of a second layer of graphene together with chemical functionalization can have a similar effect; our calculations on C5+H samples with half-coverage show a reduction from 18 W/mK in the single-layer case to 11 W/mK for a bilayer. These results suggest the tunable thermal conductivity of functionalized graphene could lead to its use as an efficient thermoelectric material.^{24,44,45}

References

1. Geim, A. K., Novoselov, K. S. The rise of graphene. *Nat Mater* **6**, 183-191 (2007).
2. Charlier, J. C., Eklund, P. C., Zhu, J., Ferrari, A. C. Electron and phonon properties of graphene: Their relationship with carbon nanotubes. In: Jorio A, Dresselhaus G, Dresselhaus MS (eds). *Carbon Nanotubes*; , vol. 111. Springer: New York, 2008, pp 673-709.
3. Kageshima, H., Hibino, H., Nagase, M., Sekine, Y., Yamaguchi, H. Theoretical Study on Magnetoelectric and Thermoelectric Properties for Graphene Devices. *Japanese Journal of Applied Physics* **50**, (2011).
4. Sevincli, H., Cuniberti, G. Enhanced thermoelectric figure of merit in edge-disordered zigzag graphene nanoribbons. *Phys Rev B* **81**, 113401 (2010).
5. Bao, W. S., Liu, S. Y., Lei, X. L. Thermoelectric power in graphene. *Journal of Physics-Condensed Matter* **22**, 315502 (2010).
6. Dragoman, D., Dragoman, M. Giant thermoelectric effect in graphene. *Appl Phys Lett* **91**, 203116 (2007).
7. Hwang, E. H., Rossi, E., Das Sarma, S. Theory of thermopower in two-dimensional graphene. *Phys Rev B* **80**, 235415 (2009).
8. Seol, J. H., Jo, I., Moore, A. L., Lindsay, L., Aitken, Z. H., Pettes, M. T., *et al.* Two-dimensional phonon transport in supported graphene. *Science* **328**, 213-216 (2010).
9. Zuev, Y. M., Chang, W., Kim, P. Thermoelectric and magnetothermoelectric transport measurements of graphene. *Phys Rev Lett* **102**, 096807 (2009).
10. Wei, P., Bao, W. Z., Pu, Y., Lau, C. N., Shi, J. Anomalous Thermoelectric Transport of Dirac Particles in Graphene. *Phys Rev Lett* **102**, 166808 (2009).
11. Balandin, A. A., Ghosh, S., Bao, W. Z., Calizo, I., Teweldebrhan, D., Miao, F., *et al.* Superior thermal conductivity of single-layer graphene. *Nano Lett* **8**, 902-907 (2008).
12. Ghosh, S., Calizo, I., Teweldebrhan, D., Pokatilov, E. P., Nika, D. L., Balandin, A. A., *et al.* Extremely high thermal conductivity of graphene: Prospects for thermal management applications in nanoelectronic circuits. *Appl Phys Lett* **92**, 151911 (2008).
13. Nika, D. L., Pokatilov, E. P., Askerov, A. S., Balandin, A. A. Phonon thermal conduction in graphene: Role of Umklapp and edge roughness scattering. *Phys Rev B* **79**, 155413 (2009).
14. Uher, C. Skutterudites: Prospective novel thermoelectrics. *Semicond Semimetals* **69**, 139-253 (2001).
15. Nolas, G. S., Poon, J., Kanatzidis, M. Recent developments in bulk thermoelectric materials. *Mrs Bulletin* **31**, 199-205 (2006).
16. Zhang, H. J., Lee, G., Cho, K. Thermal transport in graphene and effects of vacancy defects. *Phys Rev B* **84**, 115460 (2011).
17. Jiang, J. W., Wang, B. S., Wang, J. S. First principle study of the thermal conductance in graphene nanoribbon with vacancy and substitutional silicon defects. *Appl Phys Lett* **98**, (2011).
18. Chen, S. S., Wu, Q. Z., Mishra, C., Kang, J. Y., Zhang, H. J., Cho, K. J., *et al.* Thermal conductivity of

- isotopically modified graphene. *Nat Mater* **11**, 203-207 (2012).
19. Li, D. Y., Wu, Y. Y., Kim, P., Shi, L., Yang, P. D., Majumdar, A. Thermal conductivity of individual silicon nanowires. *Appl Phys Lett* **83**, 2934-2936 (2003).
 20. Donadio, D., Galli, G. Atomistic Simulations of Heat Transport in Silicon Nanowires. *Phys Rev Lett* **102**, 195901 (2009).
 21. Lee, S. M., Cahill, D. G., Venkatasubramanian, R. Thermal conductivity of Si-Ge superlattices. *Appl Phys Lett* **70**, 2957-2959 (1997).
 22. Savin, A. V., Kivshar, Y. S., Hu, B. Suppression of thermal conductivity in graphene nanoribbons with rough edges. *Phys Rev B* **82**, 195422 (2010).
 23. Hu, J. N., Ruan, X. L., Chen, Y. P. Thermal Conductivity and Thermal Rectification in Graphene Nanoribbons: A Molecular Dynamics Study. *Nano Lett* **9**, 2730-2735 (2009).
 24. Nika, D. L., Balandin, A. A. Two-dimensional phonon transport in graphene. *Journal of Physics-Condensed Matter* **24**, (2012).
 25. Singh, A. K., Yakobson, B. I. Electronics and Magnetism of Patterned Graphene Nanoroads. *Nano Lett* **9**, 1540-1543 (2009).
 26. Boukhvalov, D. W., Katsnelson, M. I. Chemical functionalization of graphene. *Journal of Physics-Condensed Matter* **21**, 344205 (2009).
 27. Sessi, P., Guest, J. R., Bode, M., Guisinger, N. P. Patterning Graphene at the Nanometer Scale via Hydrogen Desorption. *Nano Lett* **9**, 4343-4347 (2009).
 28. Balog, R., Jorgensen, B., Nilsson, L., Andersen, M., Rienks, E., Bianchi, M., *et al.* Bandgap opening in graphene induced by patterned hydrogen adsorption. *Nat Mater* **9**, 315-319 (2010).
 29. Elias, D. C., Nair, R. R., Mohiuddin, T. M. G., Morozov, S. V., Blake, P., Halsall, M. P., *et al.* Control of Graphene's Properties by Reversible Hydrogenation: Evidence for Graphane. *Science* **323**, 610-613 (2009).
 30. Plimpton, S. Fast Parallel Algorithms for Short-Range Molecular-Dynamics. *J Comput Phys* **117**, 1-19 (1995).
 31. Brenner, D. W., Shenderova, O. A., Harrison, J. A., Stuart, S. J., Ni, B., Sinnott, S. B. A second-generation reactive empirical bond order (REBO) potential energy expression for hydrocarbons. *J Phys: Condens Matter* **14**, 783-802 (2002).
 32. Ong, Z. Y., Pop, E. Effect of substrate modes on thermal transport in supported graphene. *Phys Rev B* **84**, 075471 (2011).
 33. Zhang, H. J., Lee, G., Fonseca, A. F., Borders, T. L., Cho, K. Isotope Effect on the Thermal Conductivity of Graphene. *Journal of Nanomaterials* 537657 (2010).
 34. Chien, S. K., Yang, Y. T., Chen, C. K. Influence of hydrogen functionalization on thermal conductivity of graphene: Nonequilibrium molecular dynamics simulations. *Appl Phys Lett* **98**, 033107 (2011).
 35. Lindsay, L., Broido, D. A. Optimized Tersoff and Brenner empirical potential parameters for lattice dynamics and phonon thermal transport in carbon nanotubes and graphene. *Phys Rev B* **81**, 205441 (2010).
 36. Sofo, J. O., Chaudhari, A. S., Barber, G. D. Graphane: A two-dimensional hydrocarbon. *Phys Rev B* **75**, 153401 (2007).
 37. Torrent-Sucarrat, M., Liu, S. B., De Proft, F. Steric Effect: Partitioning in Atomic and Functional Group Contributions. *J Phys Chem A* **113**, 3698-3702 (2009).
 38. Pei, Q. X., Sha, Z. D., Zhang, Y. W. A theoretical analysis of the thermal conductivity of hydrogenated graphene. *Carbon* **49**, 4752-4759 (2011).
 39. Zhao, H., Freund, J. B. Phonon scattering at a rough interface between two fcc lattices. *J Appl Phys* **105**, (2009).
 40. Chen, G. Phonon wave heat conduction in thin films and superlattices. *J Heat Transfer* **121**, 945-953 (1999).
 41. Hyldgaard, P., Mahan, G. D. Phonon superlattice transport. *Phys Rev B* **56**, 10754-10757 (1997).
 42. Lindsay, L., Broido, D. A., Mingo, N. Flexural phonons and thermal transport in graphene. *Phys Rev B* **82**, 115427 (2010).
 43. Balandin, A., Wang, K. L. Effect of phonon confinement on the thermoelectric figure of merit of quantum wells. *J Appl Phys* **84**, 6149-6153 (1998).
 44. Balandin, A. A. Thermal properties of graphene and nanostructured carbon materials. *Nat Mater* **10**, 569-581 (2011).
 45. Balandin, A. A., Nika, D. L. Phononics in low-dimensional materials. *Materials Today* **15**, 266-275 (2012).

Chapter 4

High-Efficiency Thermoelectrics with Functionalized Graphene

4.1. Introduction to High-Efficiency Thermoelectrics with Functionalized Graphene

Recent work has shown that the most familiar 2D carbon material, namely graphene, exhibits remarkable electronic transport properties, with a record carrier mobility of $\sim 200,000 \text{ cm}^2 \text{ V}^{-1} \text{ s}^{-1}$ reported for a suspended single layer¹ as well as a moderate Seebeck coefficient (S) of $\sim 80 \text{ } \mu\text{V K}^{-1}$.^{2,3} Graphene is well known to possess an ambipolar nature, such that the sign of S can be controlled by changing the gate bias instead of doping.⁴ Experimentally measured values of the thermoelectric figure of merit (ZT) for pristine graphene at room temperature are in the range of $0.1 - 0.01$,^{2,3,5,6} roughly two orders of magnitude lower than the most efficient 3D thermoelectric materials such as Bi_2Te_3 alloys.⁷ Such low ZT values for graphene are to be expected due to its extremely high thermal conductivity (κ), on the order of $2000\text{--}5000 \text{ W m}^{-1}\text{K}^{-1}$.^{6,8,9}

In the last section, we explored mechanisms for reduction in the thermal conductivity of patterned graphene nano-roads. In this section, we examine the impact of such functionalization on the electronic contributions to the figure of merit, and consider the prospect of patterned graphene nano-roads¹⁰ as an efficient thermoelectric material. The patterning introduces quantum

confinement in pure (unfunctionalized) graphene by reducing its dimensionality from 2D to quasi-1D, with the periodic functionalization lines forming arrays of parallel graphene regions. Confinement in the material leads to an improvement in the power factor by increasing the density of states at the Fermi level, as demonstrated in recent studies¹¹⁻¹³ for low-dimensional thermoelectric materials.

4.2. Atomic Structure of Chemically Functionalized Graphene

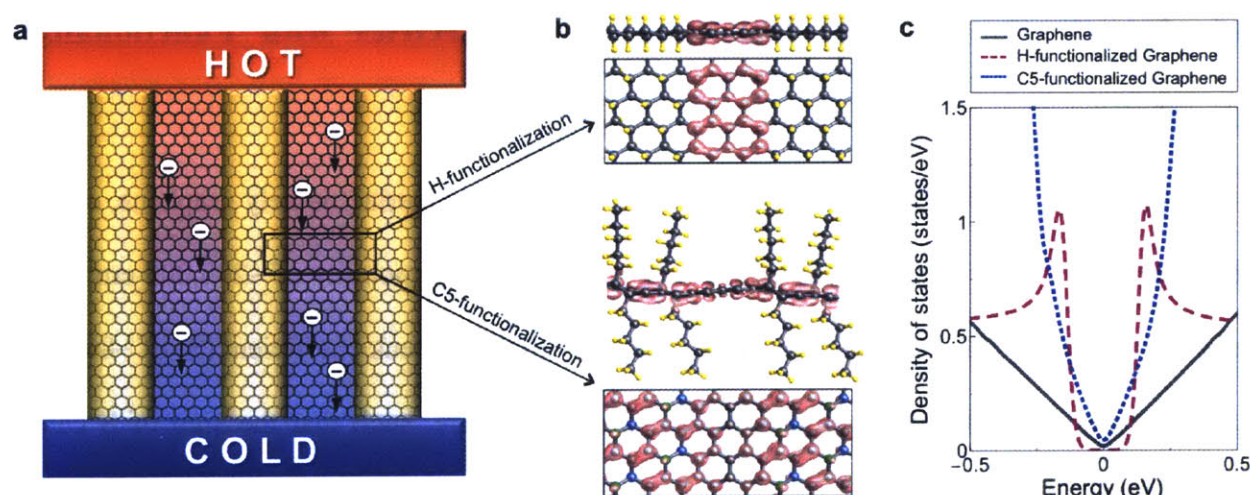


Figure 4.1 | 2D thermoelectric based on patterned graphene nano-roads with two different chemical functionalizations. (a) Schematic of 2D thermoelectric based on patterned graphene nano-roads with an armchair-type boundary. Yellow shaded area indicates the patterned region. (b) We consider H-functionalized graphene (HG) for 6 Å pattern width (top) and C5-functionalized graphene (C5G) (bottom). C and H atoms are represented by gray and yellow spheres, respectively. Pink contour plot represents charge density of the conduction band in each sample. Green and blue spheres indicate the C sites where C5 chains are attached on the up and down side of graphene, respectively. (c) Density of states (DOS) per unit cell of graphene, HG and C5G.

Figure 4.1a shows a schematic of a 2D thermoelectric device based on graphene nano-roads with armchair-type interfaces formed *via* partial functionalization. This type of superlattice is modeled with a repeated structure of pristine graphene (sp^2 network) and graphene with

functionalization ($sp^2 + sp^3$ network) within the same sheet, where the former exhibits semi-metallic behavior, and the latter shows insulating or semiconducting behavior depending on the functional groups. The electronic structure of functionalized graphene is strongly influenced by the functionalized configurations on the graphene sheet, determined by the shape of the functional groups. For example, H-functionalization generates full functionalization (perfect sp^3 network) showing insulating behavior, whereas hydrocarbon chains generate partial functionalization of the graphene sheet due to the steric repulsion between the chains, exhibiting a graphene-like electronic structure with a distorted cone-shaped band. In this work, we continue with the same two different functional groups as in the previous section on thermal transport, H and pentane C_5H_{12} , or C5, to investigate how chemical functionalization influences the thermoelectric properties of a patterned graphene superlattice.

4.3. Charge Carrier Transport in H-Functionalized Graphene

4.3.1. Electronic Structure

We employed first-principles calculations performed within the framework of density functional theory (DFT) as implemented in the plane-wave basis VASP code.¹⁴ The projected augmented wave pseudopotentials¹⁵ with the PW91¹⁶ generalized gradient approximation of Perdew and Wang is used for treatment of the exchange-correlation energy. Geometry optimizations are performed using the conjugate gradient scheme until force components on every atom are less than 0.01 eV \AA^{-1} . The fully relaxed structures are used to compute the electronic band structure.

We first compute the electronic structure of partially H-functionalized graphene (HG). In this section, the width (W) of the pattern in our simulations ranges from 6–23 \AA and can be

represented by the number of pure carbon dimers (N_C) along the pattern direction in the unit cell as shown in Figure 4.2a. In our previous thermal transport study, we defined the system size of HG sample with W_p and W_g values, where N_C does not matter, but rather only W_g matters. However, for electronic properties, it turns out there is a particular dependence on the specific count of carbon atoms in the width, and define the size of HG samples with N_C values. While graphene is a zero-gap semiconductor with a 2D cone-shaped linear energy dispersion, all HG samples show semiconducting behavior with a finite energy gap due to confinement effects of the graphene parts of the structure. As in the case of armchair graphene-based nanoribbons,¹⁷ the gap can be categorized into three different families depending on N_C : $E_g(N_C = 3p+2) \ll E_g(N_C = 3p) < E_g(N_C = 3p+1)$, where p is an integer. This hierarchy is in good agreement with previous work on the energy gaps of hydrogenated graphene superlattices^{10,18} and it is also found that E_g decreases with N_C values within each family due to decreasing confinement effects. All HG samples show a flattened energy dispersion across the pattern direction, whereas energy bands along the pattern direction ($\Gamma \rightarrow Y$) retain the dispersive nature of pristine graphene, implying quasi-1D transport in such graphene superlattices. The reduction of the charge transport dimension in all HG samples introduces a peak in the DOS near the band edge, which would be expected to enhance S according to Mahan-Sofo theory.¹⁹

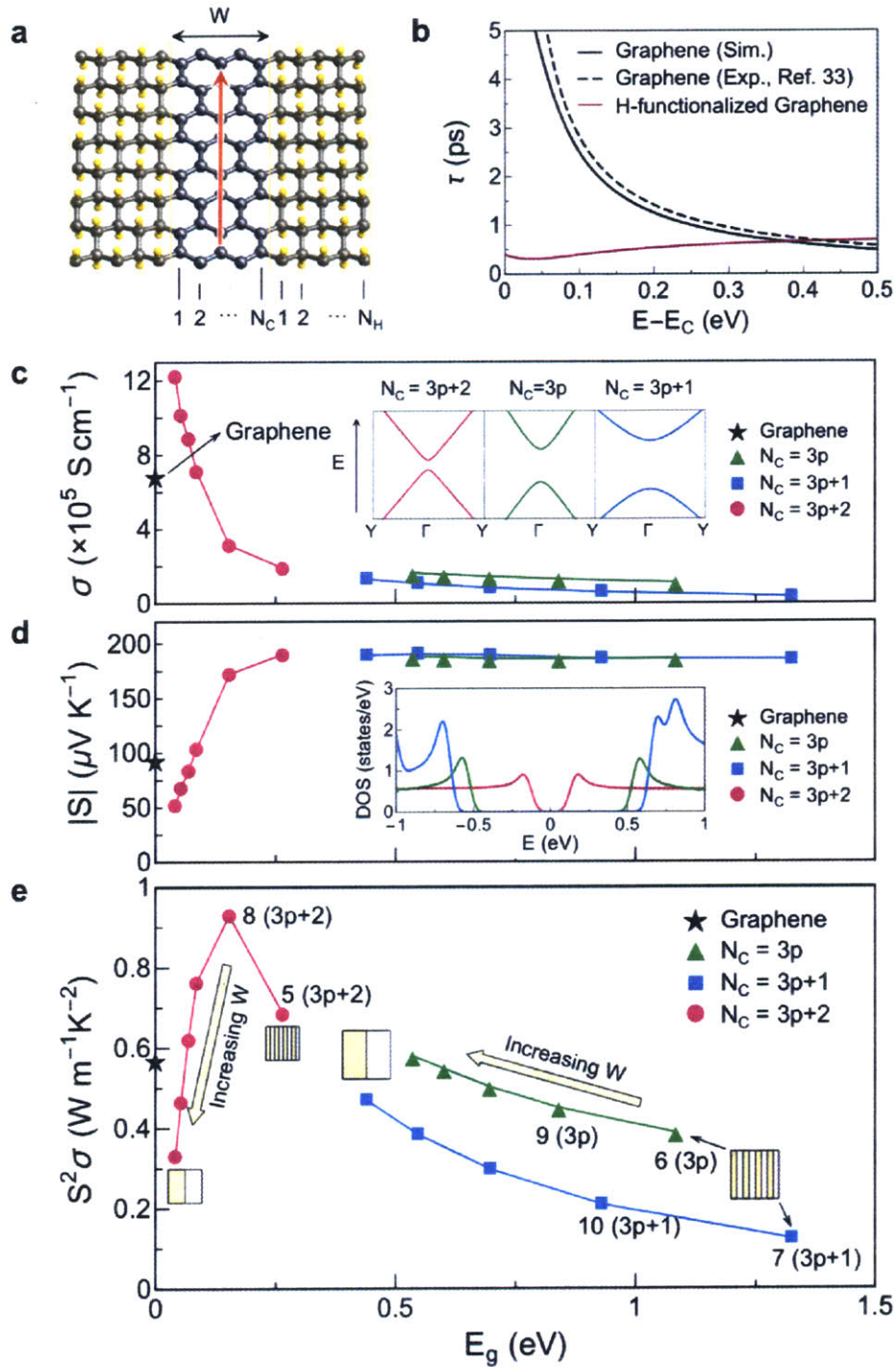


Figure 4.2 | Thermoelectric properties of H-functionalized patterned graphene nano-roads. (a) Structure of H-functionalized patterned graphene nano-roads along with structural variables. The red arrow represents the direction of transport considered in our work. (b) Relaxation time for graphene and HG as a function of the carrier energy. (c) Electrical conductivities of HG samples as a function of band gap (E_g). Inset represents computed energy dispersion of three different HG samples for $N_C = 3p+2$ (pink), $N_C = 3p$ (green) and $N_C = 3p+1$ (blue), respectively. (d) Seebeck coefficient of HG samples. Inset represents computed DOS per unit cell. (e) Power factors of HG samples at 300 K.

4.3.2. Relaxation Time

The relaxation time (τ) is a complex function of the electron energy, temperature, and atomic structure. In this respect, as we discussed in section 2.3.4, using a τ value obtained from pristine graphene is not a reasonable approximation for use in patterned graphene nano-roads, where chemical modification in those samples plays an important role in opening the energy gap, which indirectly relates to the relaxation time. Since the goal of our work is to determine the quantitative effect of functionalization on charge transport, we calculate the relaxation time of functionalized graphene samples with Boltzmann transport theory for a reliable quantitative approximation.

In this work, since we focus on the thermoelectric properties of a freestanding graphene monolayer, we ignore effects from charged impurities from the substrate or any organic residues on the graphene sheet, and only consider the acoustic phonon scattering. The relaxation time can be expressed with Eq. 2.34. This equation highlights the proportionality of the scattering rate to the density of states of the 2D graphene sheet.

The relaxation time of HG samples is calculated using Eq. 2.34 with density of states from first-principle calculations. Here, the D_{ac} value of pristine graphene (16 eV)²⁰ is used for the HG cases, which is a reasonable approximation since charge carriers are confined within the 1D pristine graphene regions as shown in Figure 4.1b. Figure 4.2b shows our calculated τ for pristine graphene and HG sample ($N_C = 6$) as a function of the carrier energy. For pristine graphene τ decreases with carrier energy, in good agreement with experiments that showed the room-temperature intrinsic resistivity of graphene $\sim 30 \text{ } \Omega$ is limited only by intrinsic LA phonon scattering.²¹ The scattering becomes more severe in HG samples compared with graphene, particularly near the band edge. We also find that calculated τ values in HG samples

are proportional to the width of the pattern (see Figure 4.3), resulting in stronger scattering for narrower patterns, similar to the ribbon width dependence in GNR.²²

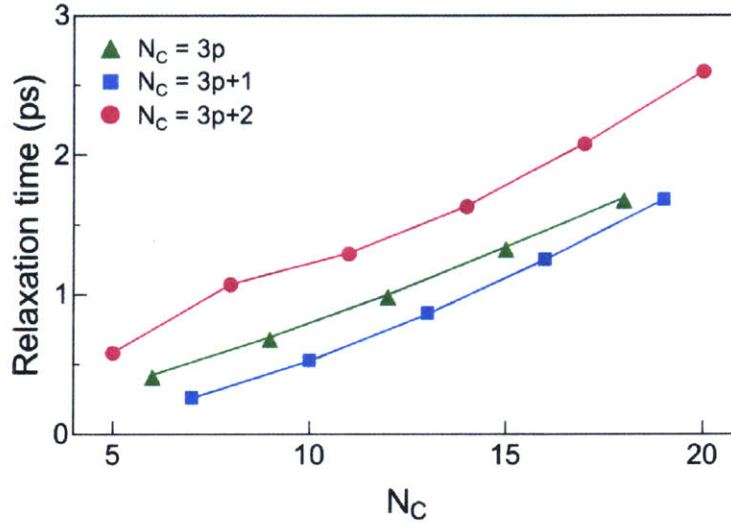


Figure 4.3 | Calculated relaxation time of three different HG samples at n_{peak} and as a function of N_C for $N_C = 3p+2$ (pink), $N_C = 3p$ (green) and $N_C = 3p+1$ (blue), respectively.

4.3.3. Transport Coefficients

Room-temperature transport calculations of patterned graphene nano-roads are calculated by semi-classical Boltzmann transport approach within the constant relaxation time approximation, as implemented in the BOLTZTRAP code.²³ Here, we are interested in transport along the pattern direction (y). The converged values of σ and S are obtained using a dense k -point mesh of 121 points along the y direction. All simulations are carried out at 300 K and a carrier concentration range of 10^{11} – 10^{13} cm^{-2} .

The electrical conductivity (σ) and Seebeck coefficient (S), are calculated as a function of carrier concentration (n_i), where σ increases with n_i while S decreases, resulting in a maximum power factor ($S^2\sigma$) at carrier concentrations (n_{peak}) between 10^{12} – 10^{13} cm^{-2} , corresponding to

the band edge (see Figure 4.4). Our calculated σ and S values at n_{peak} as a function of band gap (E_g) are presented in Figures 4.2c and 4.2d for the range of HG samples considered. Here, we are only interested in thermoelectric properties along the pattern direction since values in the direction perpendicular to the pattern are negligible due to the band flattening.

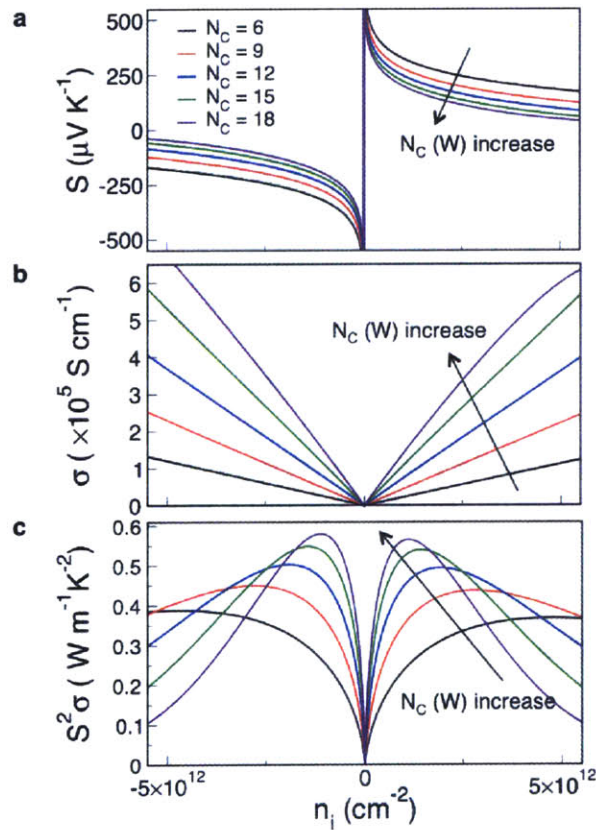


Figure 4.4 | Thermoelectric properties of H-functionalized Graphene in the 3p family. Seebeck coefficient (a), electrical conductivity (b), and power factor (c) as a function of carrier concentration (n_i) for different N_C values.

As can be seen in Figure 4.2c, σ decreases with E_g implying that wider H-patterns exhibit higher σ because τ increases. Clearly, the presence of the H-pattern reduces σ compared to pristine graphene, especially for the 3p and 3p+1 families, due to both the reduced τ as well as reduced group velocities. Among the three different families, samples in the 3p+1 family show

the lowest σ , which can be explained by the lowest slope in the band dispersion as shown in the inset of Figure 4.2c. It is interesting to observe that 3p+2 family samples with $E_g < 0.1$ eV show higher σ than graphene because the maximum power factor arises at a higher carrier concentration, where more carriers contribute to the transport. On the other hand, most of the HG samples show larger S than pristine graphene. This can be explained by a peak in the DOS near the band edge, induced from the reduction of the charge transport dimension as shown in the inset of Figure 4.2d. This sharp increase in the DOS enhances S by a factor of 2 for the 3p and 3p+1 family samples. Since S is proportional to the magnitude of the DOS peak, S is expected to increase as the pattern width decreases in going from the bulk to the nano-structured case. This is indeed what we observe for the 3p+2 family. However, for the 3p and 3p+1 family, the maximum power factor occurs at higher carrier concentration for narrower pattern samples, and the decrease of S due to higher carrier concentration is large enough to compensate the increase of S due to stronger confinement effects as the pattern width decreases, resulting in nearly constant S values among samples.

These two conflicting thermoelectric properties produce a strong dependence between the power factor and band gap (Figure 4.2e), with a maximum value of $S^2\sigma$ at $E_g \sim 0.15$ eV for the HG sample with the $N_C = 8$ pattern ($W = 10$ Å). For $E_g > 0.15$ eV, $S^2\sigma$ decreases as E_g increases, indicating that the wider H-pattern generates superior charge transport in these graphene superlattices. The reduction in $S^2\sigma$ in this regime is mainly due to more severe scattering for narrower H-patterns. On the other hand, $S^2\sigma$ decreases as E_g decreases for $E_g < 0.15$ eV, and this behavior can be explained by the S^2 term in the power factor, which is significantly reduced with H-pattern width, due to weaker confinement effects. Thus, the HG sample with the $N_C = 8$ pattern exhibits the best performance for TE applications with $S^2\sigma \sim$

0.93 $\text{W m}^{-1}\text{K}^{-2}$, which is about 1.6 times larger than pristine graphene. We note that this large enhancement in power factor arises from considerably enhanced S as well as a comparatively small reduction in σ in spite of strong scattering due to the H-pattern.

4.4. Charge Carrier Transport in C5-Functionalized Graphene

4.4.1. Electronic Structure

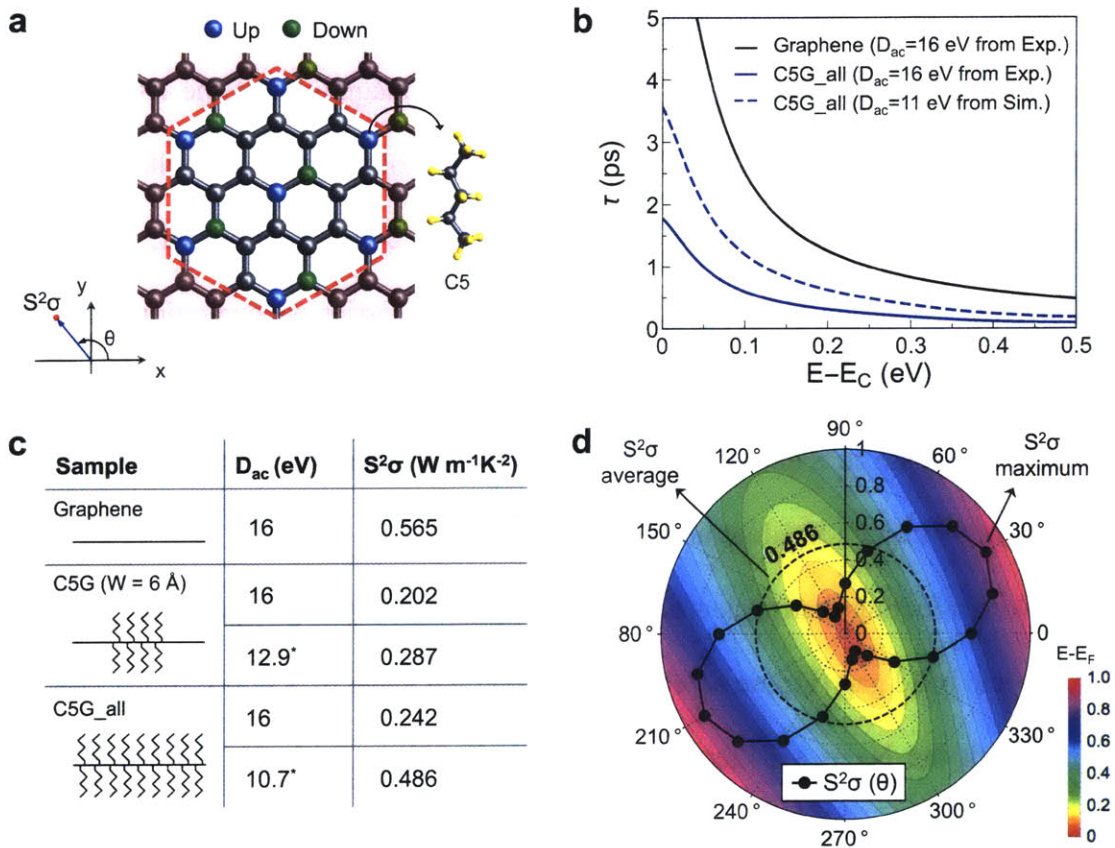


Figure 4.5 | Thermoelectric properties of C5-functionalized graphene. (a) Configuration of C5-functionalized graphene (C5G) with the structure of C5 (pentane: C_5H_{12}). C5 chains are arranged in a two-dimensional hexagonal close-packed lattice on the graphene sheet. (b) Relaxation time for C5G as a function of the carrier energy. C5G_all represents C5G sample with full coverage. (c) Deformation potential constant (D_{ac}) and corresponding power factor of C5G samples, where * represents calculated D_{ac} values for C5G samples. (d) Power factor of fully functionalized C5G as a function of spatial direction. The black dashed line indicates the average value of the power factor. The background represents the energy band contour of constant energy, showing a distorted cone-shape dispersion.

We next consider the case of functionalizing graphene with pentane chains (C5), which was shown in the previous section to further reduce κ in graphene superlattices beyond simple hydrogen functionalization due to a clamping effect imposed by the steric hindrance between chains. In contrast to the one-dimensional dispersion of HG cases, C5-functionalized graphene (C5G) exhibits a 2D distorted cone-shape band, resulting in an anisotropic σ (Figure 4.5d). This difference is caused by the fact that C5 patterns cannot generate confinement effects in graphene due to their inability to pack them closely enough to functionalize every carbon atom. As a result, the DOS of a C5G sample is similar to that of pristine graphene (Figure 4.1c), showing no peak at the band edge, and our computed S values are similar in all directions to that of pristine graphene.

4.4.2. Relaxation Time

It should be noted that in contrast to HG samples, charge carriers in C5G samples are not confined in an un-functionalized region but rather delocalized over the entire 2D graphene sheet as shown in Figure 4.1b. Accordingly, we need to determine an accurate value of D_{ac} for C5G samples, which considers the electron-phonon coupling for this specific functionalization. To this end, we compute D_{ac} using Bardeen and Shockley's theory,²⁴ where the deformation potential constant $D_{ac} = \Delta E / (\Delta l_x / l_x)$ is determined by shifts in the band energy (ΔE) under the lattice dilations ($\Delta l_x / l_x$). We note that it is difficult to obtain absolute values of D_{ac} using this approach because the absolute position of an energy level with respect to vacuum is ill-defined. However, the relative change D_{ac} arising from a C5-functionalized graphene sheet is sufficient to understand the effect of functionalization on charge transport. Reduction in D_{ac} gives rise to an increase in τ for the C5G samples as shown in Figure 4.5b.

The calculated D_{ac} and corresponding power factors are shown in Figure 4.5c. Reduction in D_{ac} gives rise to an increase in τ for the C5G samples, which is inversely proportional to the square of D_{ac} , as shown in Figure 4.5b. It is interesting to note that C5-functionalization leads to the suppression of electron-phonon coupling in the graphene sheet, implying diminished charge scattering.

4.4.3. Transport Coefficients

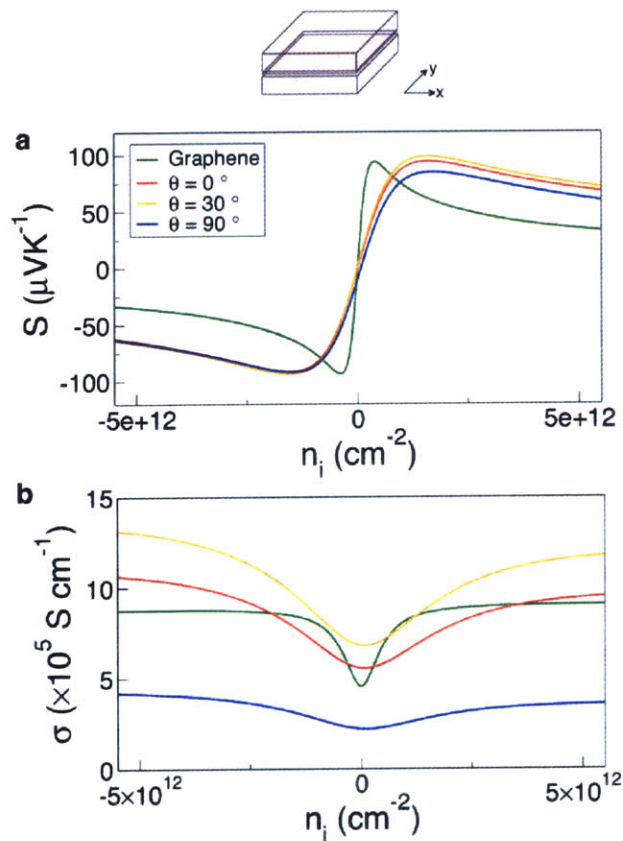


Figure 4.6 | Calculated Seebeck coefficients (a) and electrical conductivities (b) of fully functionalized C5G as a function of carrier concentration. Thermoelectric properties of pristine graphene are also shown for comparison. Due to the special functionalization configuration in C5G samples, we found anisotropic behaviour in electrical conductivities, where Seebeck coefficients exhibit no angular dependence.

In order to investigate the anisotropic behavior in the C5G sample, which arises from a special functionalization configuration, we compute thermoelectric coefficients in all directions, where directions are defined as θ , the angle above the positive x-axis (see Figure 4.5a). As expected, σ is highly anisotropic; however, S values are similar in all directions to that of pristine graphene as shown in Figure 4.6a and b.

Among the several C5G samples we considered with different pattern widths, the case of fully C5-functionalized graphene (*i.e.*, width=0, so no “nano-roads”) exhibits the largest $S^2\sigma$, with an average value close to the value of pristine graphene ($0.486 \text{ W m}^{-1}\text{K}^{-2}$). The peak in $S^2\sigma \sim 0.88 \text{ W m}^{-1}\text{K}^{-2}$ arises at $\theta = 30^\circ$, where the group velocity along this direction is largest due to the distorted band dispersion (Figure 4.5d). The values of $S^2\sigma$ for C5G samples are close to the value of graphene, showing good potential for TE applications when combined with the significantly reduced κ for this type of functionalization.²⁵

4.5. Charge Carrier Transport in (C5+H)-Functionalized Graphene

H-functionalization gives rise to confinement of the graphene region, where confined charge carriers induce an enhanced power factor, while the confined phonon modes in this case have little effect on thermal transport along the pattern direction, resulting in $3\times$ lower thermal conductivity than that of pristine graphene.²⁵ In contrast, C5-functionalization greatly suppresses κ in graphene superlattices from the steric repulsion of the C5 chains,²⁵ although as shown above no power factor improvement is observed for this case. Thus, each functionalization type alone would not be sufficient to make high efficiency graphene-based TE materials. However,

combining *both* functionalizations into the same sample could achieve the best of both worlds: namely, controllable charge transport with H-functionalization and tunable thermal transport with C5-functionalization. In this combined case, a well-defined boundary is formed between the sp^2 graphene and sp^3 domains, giving rise to the same types of electronic confinement effects as in the HG cases, and therefore the same energy dispersions, resulting in significant enhancements in $S^2\sigma$. We can also achieve further suppression of κ compared with either the HG or C5G samples due to a combination of boundary scattering and clamping effects.

4.6. Charge Carrier Transport in Pristine Graphene

Graphene exhibits a moderate Seebeck coefficient (S) of $\sim 80 \mu\text{V K}^{-1}$.^{2,3} Electrical conductivity (σ) of graphene ranges from 10^5 to 10^6 S cm^{-1} depending on sample quality. Here, 10^6 S cm^{-1} is obtained from the room-temperature intrinsic resistivity ($\sim 30 \Omega$), where the charge transport of graphene is limited only by the intrinsic LA phonon scattering.^{1,21} It also shows extremely high thermal conductivity (κ), on the order of $2000\text{--}5000 \text{ W m}^{-1}\text{K}^{-1}$.^{6,8,9} Combining these experimental studies, we can compute the thermoelectric figure of merit (ZT) for pristine graphene at room temperature, which is in the range of $0.1\text{--}0.01$.^{2,3,5,6}

Our calculated thermoelectric properties of pristine graphene as a function of carrier concentration (n_i) are shown in Figure 4.7. The maximum value of power factor ~ 0.565 for pristine graphene at room temperature is obtained. These calculated values are in the same range with experimental measurements of intrinsic thermoelectric properties for a graphene monolayer (without extrinsic sources of scattering). We note that direct comparison between our results and experiments is difficult since TE properties are highly dependent on carrier concentration and sample condition.

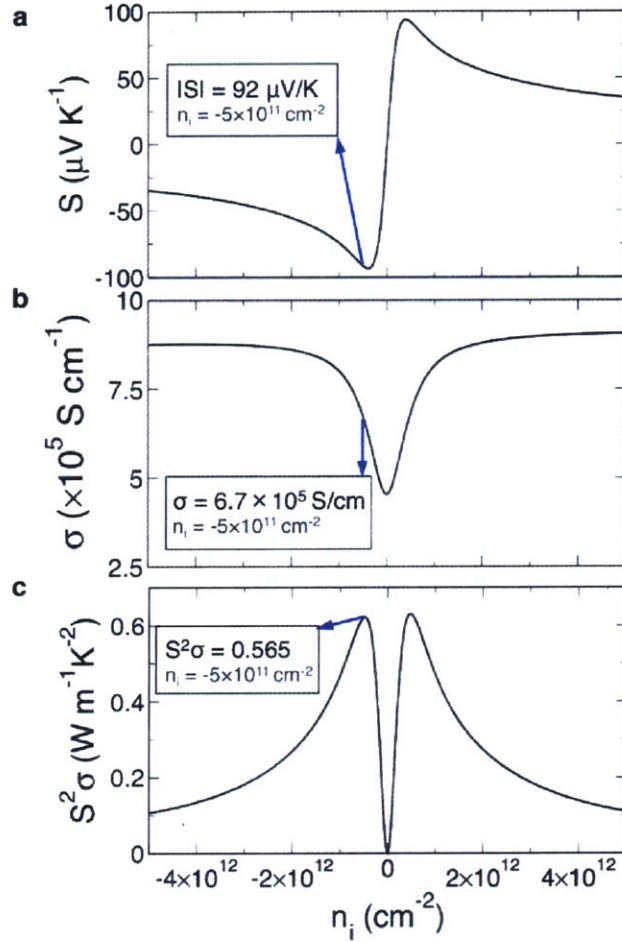


Figure 4.7 | Thermoelectric properties of pristine graphene as a function of carrier concentration (n_i). (a) Seebeck coefficient. (b) electrical conductivity, and (c) power factor.

4.7. Prediction of overall ZT values

The MD simulations employed in the previous section to compute the lattice thermal conductivity describe well the scattering effects of functionalization on thermal transport in graphene, especially for short-wavelength phonons. However, as discussed earlier in this thesis, given the current limits of system size and timescales, our MD simulations do not capture the contributions of long-wavelength phonons, which are important for thermal transport in graphene, resulting in lower κ values in our simulations by an order of magnitude than measured values. In order to quantitatively predict ZT, we modify our computed κ values by adding the long-

wavelength phonon contributions from the Klemens model,^{26,27} allowing one to obtain κ values for larger graphene samples.

4.7.1. Klemens Model

We modify our computed κ values by adding the long-wavelength phonon contributions from the Klemens model ($\kappa_{Klemens}$),^{26,27} allowing one to obtain κ values for larger graphene samples.

$$\kappa_{Klemens} = \frac{1}{2} \int_{f_b}^{f_c} C(f) \nu l(f) df \quad (4.1)$$

where C is the specific heat per unit volume, ν is the group velocity, l is the phonon mean free path, f_b is the lowest cutoff frequency, and f_c is the minimum frequency mode in the MD simulation.

As we mentioned in chapter 3, chemical functionalization of graphene introduces several different thermal conductivity (κ) reduction mechanisms, and these different κ reduction mechanisms have different influences on each phonon mode depending on its wavelength (frequency). For example, long wavelength phonons have less chance to be randomly scattered due to the boundary, while short wavelength phonons strongly scattered (Ziman's theory).²⁸ On the other hand, phonon confinement effects can strongly suppress long wavelength phonons due to the modified dispersion with lower group velocities.²⁹ Also, scattering between sp^2 and sp^3 carbon suppresses almost the whole frequency range of phonon modes. Thus, phonon modes of the entire range of frequencies can be suppressed due to a combination of several different reduction mechanisms, verified by greatly decreased lifetimes with respect to those in pristine graphene, especially below 20 THz, when graphene is functionalized.²⁵

For functionalized graphene samples, the long-wavelength phonon suppression by chemical functionalization is taken into account as:

$$\kappa_{Correct} = \frac{\kappa_{MD,F}}{\kappa_{MD,G}} \times \kappa_{Klemens} \quad (4.2)$$

where $\kappa_{MD,F}/\kappa_{MD,G}$ is the reduction of κ in functionalized graphene samples. From our previous works on thermal transport in functionalized graphene (in Chapter 3), we found that for functionalized graphene samples, κ along the pattern direction is mainly reduced due to suppressed lifetimes of each phonon modes, implying that long-wavelength phonons (*i.e.*, $\kappa_{Klemens}$) could also be suppressed by functionalization in the same manner. Accordingly, multiplying κ by this reduction term is quite reasonable to consider the influence of functionalization on long-wavelength phonon modes. Thus, the total thermal conductivity is defined as:

$$\kappa_{Total} = \kappa_{MD} + \kappa_{Correct} \quad (4.3)$$

We calculate κ_{MD} (parallel to the pattern boundary) for patterned graphene nano-roads, which are functionalized with H, C5, and C5+H patterns, as a function of pattern width as shown in Figure 4.8.

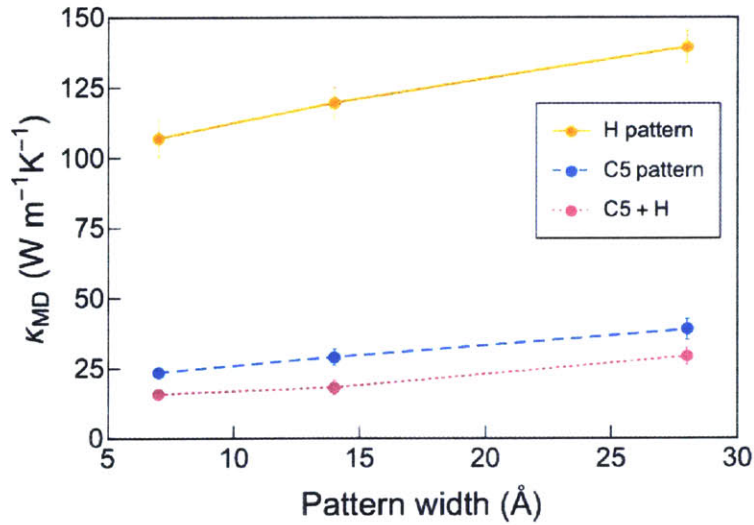


Figure 4.8 | Thermal conductivities of functionalized graphene with H pattern (solid line), C5 pattern (dashed line) and C5+H pattern (dotted line) parallel to the pattern as a function of pattern width.

At 300 K, we obtained a corrected $\kappa \sim 1810 \pm 23 \text{ W m}^{-1}\text{K}^{-1}$ for pristine graphene, combining the MD calculation term $\kappa_{MD} \sim 380 \pm 23 \text{ W m}^{-1}\text{K}^{-1}$ with the Klemens' correction²⁶ term $\kappa_{Klemens} \sim 1430 \text{ W m}^{-1}\text{K}^{-1}$ (see Figure 4.9)

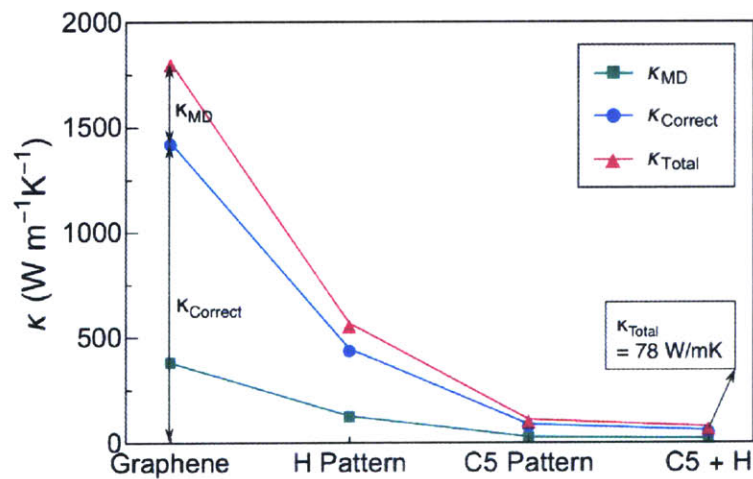


Figure 4.9 | Calculated thermal conductivities of patterned graphene as a function of functional groups are shown for $N_C = 8$ pattern width at 300 K, where $\kappa_{Total} = \kappa_{MD} + \kappa_{Correct}$.

4.7.2. ZT values in Functionalized Graphene

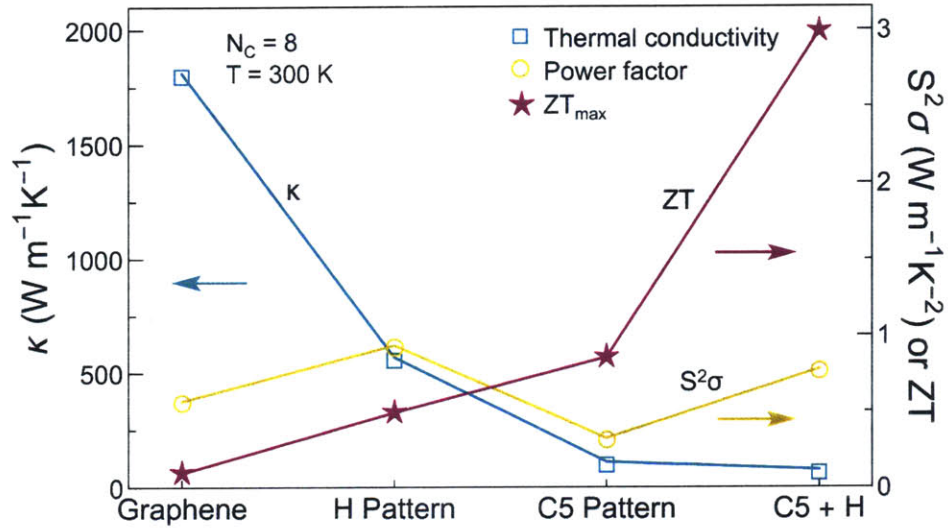


Figure 4.10 | Thermoelectric properties of patterned graphene nano-roads with different functional groups. Calculated thermal conductivity (green), power factor (orange) and ZT (red) of patterned graphene as a function of functional groups are shown for $N_C = 8$ pattern width, which exhibits the most enhanced charge transport. These are computed values along the pattern direction.

Using the correction for κ with Klemens model, we show our calculated thermoelectric properties of patterned graphene nano-roads as a function of functional groups in Figure 4.10 for the $N_C = 8$ pattern width. We predict a maximum value of $ZT \sim 0.09$ for pristine graphene at room temperature, in good agreement with experimental measurements of intrinsic thermoelectric properties for graphene monolayer without any extrinsic scattering sources.²¹ By combining the κ reduction and $S^2\sigma$ enhancements in each sample, we obtain significantly increased ZT values for all functionalized graphene samples compared to the pristine graphene case. Among these cases, a factor of ~ 30 enhancement in ZT can be achieved in the C5+H sample, with corresponding ZT values as large as 3 at room temperature. This large enhancement in ZT is due to a combination of a large reduction in κ and relatively small

enhancement in $S^2\sigma$ by 40 % from pristine graphene. Interestingly, the fully C5-functionalized graphene case also yields a figure of merit well above 2 at room temperature, even without periodic patterning on the graphene sheet, suggesting that chemical functionalization by itself offers further opportunities for graphene to become fascinating TE material without complex nano-patterning. The results suggest that chemical functionalization could be an important route to designing high-efficiency graphene-based TE materials, by allowing for independent control of charge transport and thermal transport.

4.8. Outlook and Future Work

In this work, we investigated the thermoelectric properties of patterned graphene nano-roads functionalized with H and C5 chains using both classical and quantum mechanical calculations. Periodically patterned sp^3 -hybridized carbon regions on graphene were shown to introduce DOS peaks at the band edge, which lead to substantially enhanced S and $S^2\sigma$ compared to that of pristine graphene at carrier concentrations corresponding to the band edge. These results also demonstrate that the thermal transport in such materials can be tuned by functional groups separately from the power factor, which simply depends on the pattern width. We note that unlike the case of standard, 3-dimensional TE materials, for the 2D cases considered here it is not difficult to achieve reduced κ and enhanced $S^2\sigma$ *simultaneously*, resulting in broad tunability of thermoelectric properties for this class of materials. Finally, although fabrication of functionalized graphene with 100 % H coverage or regular C5 chain ordering may be challenging, we note that incomplete H-functionalization in the patterned region has a negligible influence on ZT values of HG and (C5+H)-G samples since charge transport in these samples is mainly determined by the condition of the pristine graphene region. Furthermore, our

calculations of a fully functionalized C5G sample with random (as opposed to regular) C5 chain ordering still shows high ZT values at room temperature, as the decrease in thermal conductivity roughly tracks the decrease in the power factor, indicating that perfectly controlled ordering is not crucial for the potential use of functionalized graphene in TE applications.

References

1. Bolotin, K. I., Sikes, K. J., Jiang, Z., Klima, M., Fudenberg, G., Hone, J., *et al.* Ultrahigh electron mobility in suspended graphene. *Solid State Commun* **146**, 351-355 (2008).
2. Seol, J. H., Jo, I., Moore, A. L., Lindsay, L., Aitken, Z. H., Pettes, M. T., *et al.* Two-dimensional phonon transport in supported graphene. *Science* **328**, 213-216 (2010).
3. Zuev, Y. M., Chang, W., Kim, P. Thermoelectric and magnetothermoelectric transport measurements of graphene. *Phys Rev Lett* **102**, 096807 (2009).
4. Geim, A. K., Novoselov, K. S. The rise of graphene. *Nat Mater* **6**, 183-191 (2007).
5. Bolotin, K. I., Sikes, K. J., Hone, J., Stormer, H. L., Kim, P. Temperature-dependent transport in suspended graphene. *Phys Rev Lett* **101**, 096802 (2008).
6. Balandin, A. A. Thermal properties of graphene and nanostructured carbon materials. *Nat Mater* **10**, 569-581 (2011).
7. Poudel, B., Hao, Q., Ma, Y., Lan, Y. C., Minnich, A., Yu, B., *et al.* High-thermoelectric performance of nanostructured bismuth antimony telluride bulk alloys. *Science* **320**, 634-638 (2008).
8. Balandin, A. A., Ghosh, S., Bao, W. Z., Calizo, I., Teweldebrhan, D., Miao, F., *et al.* Superior thermal conductivity of single-layer graphene. *Nano Lett* **8**, 902-907 (2008).
9. Vincent, E. D., Ashkan Behnam, Hiram J. Conley, Kirill I. Bolotin, Pop, a. E. High-field electrical and thermal transport in suspended graphene. *Nano Lett* **13**, 4581-4586 (2013).
10. Singh, A. K., Yakobson, B. I. Electronics and magnetism of patterned graphene nanoroads. *Nano Lett* **9**, 1540-1543 (2009).
11. Lee, J. H., Galli, G. A., Grossman, J. C. Nanoporous Si as an Efficient Thermoelectric Material. *Nano Lett* **8**, 3750-3754 (2008).
12. Venkatasubramanian, R., Siivola, E., Colpitts, T., O'Quinn, B. Thin-film thermoelectric devices with high room-temperature figures of merit. *Nature* **413**, 597-602 (2001).
13. Dresselhaus, M. S., Chen, G., Tang, M. Y., Yang, R. G., Lee, H., Wang, D. Z., *et al.* New directions for low-dimensional thermoelectric materials. *Adv Mater* **19**, 1043-1053 (2007).
14. Kresse, G., Furthmuller, J. Efficient iterative schemes for ab initio total-energy calculations using a plane-wave basis set. *Phys Rev B* **54**, 11169-11186 (1996).
15. Kresse, G., Joubert, D. From ultrasoft pseudopotentials to the projector augmented-wave method. *Phys Rev B* **59**, 1758-1775 (1999).
16. Perdew, J. P., Wang, Y. Accurate and simple analytic representation of the electron-gas correlation-energy. *Phys Rev B* **45**, 13244-13249 (1992).
17. Son, Y. W., Cohen, M. L., Louie, S. G. Energy gaps in graphene nanoribbons. *Phys Rev Lett* **97**, 216803 (2006).
18. Lee, J. H., Grossman, J. C. Energy gap of Kronig-Penney-type hydrogenated graphene superlattices. *Phys Rev B* **84**, 113413 (2011).
19. Mahan, G. D., Sofo, J. O. The best thermoelectric. *Proc Natl Acad Sci USA* **93**, 7436-7439 (1996).
20. Pennington, G., Goldsman, N., Akturk, A., Wickenden, A. E. Deformation potential carrier-phonon scattering in semiconducting carbon nanotube transistors. *Appl Phys Lett* **90**, (2007).
21. Chen, J. H., Jang, C., Xiao, S. D., Ishigami, M., Fuhrer, M. S. Intrinsic and extrinsic performance limits of graphene devices on SiO₂. *Nat Nanotech* **3**, 206-209 (2008).

22. Fang, T., Konar, A., Xing, H., Jena, D. Mobility in semiconducting graphene nanoribbons: Phonon, impurity, and edge roughness scattering. *Phys Rev B* **78**, (2008).
23. Madsen, G. K. H., Singh, D. J. BoltzTraP. A code for calculating band-structure dependent quantities. *Comput Phys Commun* **175**, 67-71 (2006).
24. Bardeen, J., Shockley, W. Deformation Potentials and Mobilities in Non-Polar Crystals. *Physical Review* **80**, 72-80 (1950).
25. Kim, J. Y., Lee, J. H., Grossman, J. C. Thermal transport in functionalized graphene. *ACS Nano* **6**, 9050-9057 (2012).
26. Klemens, P. G. Theory of the A-Plane thermal conductivity of graphite. *J Wide Bandgap Mater* **7**, 332-339 (2000).
27. Chen, S. S., Wu, Q. Z., Mishra, C., Kang, J. Y., Zhang, H. J., Cho, K. J., *et al.* Thermal conductivity of isotopically modified graphene. *Nat Mater* **11**, 203-207 (2012).
28. Ziman, J. M. *Electrons and phonons: the theory of transport phenomena in solids*. Clarendon Press: Oxford,, 1960.
29. Hyldgaard, P., Mahan, G. D. Phonon superlattice transport. *Phys Rev B* **56**, 10754-10757 (1997).

Chapter 5

Optimization of the Thermoelectric Figure of Merit in Crystalline C₆₀ with Intercalation Chemistry

5.1. Introduction to Crystalline C₆₀

The C₆₀ fullerene has attracted great interest since its discovery by Kroto and co-workers in 1985,¹ due to its symmetric shape and unique properties. This interest dramatically increased after the synthesis of C₆₀ solid by Krätschmer *et al.* (1990).² In crystalline C₆₀, the molecules stick together through van der Waals forces in the fcc crystal structure. The discrete levels of a free C₆₀ molecule are broadened in the solid, inducing energy dispersion as shown in Figure 5.1. Crystalline C₆₀ is a semiconductor with direct gap around 1.5 eV. In 1991, Haddon *et al.*³ found that the intercalation of alkali metals in crystalline C₆₀ induces metallic behavior, and doped C₆₀ shows superconductivity with a large value of T_C (*e.g.*, T_C = 40K for Cs₃C₆₀).⁴

In this chapter, we explore the C₆₀ fulleride, a fullerene doped with a metal atom, as a candidate material for thermoelectric applications due to its low thermal conductivity ($\kappa \sim 0.4$ W/mK at room temperature),⁵ exhibiting the lowest thermal conductivity among carbon materials. This is mostly due to the phonon scattering, arising from randomly rotating C₆₀ molecules between various orientations at room temperature. Furthermore, the electronic transport of crystalline C₆₀ can be widely modified by doping. Even in the close-packed structure, solid C₆₀ contains large voids due to its large linear size (~ 7 Å) as a building block, and they can accommodate small atoms, ions, or even molecules. Such dopants can play an

important role in electronic properties of solid C_{60} by donating electrons to C_{60} due to the unsaturated character of the C-C bonds on the C_{60} . The variation of dopant atoms provides a wide range of accessible electronic states in solid C_{60} .

In contrast to the case of graphene, crystalline C_{60} exhibits inferior thermal and charge transport compared with other carbon materials. In this chapter, we demonstrate how these transport properties in solid C_{60} can be improved for thermoelectric applications through intercalation chemistry using both classical and quantum mechanical calculations.

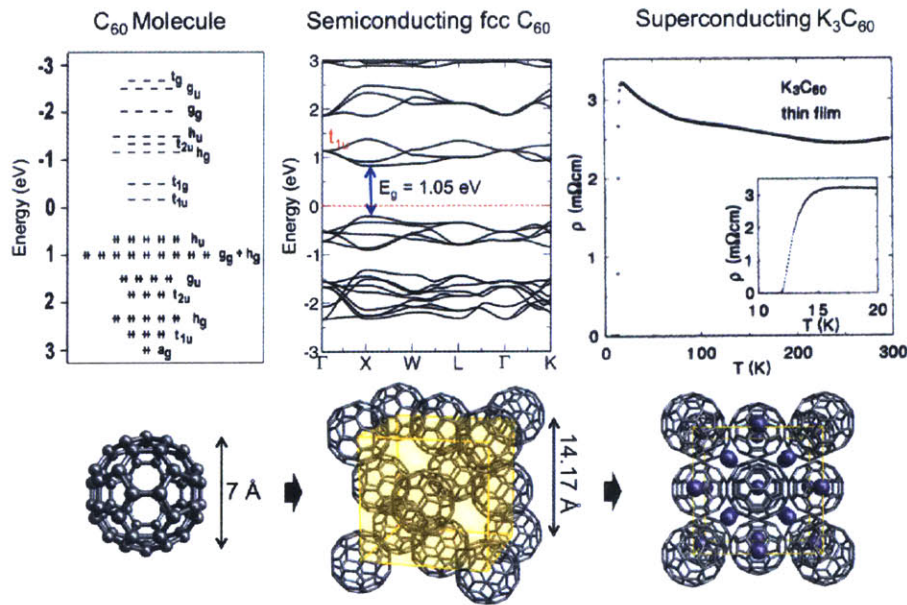


Figure 5.1 | Hückel energy levels of C_{60} molecule, band structure of crystalline fcc- C_{60} , and resistivity of K_3C_{60} thin film as a function of temperature, exhibiting superconducting behavior upon the introduction of K atoms.⁶

5.2. Effect of Doping Composition on Thermoelectric Properties in A_xC_{60}

5.2.1. Crystal Structure and Electronic Structure in A_xC_{60}

Fcc C_{60} contains voids at its octahedral and tetrahedral sites, and these voids are sufficiently large to intercalate impurity atoms, such as alkali metals, due to the large size of

the C_{60} molecule. When alkali metals are doped into these voids, crystalline C_{60} converts from a semiconductor into a metal. The combination of alkali metals and alkaline earth elements in C_{60} leads to a variety of A_xC_{60} ($A = Na, K, Rb, Cs, Ca, Sr, Ba$ and their combinations) materials. FCC C_{60} can only account for compositions of A_xC_{60} ($x = 1 - 3$), since this structure contains one octahedral and two tetrahedral interstitial sites per C_{60} . Further doping of metal atoms gives rise to a change of the C_{60} lattice structure from closed-packed fcc to a more open, body-centered lattice. Accordingly, there are three distinct bulk phases upon metal doping: 1) the superconducting phase A_3C_{60} in the fcc structure, 2) the insulating A_4C_{60} in the bcc structure, and 3) the insulating A_6C_{60} in the bcc structure, in which there are six tetrahedral sites per C_{60} . In this work, we examine two different compositions: fcc- A_3C_{60} and bcc- A_6C_{60} .

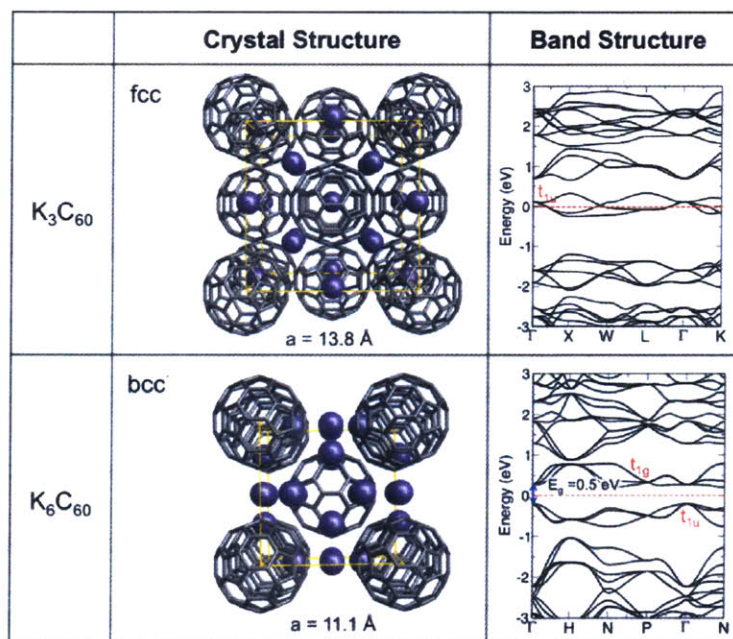


Figure 5.2 | Unit cells and corresponding band structures of K_3C_{60} in the fcc lattice and K_6C_{60} in the bcc lattice. Intercalated potassium atoms are represented by purple spheres. Energy bands derived from t_{1u} and t_{1g} energy levels of C_{60} molecules are shown.

Figure 5.2 shows the crystal structures and electronic band structures of both K_3C_{60} and

K_6C_{60} . For an un-doped solid C_{60} , the π -orbitals, originated from the molecular h_u levels of isolated C_{60} , make up the valence band, and the conduction band originates from the 3-fold t_{1u} molecular levels. When solid C_{60} is doped with metal atoms, the metal atoms give electrons to the t_{1u} -derived conduction band (or upper 3-fold t_{1g} -band), converting the behavior from insulating to metallic. In K_3C_{60} , three K atoms give three electrons to each C_{60} , leading to a half-filled t_{1u} -band since it can accommodate up to six electrons, in turn leading to metallic behavior. In contrast, the K_6C_{60} compounds will be insulators as the 3-fold degenerate t_{1u} -band is filled with six electrons at this doping composition. Our calculation predicts K_6C_{60} to be insulating, with an indirect gap of 0.5 eV (a valence band maximum at Γ , and a conduction band minimum at N). This is in quite good agreement with other previous work on electronic structure study on K_6C_{60} .⁷

5.2.2. Thermal Transport in A_xC_{60}

We carried out calculations of the thermal conductivity (κ) of alkali-metal doped C_{60} using the same formalism as described in the previous sections, namely equilibrium molecular dynamics (MD) simulations employed within the LAMMPS package,⁸ and κ is computed from the fluctuations of the heat current using the Einstein relation. To describe the covalent bonding interactions between C atoms and the long-range van der Waals interactions for C, K, and C – K, we used the Goddard Force Field (GFF),^{9,10} which has been successfully applied to the study of K-intercalated fullerenes.¹¹ Within this force field, the K atoms are assumed to be fully ionized to K^+ , and the charges on the C_{60} are distributed uniformly. The interactions are described by bond stretches (Morse), cosine angle bends, a two-fold torsion and long-range van der Waals interactions. These potentials are based on empirical fits to experimental data such as

lattice parameters, elastic modulus, and phonon frequencies for K intercalated graphite, and they predict vibrational frequencies in K_3C_{60} quite well.⁹ All simulations are carried out at 300 K with a time step of 0.2 fs. To obtain converged results, 15 separate simulations are averaged for each system, each with different initial conditions. In each run, after a 200 ps equilibration period, the microscopic heat flux is recorded for 2×10^7 MD steps (4ns) in order to obtain a converged thermal conductivity value. On the basis of convergence tests, we choose the size of the C_{60} lattice to be 40 Å (corresponding to 4000 atoms in the simulation cell) for all subsequent simulations. The lattice constant optimized with this force field is $a = 14.18$ Å in K_3C_{60} , and we used this value as a fixed lattice parameter during the MD simulations.

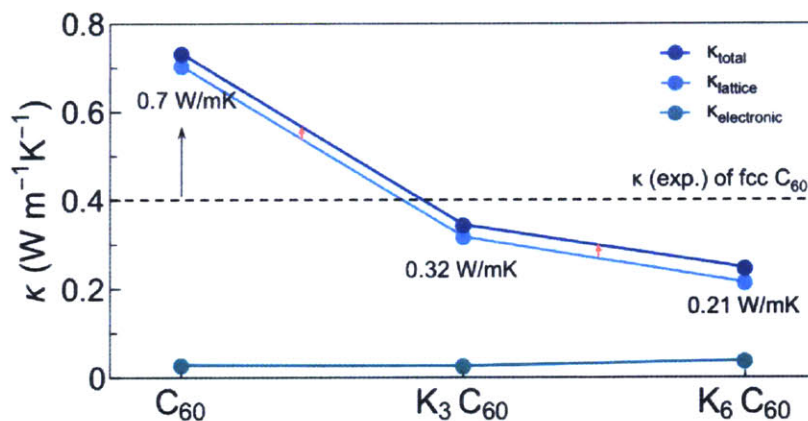


Figure 5.3 | Calculated electronic (green), lattice (sky-blue) and total (dark-blue) thermal conductivities of $K_x C_{60}$ samples as a function of doping composition. Pristine C_{60} and $K_3 C_{60}$ are in fcc lattice, and $K_6 C_{60}$ is in bcc lattice. Labels indicate computed lattice thermal conductivity values in each doping composition. Horizontal dashed line indicates the measured thermal conductivity of fcc- C_{60} ($\kappa \sim 0.4$ W/mK).⁵

Figure 5.3 shows the calculated lattice thermal conductivity (κ_l) of pristine fcc- C_{60} , $K_3 C_{60}$ and $K_6 C_{60}$. We note that the use of the GFF potential tends to overestimate κ_l (~ 0.7 W/mK) with respect to the measured value for single crystal C_{60} (0.4 W/mK at 300 K).⁵ This low κ_l

value is mainly due to the orientational disorder, which causes strong phonon scattering. The intercalation of K atoms suppresses κ_l , showing more than a 2-fold reduction from that of undoped C_{60} . This reduction is due to the disorder within the unit cell, achieved through rattling K atoms, enabling effective point-defect phonon scattering. It is interesting to note that further doping of K atom gives rise to further suppressed thermal transport, showing $\kappa_l = 0.21$ W/mK with K_6C_{60} , due to the higher density of rattling atoms in the unit cell.

The electronic thermal conductivity (κ_e) is computed through semi-classical Boltzmann theory within the constant relaxation time approximation, as implemented in the BOLTZTRAP code,¹² which is explained in Chapter 2. The κ_e values within the range we are interested are smaller than κ_l by an order of magnitude, as can be seen in Figure 5.5. The total thermal conductivity (κ) is given as the sum of the electronic (κ_e) and lattice (κ_l) contributions, and it also decreases with K atom concentration in the unit cell, demonstrating the lowest κ value for K_6C_{60} in the bcc lattice.

5.2.3. Charge Transport in A_xC_{60}

Room-temperature transport calculations of alkali-metal doped C_{60} are carried out using electronic structure calculations and the Boltzmann transport approach, as explained in Chapter 2. We performed first-principles electronic structure calculations for doped C_{60} , using the local-density approximation (LDA) within the framework of density functional theory and the Ceperly-Alder exchange-correlation functional. Geometry optimizations are performed using the conjugate gradient scheme until force components on every atom are less than 0.01 eV/Å. The fully relaxed structures are used to compute the electronic band structure.

In order to predict accurate transport coefficients, similar to our work on graphene

described in Section 4, we need to once again compute the energy-dependent relaxation time (τ), generally depending on the density of states ($N(\epsilon)$). The charge transport in alkali-metal doped C_{60} can be caused by various scattering mechanisms. A dominant scattering mechanism near room temperature is electron-phonon scattering, resulting in a linear temperature dependence of the resistivity. The contribution to the normal state resistivity due to electron-phonon scattering is calculated using Ziman's resistivity formula,¹³

$$\rho_{e-phonon}(T) = \frac{8\pi^2}{\omega_p^2 k_B T} \int_0^{\omega_{max}} \frac{\hbar \omega \alpha_r^2 F(\omega)}{\cosh(\hbar \omega / k_B T) - 1} d\omega \quad (5.1)$$

where ω_p is the plasma frequency, and the transport coupling function $\alpha_r^2 F(\omega)$ can be replaced by the electron-phonon coupling constant (λ) as $\alpha_r^2 F(\omega) = \frac{1}{2} \sum_v \omega_v \lambda_v \delta(\omega - \omega_v)$.

Here, the λ value is proportional to the density of states ($N(\epsilon_F)$) as $\lambda = N(\epsilon_F) \nu$, where ν is the corresponding electron-phonon coupling strength. Two other scattering mechanisms are the electron-electron scattering, leading to the presence of T^2 -like dependence, and the scattering originated from orientational disorder, resulting in a large residual resistivity. Accordingly, the overall relaxation time can be determined through

$$\frac{1}{\tau_{total}} = \frac{1}{\tau_0} + \frac{1}{\tau_{e-e}} + \frac{1}{\tau_{e-phonon}} \quad (5.2)$$

where $1/\tau_0$ ($1/\tau_{e-e}$ and $1/\tau_{e-phonon}$) is the scattering rate arising from orientational disorder (electron-electron and electron-phonon scattering, respectively).

For metals, the resistivity is given by $\rho = 4\pi/\omega_p^2 \tau$, and thus, at high temperature the total relaxation time can be expressed as

$$\frac{1}{\tau_{total}} = \frac{\rho_0}{4\pi} \omega_p^2 + \frac{\rho_{e-e}}{4\pi} \omega_p^2 + \frac{2\pi k_B T}{\hbar} \nu N(\epsilon_F) \quad (5.3)$$

Here, the plasma frequency is determined by $\omega_p^2 = \frac{4\pi}{3} e^2 v_F^2 N(\epsilon)$, where v_F ($=1.8 \times 10^7$ cm/s) is the Fermi-surface averaged electron velocity, and $N(\epsilon_F) \sim 14$ states/eV for K_3C_{60} , resulting in $\omega_p = 1.2$ eV. The resistivity values are obtained from previous experimental work that reports the electrical conductivity of K_3C_{60} thin films, which exhibit the normal-state $\rho \sim 2$ m Ω cm at room temperature.¹⁴ In the K_3C_{60} case, the residual resistivity value is $\rho_0 = 1.2$ m Ω cm, and the value of ρ_{e-e} (at 300 K) = 0.9 m Ω cm is obtained from the relation $\rho_{e-e} = AT^2$, where $A = 0.01$ $\mu\Omega$ cm/K². To compute $\tau_{e-phonon}$, the ν value of K_3C_{60} (0.05 eV, corresponding to $\lambda \sim 0.7$ with $N(\epsilon_F) = 14$ states/eV) is used for all fullerides, where this value contains the electron-phonon coupling information of both intermolecular (low frequency) and intramolecular (high frequency) phonon contributions.¹⁵ To this end, all three terms in the scattering rate equation are proportional to the density of states, and accordingly the total scattering rate can be expressed as $\frac{1}{\tau_{total}(\epsilon)} = 0.568 \times 10^{14} N(\epsilon)$ with the above parameters. Using this relaxation time relation, we obtained the resistivity value of K_3C_{60} at $n_i = 4.21 \times 10^{21}$ /cm³ (three electrons per C_{60}) ~ 2.2 m Ω cm, which is in quite good agreement with the measured normal state resistivity value.⁶

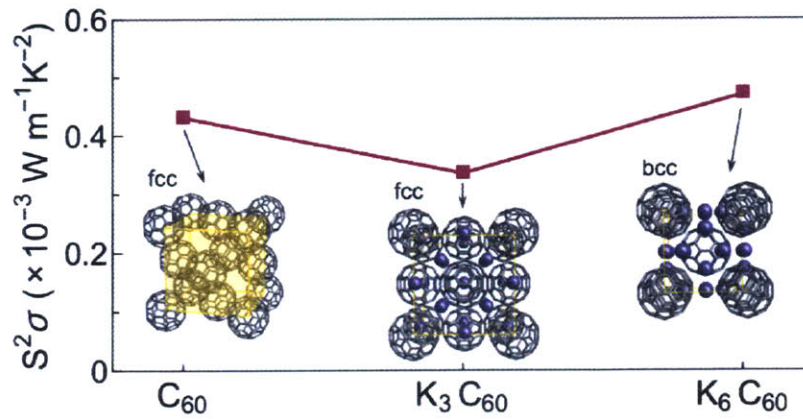


Figure 5.4 | Calculated power factors of pristine fcc C_{60} , K_3C_{60} in fcc lattice and K_6C_{60} in bcc lattice. Intercalated potassium atoms are represented by purple spheres, and yellow cubic represents the unit cell of fcc lattice in pristine C_{60} .

The electrical conductivity (σ) and Seebeck coefficient (S) are calculated as a function of carrier concentration (n_i), resulting in a maximum power factor at the edge of the t_{1u} -band for un-doped C_{60} and K_3C_{60} , and the edge of the t_{1g} -band for K_6C_{60} . The calculated $S^2\sigma$ of A_xC_{60} with different doping compositions ($x = 0, 3$ and 6) are shown in Figure 5.4, and the K_6C_{60} sample in the bcc lattice exhibits the highest $S^2\sigma$ value. It is interesting to note that the more open bcc lattice exhibits a higher power factor than the close-packed fcc lattice. This can be explained by the broadened t_{1u} (t_{1g}) valence (conduction) band, caused by the introduction of K atoms in the bcc lattice. Such band widening is considered to be due to the presence of hybridization between C_{60} and K electronic states.¹⁶ This is contrary to the case of the fcc lattice, where dispersion of the t_{1u} band is not affected by K intercalation. The hybridization between C_{60} and metal states in the bcc lattice is explained in detail in section 5.3.2.

5.2.4. Prediction of Figure of Merit ZT in A_xC_{60}

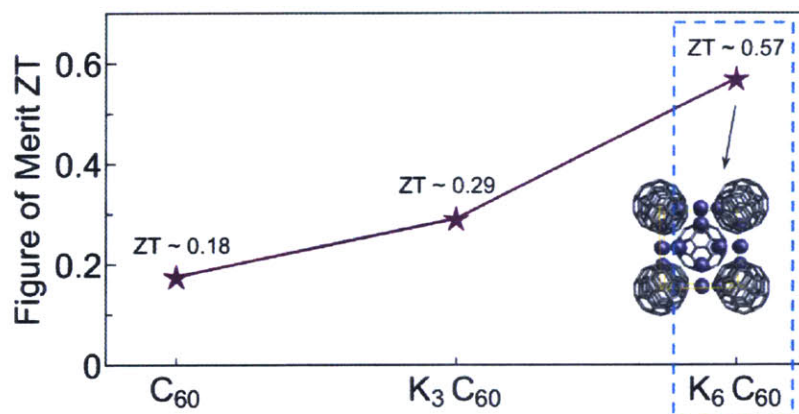


Figure 5.5 | Calculated figure of merit ZT values of pristine fcc C_{60} , K_3C_{60} in the fcc lattice and K_6C_{60} in the bcc lattice.

Combining both the thermal and charge transport studies described above, we are able to predict the full ZT in A_xC_{60} samples. Among the three fulleride samples, K_6C_{60} yields the highest ZT ~ 0.6 at room temperature, owing to both the lowest κ and highest $S^2\sigma$. This high ZT value, compared with other organic TE materials, suggests the potential of alkali-metal doped C_{60} in the bcc lattice as a candidate material for thermoelectric applications. Here, it should be noted that our predicted value of ZT for A_xC_{60} samples are underestimated possibly by a factor of 2, arising from the overestimated κ_l values from MD simulations.

5.3. Effects of Dopants on Thermoelectric Properties in A_xC_{60}

5.3.1. Face-centered Cubic (fcc) A_3C_{60}

We first investigate the effect of lattice parameter variation on thermoelectric properties of alkali-metal doped C_{60} with stoichiometry A_3C_{60} in fcc lattice. Many previous theoretical and experimental studies demonstrate that A_3C_{60} exhibits superconductivity, and its transition temperature (T_C) increases monotonically with unit cell size.^{17,18} As the lattice increases, the

overlap between C_{60} ions decreases, resulting in a reduced bandwidth and an increased electronic density of states ($N(\epsilon_F)$), which enhances the T_C of A_3C_{60} . The lattice parameter variation of A_3C_{60} results from the insertion of A ions of various size by chemical doping. In this work, we consider four different alkali metals (A= Na, K, Rb, and Cs).

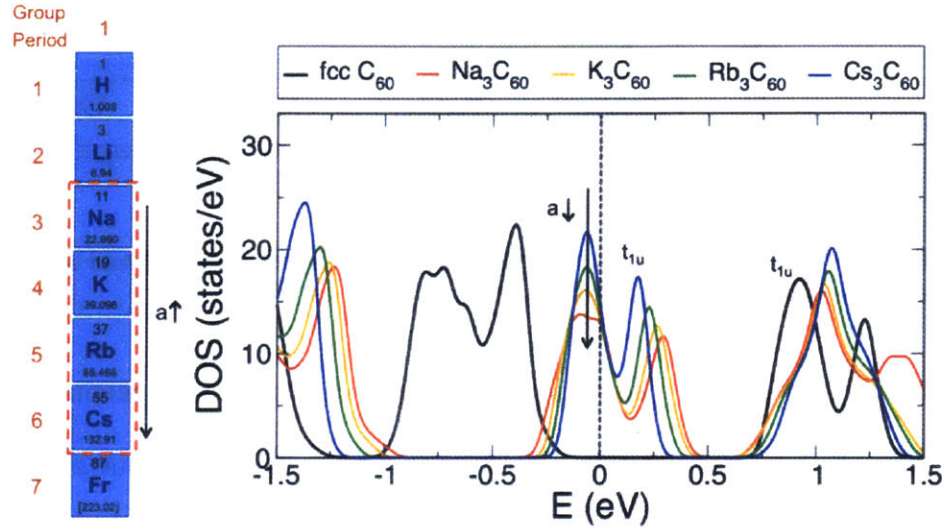


Figure 5.6 | Computed density of states of A_3C_{60} (A = Na, K, Rb and Cs) fullerides. The lattice parameter (a) of A_3C_{60} increases with the ionic radius of intercalated alkali metals. As lattice parameter decreases, density of states of t_{1u} band in A_3C_{60} samples decreases.

We first compute the electronic structure of A_3C_{60} , and the calculated density of states are shown in Figure 5.6. In A_3C_{60} , the lattice parameter increases with the size of the inserted A ion, where the lattice parameter ranges from 13.7 (Na_3C_{60}) to 14.4 Å (Cs_3C_{60}). As we expected, A_3C_{60} samples with smaller lattice parameters shows lower $N(\epsilon_F)$ of the t_{1u} -band due to the increased overlap between C_{60} ions, which would be expected to suppress S according to Mahan-Sofa theory.¹⁹ In contrast to the suppressed S, as the lattice parameter decreases, σ is expected to increase owing to the more dispersive electronic band.

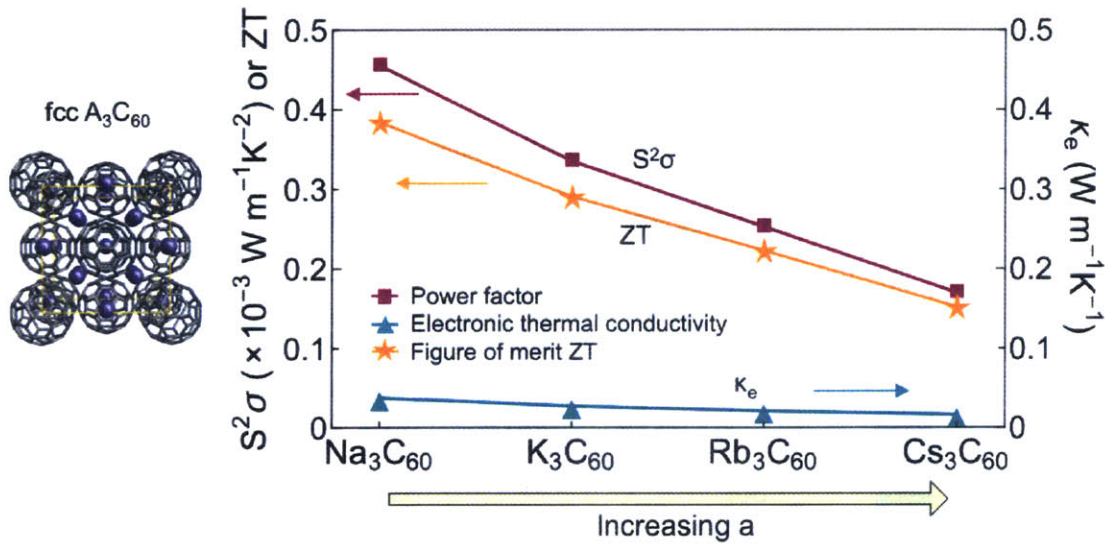


Figure 5.7 | Electronic thermal conductivity (green), power factor (purple) and ZT (orange) values of A_3C_{60} (A = Na, K, Rb and Cs) fullerides in fcc lattice.

Our transport coefficient calculations show that as the lattice parameter decreases, σ increases while S decreases. This is indeed what we expected from our electronic structure calculations. Interestingly, between these two conflicting thermoelectric properties, σ is more influenced by the lattice variation than S , resulting in a maximum value of $S^2\sigma$ with Na_3C_{60} sample (Figure 5.7). Although κ_e decreases with lattice parameter as well, our calculated ZT values exhibit the same lattice parameter dependence with $S^2\sigma$, due to the lower κ_e values by an order of magnitude compared to $S^2\sigma$ values (Figure 5.7). Here, the κ_1 value of K_3C_{60} (0.32 W/mK) is used for all A_3C_{60} samples since the mass differences of the inserted ions has a negligible effect on thermal transport in A_3C_{60} samples. Among these samples, the Na_3C_{60} case exhibits the highest ZT ~ 0.4 at room temperature. This result implies that a smaller lattice parameter is more favorable for thermoelectric applications, which is opposite to the case of C_{60} -based superconductivity. The role of the dopant in A_3C_{60} samples is to modulate the volume of the unit cell, and accordingly the bandwidth as well, which is an important

optimization factor in controlling charge transport in fullerenes.

5.3.2. Base-centered Cubic (bcc) A_6C_{60}

We investigate the effect of dopants on transport coefficients in bcc A_6C_{60} samples as well. As mentioned in section 5.2.3, the charge transfer from an A ion to C_{60} is not complete at this composition, resulting in a hybridization between the C_{60} and A electronic states. Comparison between actual K_6C_{60} and hypothetical pristine bcc- C_{60} with the same lattice parameter demonstrates that the fully occupied t_{1u} -band of K_6C_{60} is considerably wider than that of the empty t_{1u} -band of pristine bcc- C_{60} . This band widening is mainly due to the presence of hybridization between the C_{60} and K states. In bcc A_6C_{60} , the electronic band becomes more dispersive with alkali metal doping. Accordingly, in addition to the lattice parameter, dopant variation could provide another strong controlling factor, namely hybridization variation, on charge transport in bcc A_6C_{60} samples, in contrast to the case of fcc A_3C_{60} samples, where only the lattice parameter can be modulated by the dopants. Here, we consider two different kinds of dopants, alkali metals (A_6C_{60} , A = Na, K and Rb), alkaline earth metals (AE_6C_{60} , AE = Ca, Sr and Ba) and their combinations ($K_3AE_3C_{60}$ and $A_3Ba_3C_{60}$), to investigate how doping influences the thermoelectric properties of fullerenes in the bcc lattice. We note that AE ions are expected to provide stronger hybridization between C_{60} and ion states than A intercalation, leading to a wider bandwidth.¹⁶

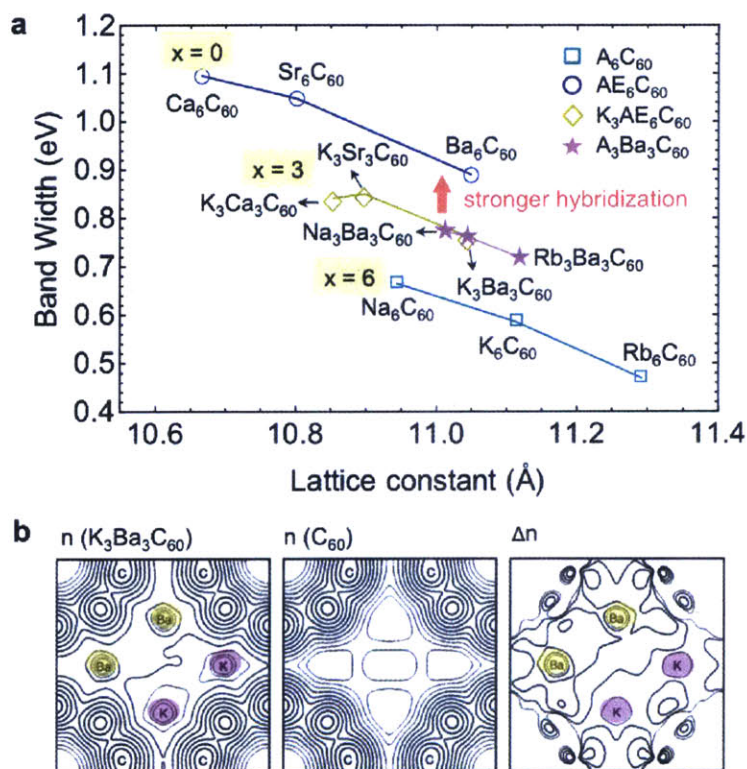


Figure 5.8 | The effect of the metal atom intercalation on bandwidth. (a) Calculated bandwidth (W) with corresponding lattice constant of $A_xAE_{6-x}C_{60}$ samples. (b) Valence-electron density of $K_3Ba_3C_{60}$, pristine bcc C_{60} , and the difference between them. The center of C_{60} is located at each corner.¹⁶ A sizable electron density is found around K sites (Pink), and a larger density remains around Ba sites (Yellow).

As can be seen in Figure 5.8, the lattice parameters of bcc $A_xAE_{6-x}C_{60}$ ($x = 0, 3$ and 6) fullerenes are significantly influenced by the dopants. We found that the lattice constant decreases with the size of dopant ions within the samples with the same composition, similar to the fcc A_3C_{60} fullerene cases. Interestingly, fullerene samples with larger AE ion composition exhibit smaller lattice constant. For example, the lattice constants of Ba_6C_{60} and Sr_6C_{60} are smaller than K_6C_{60} , despite the larger ionic radii of these dopants, in agreement with previous studies.^{16,20} This result implies that AE ion doping induces stronger hybridization between C_{60} and metal ions than the A ion case, resulting in stronger C_{60} and ion interaction, which could decrease the fullerene interspacing.

When hybridization exists, the lattice constant reduction does not always result in a simple broadening of the band structure. We compute the t_{1g} -band widths (W), which are the difference between maximum and minimum energy levels in the band, of fullerides in the bcc lattice. As can be seen in Figure 5.8, the t_{1g} -band width decreases with lattice parameter within the samples with the same composition, as in the case of fullerides in the fcc lattice. However, samples with the same lattice parameter do not always result in the same bandwidth. Fulleride samples ($A_xAE_{6-x}C_{60}$) with higher AE ion composition exhibit larger bandwidths than the samples with lower AE ion composition even with the same lattice parameter: $W(x = 0) > W(x = 3) > W(x = 6)$. We note that this bandwidth gap arises from the different hybridization of each dopant, and stronger hybridization is generated with AE ions as we expected from our lattice parameter study. This can be explained by the previous valence-electron density study of the $K_3Ba_3C_{60}$ fulleride,¹⁶ demonstrating that considerable electron densities remain around both the Ba and K sites, and densities around the Ba are larger than the K site, implying stronger hybridization with Ba ions (Figure 5.8b). Thus, the intercalation of metal atoms in crystalline bcc C_{60} has an impact not only on the lattice constant, but also on the hybridization with C_{60} , where both variations determine the bandwidth of bcc fullerides together.

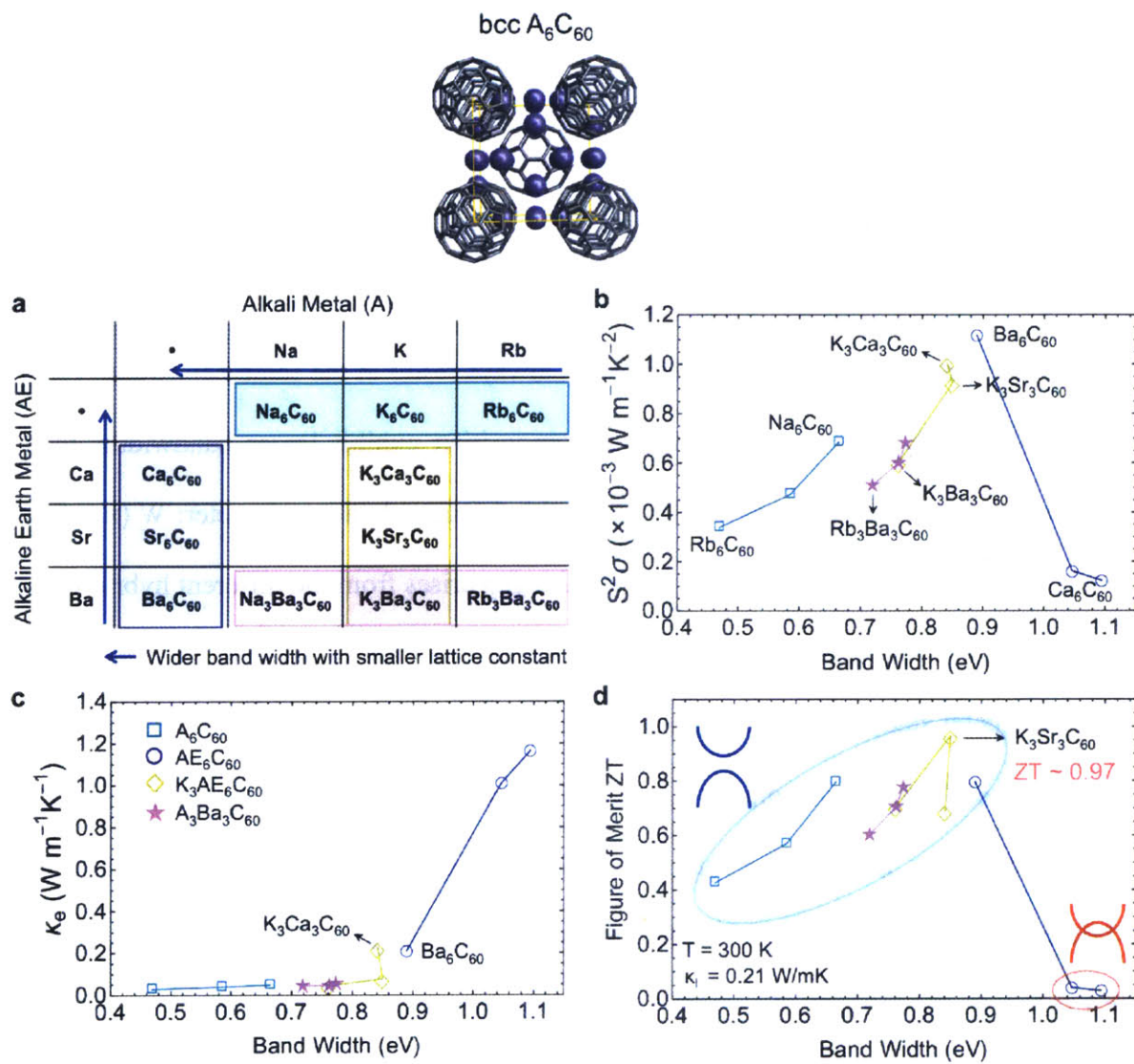


Figure 5.9 | Thermoelectric properties of $A_xAE_{6-x}C_{60}$ ($x=0, 3$ and 6) fullerides. (a) All considered $A_xAE_{6-x}C_{60}$ samples are listed. We consider three different alkali metals (Na, K and Rb) and three different alkali earth metals (Ca, Sr and Ba). Here, blue arrow indicates the direction for bandwidth increase and lattice constant decrease. Power factors (b), electronic thermal conductivities (c) and ZT values (d) of $A_xAE_{6-x}C_{60}$ fullerides are computed as a function of bandwidth (W).

Next, we calculate the thermoelectric properties ($S^2\sigma$, κ_e and ZT) of $A_xAE_{6-x}C_{60}$ ($x=0, 3$ and 6) as shown in Figure 5.9. As we expected, σ increases with bandwidth, while S decreases. These two conflicting properties generate a dependence between the power factor and bandwidth with a maximum value of $S^2\sigma$ at $W \sim 0.9$ eV for Ba_6C_{60} . Below this bandwidth, $S^2\sigma$

roughly increases as the bandwidth increases, as in the case of the fcc lattice, mostly due to the increase in σ . Significant $S^2\sigma$ reduction beyond its maximum point arises from considerably reduced S values, by a factor of 7, compared with other $A_xAE_{6-x}C_{60}$ samples, despite the increased σ values. This behavior can be explained by the strong hybridization between C_{60} and AE states, inducing an overlap between valence and conduction bands, and making these fullerides semimetallic,²¹ resulting in the sharp reduction of S . κ_e increases with bandwidth, owing to more dispersive electronic bands with larger bandwidth, as in the case of σ . The results demonstrate that the hybridization between C_{60} and dopant metal states plays an important role in the charge transport of crystalline C_{60} in the bcc lattice, and optimization of dopants could lead to further improvement of the electronic properties in crystalline C_{60} .

We predict the full ZT in bcc fullerides, combining with our computed lattice thermal conductivity of K_6C_{60} ($\kappa_l = 0.21$ W/mK), as shown in Figure 5.9d. Among these samples, a ZT value as large as 1 can be achieved in the case of $K_3Sr_3C_{60}$ at room temperature. This significant enhancement in ZT, by a factor of ~ 5 with respect to pristine crystalline C_{60} , is due to a combination of a reduction in κ and enhancement in $S^2\sigma$. This ZT value is further above the highest ZT value yet reported among organic thermoelectric materials at room temperature ($ZT \sim 0.4$).²² Here, as we noted in the previous section, for pristine C_{60} our computed lattice thermal conductivity value is overestimated by a factor of 1.8 with respect to the measured value, resulting in underestimated ZT values in fullerides. This high ZT value indicates the importance of optimizing intercalating dopants in crystalline C_{60} , which could engineer the thermoelectric properties of fullerides, by simultaneously improving all of the properties constituting ZT.

5.4. Outlook and Future Work

In this work, we investigated the thermoelectric properties of crystalline C₆₀ intercalated with alkali and alkaline earth metals using both classical and quantum mechanical calculations. The intercalation of metal atoms could play an important role in controlling both thermal and charge transport. Introduction of dopants generates strong phonon scattering in crystalline C₆₀, and thermal transport in such materials can be tuned by dopant composition. These results also demonstrate that dopant variation could broadly tailor charge transport in fullerides, introducing different effects on the bandwidths, which mostly determine charge transport in crystalline C₆₀. Thus, the introduction of metal atoms in crystalline C₆₀ could be an important route to designing high-efficiency fullerene-based thermoelectric materials, by improving both charge and thermal transport.

References

1. H. W. Kroto, J. R. H., S. C. O'Brien, R. F. Curl, R. E. Smalley. C₆₀: Buckminsterfullerene. *Nature* **318**, 162-163 (1985).
2. Kratschmer, W., Lamb, L. D., Fostiropoulos, K., Huffman, D. R. Solid C-60 - a New Form of Carbon. *Nature* **347**, 354-358 (1990).
3. Haddon, R. C. Electronic-Structure, Conductivity, and Superconductivity of Alkali-Metal Doped C-60. *Acc Chem Res* **25**, 127-133 (1992).
4. Ganin, A. Y., Takabayashi, Y., Khimyak, Y. Z., Margadonna, S., Tamai, A., Rosseinsky, M. J., *et al.* Bulk superconductivity at 38 K in a molecular system. *Nat Mater* **7**, 367-371 (2008).
5. Yu, R. C., Tea, N., Salamon, M. B., Lorents, D., Malhotra, R. Thermal conductivity of single crystal C₆₀. *Phys Rev Lett* **68**, 2050-2053 (1992).
6. Palstra, T. T. M., Haddon, R. C., Hebard, A. F., Zaanen, J. Electronic Transport-Properties of K₃C₆₀ Films. *Phys Rev Lett* **68**, 1054-1057 (1992).
7. Erwin, S. C., Pederson, M. R. Electronic-Structure of Crystalline K₆C₆₀. *Phys Rev Lett* **67**, 1610-1613 (1991).
8. Plimpton, S. Fast Parallel Algorithms for Short-Range Molecular-Dynamics. *J Comput Phys* **117**, 1-19 (1995).
9. Chen, G. H., Guo, Y. J., Karasawa, N., Goddard, W. A. Electron-Phonon Interactions and Superconductivity in K₃C₆₀. *Phys Rev B* **48**, 13959-13970 (1993).
10. Guo, Y. J., Karasawa, N., Goddard, W. A. Prediction of Fullerene Packing in C₆₀ and C₇₀ Crystals. *Nature* **351**, 464-467 (1991).
11. Gao, G. H., Cagin, T., Goddard, W. A. Position of K atoms in doped single-walled carbon nanotube crystals. *Phys Rev Lett* **80**, 5556-5559 (1998).
12. Madsen, G. K. H., Singh, D. J. BoltzTraP. A code for calculating band-structure dependent quantities. *Comput Phys Commun* **175**, 67-71 (2006).
13. Grimvall, G. *The electron-phonon interaction in metals*. North-Holland Pub. Co. : sole distributors for the

- U.S.A. and Canada, Elsevier North-Holland: Amsterdam ; New York, 1981.
14. Erwin, S. C., Pickett, W. E. Theoretical Normal-State Transport-Properties of K₃C₆₀. *Phys Rev B* **46**, 14257-14260 (1992).
 15. Tanaka, K., Huang, Y. H., Yamabe, T. Semiempirical Estimation of the Intermolecular Electron-Phonon Coupling in K₃C₆₀ and Rb₃C₆₀. *Phys Rev B* **51**, 12715-12720 (1995).
 16. Umemoto, K., Saito, S., Oshiyama, A. Electronic structure of K₃Ba₃C₆₀ and Rb₃Ba₃C₆₀ superconductors. *Phys Rev B* **60**, 16186-16191 (1999).
 17. Gunnarsson, O. Superconductivity in fullerenes. *Reviews of Modern Physics* **69**, 575-606 (1997).
 18. Fleming, R. M., Ramirez, A. P., Rosseinsky, M. J., Murphy, D. W., Haddon, R. C., Zahurak, S. M., *et al.* Relation of Structure and Superconducting Transition-Temperatures in A₃C₆₀. *Nature* **352**, 787-788 (1991).
 19. Mahan, G. D., Sofo, J. O. The best thermoelectric. *Proc Natl Acad Sci USA* **93**, 7436-7439 (1996).
 20. Erwin, S. C. Electronic-Structure of Superconducting Ba₆C₆₀. *Phys Rev B* **47**, 14657-14660 (1993).
 21. Kortan, A. R., Kopylov, N., Glarum, S., Gyorgy, E. M., Ramirez, A. P., Fleming, R. M., *et al.* Superconductivity in Barium Fullerene. *Nature* **360**, 566-568 (1992).
 22. Kim, G. H., Shao, L., Zhang, K., Pipe, K. P. Engineered doping of organic semiconductors for enhanced thermoelectric efficiency. *Nat Mater* **12**, 719-723 (2013).

Chapter 6

Conclusion

In this dissertation we have presented a detailed atomistic study of both thermal and charge transport in carbon-based nano-materials. We have focused on graphene and crystalline C_{60} , and have carried out a series of calculations using equilibrium molecular dynamics, lattice dynamics, density functional theory, and semi-classical Boltzmann transport theory. Using these simulation methods, we studied the effects of chemical modifications (*i.e.*, chemical functionalization on graphene, and metal atom intercalation in crystalline C_{60}) on thermal and charge transport in these carbon-based materials. The understanding gained of the key thermoelectric properties enabled us to provide new design strategies for high-efficiency thermoelectric materials.

We first studied the influence of 2D periodic patterns on the thermal transport of partially functionalized graphene with different functional groups, employing a combination of classical molecular dynamics and lattice dynamics simulations. Our calculations showed that the use of patterned 2D shapes on graphene reduces the room-temperature thermal conductivity by as much as 40 times compared to that of the pristine monolayer, due to a combination of boundary and clamping effects. Lattice dynamics calculations elucidated the correlation between this large reduction in thermal conductivity and two dynamical properties of the main heat carrying phonon modes: 1) decreased phonon lifetimes by an order of magnitude due to scattering, and 2) direction-dependent group velocities arising from phonon confinement. Taken together, these

results suggested that patterned graphene nano-roads provide a method for tuning the thermal conductivity of graphene without the introduction of defects in the lattice, opening an important possibility for thermoelectric applications.

Next, *ab initio* electronic structure calculations and the Boltzmann transport approach were used to determine the role of chemical functionalization on the electrical transport properties, including the electrical conductivity (σ) and Seebeck coefficient (S), which combined with our computed thermal conductivities enables us to predict the full ZT in these materials. We predicted that suitable chemical functionalization of graphene can introduce peaks in the density of states at the band edge that result in a large enhancement in the Seebeck coefficient, leading to an increase in the room-temperature power factor of a factor of two compared to pristine graphene, despite the degraded electrical conductivity. Furthermore, the presence of patterns on graphene reduces the thermal conductivity, which when taken together, leads to an increase in the figure of merit for functionalized graphene by up to 2 orders of magnitude over that of pristine graphene, reaching a maximum ZT ~ 3 at room temperature according to our calculations. These results suggest that appropriate chemical functionalization could lead to efficient graphene-based thermoelectric materials.

Finally, we investigated the thermoelectric properties of crystalline C₆₀ intercalated with alkali and alkaline earth metals using both classical and quantum mechanical calculations. Through these calculations, we have understood the influence of doping concentration and dopants on the thermoelectric properties of crystalline C₆₀. Intercalating metal atoms in solid C₆₀ gives rise to strong phonon scattering, and thermal transport in solid C₆₀ can be tuned depending on dopant composition. In addition, a variation of dopants could broadly tailor charge transport in fullerides, introducing different effects on bandwidths, which mostly determine the charge

transport in crystalline C_{60} . Based on this understanding, we optimized the thermoelectric figure of merit ZT in crystalline C_{60} , predicting $ZT \sim 1$ at room temperature with appropriate doping. Here, all of the properties constituting ZT can be improved simultaneously with metal atom intercalation. Thus, the introduction of metal atoms in crystalline C_{60} could be an important route to designing high-efficiency fullerene-based thermoelectric materials.

One of the most exciting ways in which computational materials design can be applied to the field of thermoelectrics is in the discovery of new classes of thermoelectric materials that have not been previously considered for thermoelectric applications. This is now possible because of the age of materials design we have entered, and it is happening in many fields across science and engineering for an ever-expanding range of materials. Rather than only examining the material that is already known as a “good” thermoelectric material and making it better, we can think much more broadly and creatively. The creation of new materials learning curves will play a crucial role in paving the way towards cost effective and efficient energy technologies. It is in this spirit that we have explored in this thesis an understanding of the impact of chemical modifications on the thermal and charge transport in carbon-based materials, which could provide new design strategies for high efficiency thermoelectric materials.